Dissertation

submitted to the

Combined Faculty of Natural Sciences and Mathematics of

the Ruperto Carola University Heidelberg, Germany for the

degree of

Doctor of Natural Sciences

Presented by

M.Sc. Olivia Krefft

born in: Berlin, Germany

oral examination: 30.09.2020

Unraveling the pathology of different disease severities

in human cerebral organoid models

of LIS1-lissencephaly

Referees: Professor Dr. Ana Martin-Villalba

Professor Dr. Philipp Koch

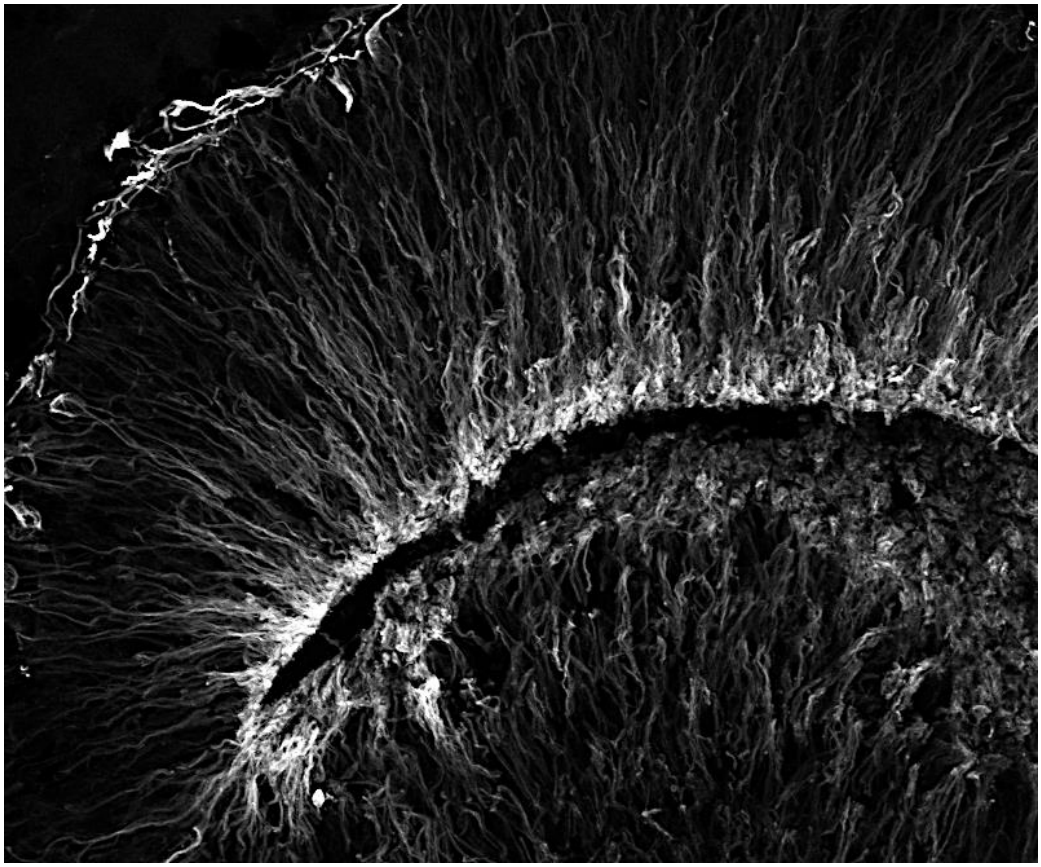

“Don't let anyone rob you of your imagination, your creativity, or your curiosity. It is your place in the world.
It is your life. Go on and do all you can with it,
and make it the life you want to live.”
-Mae Jemison

This master thesis was planned, executed and written by Olivia Krefft (D-68163 Mannheim, Rheinvillenstraße 4, E-Mail: olivia.krefft@web.de) over a period of time from April 2016 to Mai 2020 under the direct scientific supervision of Dr. Julia Ladewig and Professor Dr. Philipp Koch.

Thanks to both for their help and support in practical and theoretical questions. Furthermore, I want to thank patients, their families and clinicians for the access to the patient material used in this study. Thank you for supporting my study.

First referee: Professor Dr. Ana Martin-Villalba (Head of the Department Molecular Neurobiology at the German Cancer Research Center in Heidelberg, Germany).

Second referee: Professor Philipp Koch (Head of the Hector Institute of Translational Brain Research (HITBR) at the Central Institute for Mental Health in Mannheim, Germany).

Third referee: Professor Dr. Valery Grinevich (Head of the Department Neuropeptide Research in Psychiatry at the Central Institute for Mental Health in Mannheim, Germany).

Fourth referee: Professor Dr. Gudrun Rappold (Head of the Department Human Molecular Genetics at the Institute of Human Genetics at the University of Heidelberg, Germany).

Direct scientific supervisor: Dr. Julia Ladewig (Head of the Department Developmental Neuropathologies at the HITBR at the Central Institute for Mental Health in Mannheim, Germany).

Thanks to the reviewers for examining my work.

Declaration

Sworn Affidavit according to § 8 of the doctoral degree regulations of the Combined Faculty of Natural Sciences and Mathematics, Ruprecht-Karls-Universität Heidelberg

1. The thesis I have submitted entitled “Unraveling the pathology of different disease severities in human cerebral organoid models of LIS1-lissencephaly” is my own work.
2. I have only used the sources indicated and have not made unauthorized use of services of a third party. Where the work of others has been quoted or reproduced, the source is always given.
3. I have not yet presented this thesis or parts thereof to a university as part of an examination or degree.
4. I confirm that the declarations made above are correct.
5. I am aware of the importance of a sworn affidavit and the criminal prosecution in case of a false or incomplete affidavit.

Parts of my work have been published in Iefremova et al. (Iefremova et al. 2017) and Krefft et al. (Krefft et al. 2018). In addition, a review summarizing recent publications about unravelling the mechanisms underlying malformations of human cortical development using cerebral organoids is in press (Krefft, Ladewig, and Koch 2020). The main publication of my dissertation is in final preparation.

_____ _____

Place and date Signature

Zusammenfassung

Lissenzephaly ist eine kortikale Entwicklungsstörung, die durch ein glattes Gehirn und einen unstrukturierten Cortex charakterisiert ist. Mutationen im LIS1 Gen wurden als häufigste Ursache für diese Erkrankung identifiziert. LIS1-Lissenzephaly zeichnet sich dadurch aus, dass Betroffene unterschiedlich schwer erkrankt sind. Einige haben verbreitete kortikale Einfaltungen, sogenannte Gyri und zeigen milde Krankheitsverläufe, andere wiederum sind schwer betroffen und haben ein glattes Gehirn ohne Gyri. Analysen in murinen Systemen konnten bislang nicht die Gesamtheit der Erkrankung widerspiegeln, zeigten jedoch, dass die Dosierung von LIS1 für die Schwere der Erkrankung relevant ist. Dennoch konnte die Frage, warum eine spezifische Mutation im LIS1 Gen, wie sie bei den Erkrankten identifiziert wurden, zu unterschiedlichen Ausprägung der Erkrankungen führt, durch das Fehlen von adäquaten Modellsystem, bisher nicht beantwortet werden. Das gleiche gilt für die Frage, ob die unterschiedlichen Mutationen human-spezifische Entwicklungsprozesse differenziert beeinflussen. Aus diesem Grund habe ich zusammen mit meinen Kollegen ein Protokoll für die Generierung von zerebralen Organoiden entwickelt und dessen Fähigkeit untersucht, verschiedene Schweregrade von LIS1-Lisenzephaly widerzuspiegeln. Hierfür wurden 7 unterschiedlich schwer erkrankte (mild, moderate und schwer) Lissenzephaly Patienten aus einer 63 Patienten Kohorte ausgewählt, bei welchen die Erkrankung durch eine molekular charakterisierte heterozygote Mutation im LIS1 Gen hervorgerufen wird. Um die Konsequenzen der einzelnen Patienten-spezifischen Mutationen auf die humane Gehirnentwicklung zu untersuchen, wurden von jedem Patienten somatische Zellen zu Stammzellen zurückprogrammiert, um 3D zerebrale Organoide zu generieren. Diese *in vitro* Gewebe zeigten krankheits-assoziierte phänotypische Veränderungen, die in ihrer Ausprägungsstärke mit den Schweregrad der Patienten korrelierten. Entwickelte Quantifizierungsprotokolle zeigten mit zunehmenden Schweregrad eine progressive Veränderung der kortikalen Ventrikular-Struktur-Dimensionen sowie verfrühte Neurogenese. Um die direkte Konsequenz der Patienten-spezifischen Mutationen auf die LIS1 Mikrotubuli-stabilisierende Funktion zu untersuchen, wurde das astrale Zytoarchitekutur-stabilisierende Zytoskelett analysiert und ein progressiver Zusammenbruch mit zunehmender Schwere der Erkrankung festgestellt, was zu einer zellulären Unordnung innerhalb des *in vitro* Gewebes führte. Die Behandlung der zerebralen Organoide mit EpothiloneD, ein Mikrotubuli-stabilisierendes FDA-genehmigtes Medikament, konnte die Zytoarchitektur stabilisieren und somit partiell die zelluläre Ordnung wiederherstellen. Darüber hinaus zeigte die Untersuchung

der Teilungsorientierung von apikalen Radialgliazellen, dass es in Organoiden, die von Zellen von schwer (weniger von moderat und mild) Erkrankten generiert wurden, eine spezifische Umorientierung von proliferativer zu neurogener Zellteilung gibt, was zu verfrühter Neurogenese und kleineren Ventrikular-Strukturen führte. Bei mild und moderat Erkrankten zeigten die Zellen dagegen überwiegend eine unspezifische Fehlorientierung der Zellteilungsebene, die ebenfalls, jedoch weniger stark ausgeprägt, im Vergleich zu schweren Bedingungen, zu verfrühter Neurogenese führte. Als molekulare Ursache für die spezifische Umorientierung der Zellteilungsebene konnte eine Störung der WNT Signalübertragung ermittelt werden, so dass der Zellteilungsstörung mit GSK3ß Inhibierung (WNT Signalübermittlungsaktivierung) entgegengewirkt werden konnte.

Meine Forschung zeigt, dass zerebrale Organoide sensitiv genug sind, um unterschiedliche Schweregrade einer Erkrankung widerzuspiegeln, eine zuvor nicht bewiesene große Herausforderung des *in vitro* Systems. Die Daten zeigen, dass die verschiedenen Patienten-spezifischen Mutationen im LIS1 Gen die Mikrotubuli-stabilisierende Funktion von LIS1 direkt unterschiedlich beeinflussen, was direkt (zelluläre Unordnung) oder indirekt (WNT-Signalübermittlungsstörungen) zu einer gestörten Entwicklung des Gehirn führt. Damit konnte diese Arbeit den bisher fehlenden Zusammenhang zwischen Patienten-spezifischen Mutationen und klinischen Schweregrad aufklären. Des Weiteren konnten involvierte Pathomechanismen spezifisch für den Schweregrad aufgedeckt und therapeutische Substanzen identifiziert werden, die den Krankheitsverläufen *in vitro* entgegenwirkten. Der zukünftige Einsatz von Organoiden für die Untersuchung von individuellen Krankheitsverläufen könnte personalisierte Medizin verbessern und zu einem tieferen Verständnis von Patienten-spezifischen Pathologien für personalisierte Therapien führen.

Abbreviations

2D	two-dimensional
3D	three-dimensional
AC-TUB	acetylated alpha-tubulin
AFP	alpha-fetoprotein
APS	ammonium persulfate
aRG cell	apical radial glia cell
bRG cell	basal radial glia cell
BDNF	brain derived neurotrophic factor
bp	base pair
CAM	cell adhesion molecule
cDNA	complementary deoxyribonucleic acid
CHIR	CHIR99021
CP	cortical plate
C	control
DAPI	4′,6-diamidino-2-phenylindole
ddH2O	double-distilled water
DMEM	dulbecco's modified Eagle's medium
DMSO	dimethyl sulfoxide
DNA	deoxyribonucleic acid
DSH	disheveled
DTT	dithiothreitol
dNTP	desoxy-nucleotide triphosphate
E8 medium	essential 8 medium
ECM	extracellular matrix
EDTA	ethylenediaminetetraacetic acid
EGF	epidermal growth factor
ERK	extracellular signal-regulated kinase
FBS	fetal bovine serum
FGF	fibroblast growth factor
FZ	frizzled
G3BP1	Ras GTPase-activating protein-binding protein 1
GSK3β	glycogen synthase kinase 3ß
h	hour

HCl	hydrochloric acid
HEPES	4-(2-hydroxyethyl)-1-piperazineethanesulfonic acid
hiPS cell	human induced pluripotent stem cell
HOPX	hop homeobox
IP	intermediate progenitor
iPS cell	induced pluripotent stem cell
KO	knockout
LIS1-patient	LIS1-lissencephaly patient
mild LIS1-patient	LIS1-lissencephaly patient with a mild reduction of gyrification
moderate LIS1-patient	LIS1-lissencephaly patient with an anterior-posterior gradient of malformation
severe LIS1-patient	LIS1-lissencephaly patient with a smooth brain
LRP	LDL-receptor-related protein
M	molar
MCD	malformation of cortical development
Min	minutes
ml	milliliter
MOI	multiplicity of infection
MPTP	1-methyl-4-phenyl-1,2,3,6-tetrahydropyridine
MZ	marginal zone
n	nano
N-Cad	N-cadherin
NMD	non-sense mediated decay
NSC	neural stem cell
OCT 3/4	octamer-binding transcription factor 3/4
P	phosphorylation
PBMC	peripheral blood mononuclear cell
PP	Pluripro medium
PAFAH1B1	platelet-activating factor acetylhydrolase IB subunit alpha
PBS	phosphate-buffered saline
PCR	polymerase chain reaction
Pen/Strep	penicillin-streptomycin
PFA	paraformaldehyde
rcf	relative centrifugal force
RG cell	radial glia cell

RNA	ribonucleic acid
RNAi	RNA interference
Rock inhibitor	rho-associated coiled-coil containing protein kinase
rpm	revolutions per minute
RT	reverse transcriptase
RT-PCR	reverse transcriptase polymerase chain reaction
S.d.	standard deviation
Sec	seconds
SEM	standard error of the mean
SG	stress granular
SMA	smooth muscle actin
Snp	single nucleotide polymorphism
SOX 2	SRY (sex determining region Y)-box 2
SSEA 3	stage-specific embryonic antigen 3
SG	stress granules
TAE	tris base, acetic acid and EDTA.
TBS	tris buffered saline
TBST	tris buffered saline tween20
TGFβ	transforming growth factor ß
TUBB3	βIII-Tubulin
VZ	ventricular zone
WT	wildtype
xg	times gravity

Table Legends

Figure Legends

Figure 25: CHIR treatment-related rescue of aRG cell division orientation improves organoid ventricular zone structure dimensions. (**A, B**) Representative DAPI recordings of control C3.1, mild P1.1, moderate P4.2 and severe P6.1 LIS1-patient derived organoids treated with DMSO or 1 µM CHIR. (**C-H**) Loop parameter quantification of CHIR and DMSO control treated organoids (control C3.1 DMSO N=16, control C3.1 CHIR N=21, control C4.1 DMSO N=10,control C4.1 CHIR N=18, mild P1.1 DMSO N=16, mild P1.1 CHIR N=24, mild 2.2 DMSO N=12, mild P2.2 CHIR N=11, moderate P3.2 DMSO N=14, moderate P3.2 CHIR N=12, severe P5.1 DMSO N=14, severe P5.1 CHIR N=11, severe P5.2 DMSO N=16,severe P5.2 CHIR N=11, severe 2.1 DMSO N=10, severe P6.1 CHIR N=10, severe P7.1 DMSO N=11, severe P7.1 CHIR N=11. Scale bars 200 µm. Error bars, ±SD. *p < 0.05, **p < 0.01, ***p < 0.001.

Abstract

The human neocortex is greatly expanded and exhibits a highly organized and extensively folded (gyrencephalic) structure. Model systems gave a fundamental understanding about how the cortex is generated although the applied models often involve species with a smooth (lissencephalic) brain surface, such as mice. Thus, key cellular events that impact human-specific brain expansion and our understanding of how disease-linked mutations disrupt human cortical development remains elusive. Lissencephaly is a malformation of cortical development which is characterized by a smooth brain and a disorganized cortex. Heterozygous deletions or mutations in the LIS1 gene, encoding a microtubule-associated protein in humans, were identified to cause lissencephaly with diverse clinical phenotypic variations ranging from mild pachygyria (broad gyri) to severe agyria (no gyri) resulting in epilepsy and intellectual disabilities. While the clinical severity generally correlates with the degree of agyria, the location and type of mutation in the LIS1 gene does not. From LIS1 mouse models we know that LIS1 regulates the microtubule motor cytoplasmic dynein and by that dynein-dependent processes such as neuronal migration, nucleokinesis, interkinetic nuclear migration and mitotic spindle orientation. Even though the observed LIS1-deficiency-associated phenotypes appeared drastically milder in murine systems compared to humans these studies suggest that LIS1 gene dosage is relevant for the phenotypic severities. However, why a specific mutation within the LIS1 gene as identified in LIS1-lissencephalic patients (LIS1-patients) leads to different disease severities and whether human-specific processes during cortical development are differentially affected by the specific mutations could, due to a lack of adequate model systems, so far not been investigated. Here, I explore the ability to recapitulate different disease severities of LIS1-lissencephaly using LIS1-patient-specific iPS cells and thereof derived forebrain-type cerebral organoids. To do so, I selected from a LIS1-patient cohort comprising 63 cases 7 patients who cover the whole spectrum of gyrification alterations of LIS1-lissencephaly ranging from Dobyns grade 5 (mild) to 1 (severe). Each patient harbors a different molecular characterized heterozygous mutation in the LIS1 gene. To analyze the consequences of each LIS1 mutation on human brain development a 3D cell culture forebrain-organoid protocol was developed. Following reprogramming of patient-derived somatic cells and basic characterization (2 clones each) the iPS cells were applied to the organoid protocol. Organoids reproduced, in correlation with the patient's severity, alterations in organoid cytoarchitecture and premature neurogenesis. To assess the direct consequences of the patient-specific mutations on LIS1 microtubule stabilizing function I investigated the stability of the cytoskeleton of apical (a) RG cells within the cortical

ventricular-like zone (VZ) structures and found a progressive collapse of tubulin strand stability with increasing patient disease severity leading to a disruption of cellular organization. These phenotypic alterations could in part be reversed by stabilizing the microtubule array using the FDA-approved drug EpothiloneD. In addition, organoids from individuals with severe but not mild disease showed a non-random aRG cell division switch from proliferative to neurogenic division. As an underlying molecular cause, WNT-signaling alterations were identified, most prominently in severe conditions. To test to what extend perturbed WNT-signaling contributes to the observed patient-specific alterations, organoids were exposed to the GSK3ß inhibitor CHIR99021 leading to a significant rescue of non-random aRG cell division switch in severe organoids and to enlarged VZ diameters as well as reduced neurogenesis in all patient derived organoids.

The here demonstrated research underlines the capability of cerebral organoids to sensitively model individual disease severities, a so far not addressed major challenge of the system. My data show that different patient-specific mutations in the LIS1 gene have divergent direct impact on microtubule stability, which directly and/or indirectly lead to perturbed human corticogenesis providing the missing link between the patient-specific LIS1 mutation and the clinical severity grade. Future applications analyzing individual diseases have the potential to advance personalize medicine and improve the understanding of individual pathology for personalized therapy.

1. Unraveling the pathology of different disease severities in human cortical organoid models of LIS1-lissencephaly

To follow the here presented research, this chapter provides detailed information about the development of the human neocortex, including cytoarchitectural aspects as well as fundamental cell identities forming the 6-layered cortex. Furthermore, information about the essential WNT-signaling pathway, the cutting-edge organoid technology, the LIS1 protein and lissencephaly are given. Additionally, an overview of existing studies elucidating the question why a specific mutation within the LIS1 gene as identified in LIS1-patients leads to different disease severities is provided. At the end, the aims and objectives of this thesis are postulated in summary.

1.1. The developing cortex – cytoarchitecture and cell types

A precise choreography of progenitor proliferation, neurogenesis, neuronal migration and synaptogenesis forms the basis of human cortical development. The performance starts with a thin sheet of neural stem cells (NSC) founding the neuroepithelium. In the process of neuroepithelial thickening due to cell proliferation, the NSCs exceedingly elongate and transit to so called aRG cells (Bystron, Blakemore, and Rakic 2008). The next chorographical step comprises the formation of defined developmental zones distinctive by their cell types (Figure 1). Adjacent to the ventricle-forming lumen is the proliferative ventricular zone containing the bipolar aRG cells, which undergo internuclear migration (INM). The apical processes are anchored in the apical membrane and form adherent junctions, which are crucial for transducing morphogen signals from the cerebrospinal fluid. The basal processes of aRG cells are send to the pial surface to stabilize the radial organization of the developing cortex. Early in development aRG cells self-renew by symmetric cell division at the apical membrane, therefore increasing the aRG cells progenitor pool causing the expansion of the VZ. Later in development these progenitors start to divide asymmetrically, which can result in the direct generation of neurons or the production of intermediate cell populations including intermediate progenitors (IP) or bRG cells (also called outer RG cells) (Fietz et al. 2010; Hansen et al. 2010; Johnson et al. 2017). This precise orchestration of proliferation leads to the formation of the subventricular zone (SVZ), the intermediate zone (IZ) and the cortical plate (CP) (Figure 1). The SVZ contains the IPs and primate-specific bRG cells and is striking elaborated in primate cortical development (De Juan Romero and Borrell 2015; Borrell 2019). In contrast to aRG cells, bRG cells lack apical processes and are therefore not important for signal transduction at the apical membrane. These RG cell types may generate the majority of cortical neurons having a

tremendous proliferative potential (Lewitus, Kelava, and Huttner 2013). The IZ is a cell-poor region, which needs to be traversed by migrating neurons on their way to the CP to build up the 6-layered cortex in an inside-outer manner. This choreography of cortical development is choir mastered by distinctive signaling pathways, which regulate the self-renewal and differentiation of neuronal progenitors specifying their cell fates. One major signaling event is the evolutionary highly conserved WNT pathway.

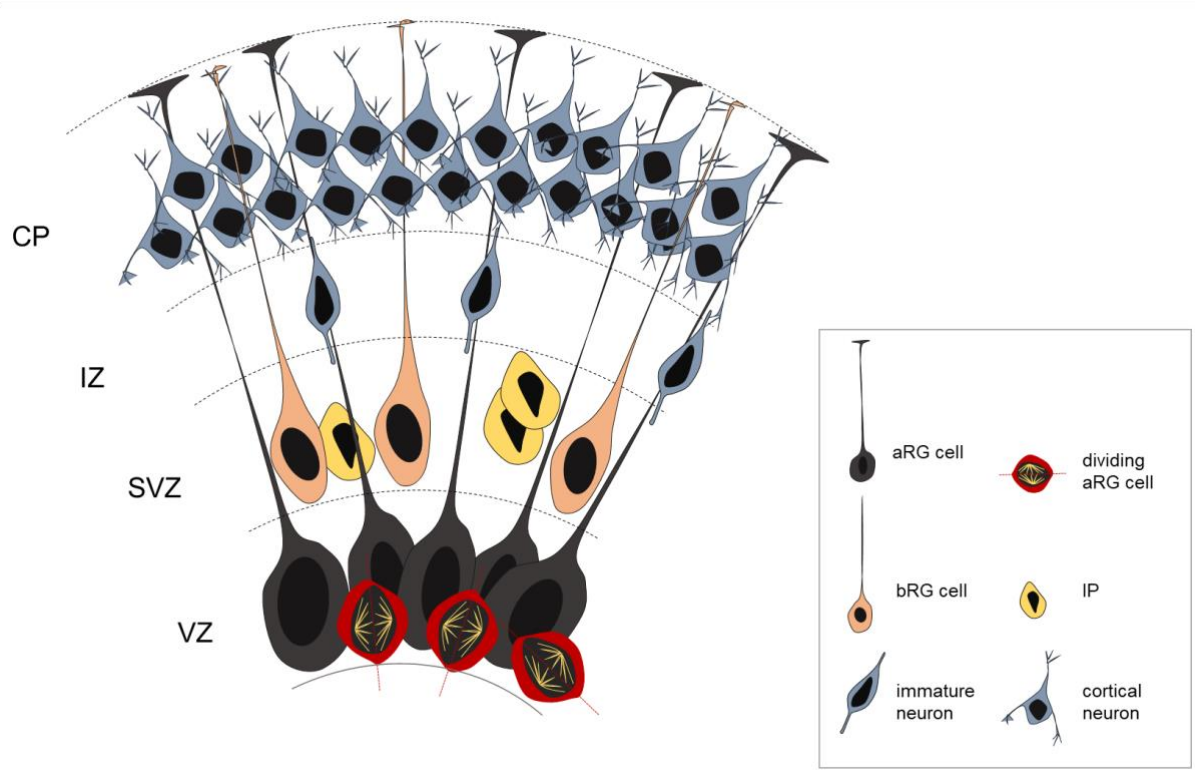

Figure 1: Illustration of the developing cortex. The developing cortex consists of distinctive developmental regions including the proliferative ventricular zone (VZ) containing the apical radial glia cells (aRG cell), the in primates highly expanded subventricular zone (SVZ) defined by intermediate progenitors (IP) and basal radial glia cells (bRG), the cell-poor intermediate zone (IZ) as wells as the cortical plate, which is migrated by differentiating neurons forming the developing 6-layered cortex.

1.2. WNT-signaling – a major choirmaster during embryogenesis

The WNT pathway is a major choirmaster in orchestrating embryogenesis including cell fate determination, cell migration, cell polarity, neural patterning, organogenesis and stem cell renewal (Komiya and Habas 2008). Discrete signaling centers release in a tightly regulated and spatially specific manner morphogens establishing regional identities. During forebrain development WNT-signaling from the cortical hem regulates the expansion and cell type

specification of the aRG cells and controls dorsal-ventral forebrain patterning in conjunction with BMP, FGF and SHH signaling (Harrison-Uy and Pleasure 2012). Subsequently, WNTs are crucial determinants for aRG cells division mode switch from self-renewing symmetric cell division to asymmetric cell proliferation leading to neurogenesis. Several signaling branches downstream of the WNT receptors have been identified including the canonical ß-CATENIN (ß-CAT) dependent) pathway as well as the non-canonical (ß-CAT independent) pathway. This project is focused on the canonical WNT pathway, where the secreted WNT ligands bind to the FRIZZLED (FZD)/ LOW-DENSITY LIPOPROTEIN RECEPTOR-RELATED PROTEIN (LRP 5/6) leading to the accumulation and translocation of adherents-junction associated-protein ß-CAT into the nucleus (Figure 2). In the absence of WNT morphogens, a so-called destruction complex composed of AXIN, ADENOMATOSIS POLYPOSIS COLI (APC), GLYCOGEN SYNTHASE KINASE (GSK 3) and CASEIN KINASE 1a (CK 1a) leads to the degradation of ß-CAT (Gordon and Nusse 2006). The phosphorylation of ß-CAT by GSK 3ß and CK 1a leads to the ubiquitination and subsequent proteolytic destruction by the proteasomal machinery (He et al. 2004; Aberle et al. 1997). The presence of WNTs leads to FZD and LRP 5/6 complex formation, which induces the membrane translocation of AXIN, a key negative regulator of WNT-signaling. GSK 3ß and CK 1a phosphorylate LRP 5/6 promoting the binding of AXIN to the co-receptor. Furthermore, WNT activation leads to the recruitment of another negative regulator, the phosphoprotein DISHEVELLED (DSH), which is also known to bind to AXIN and FZD to inhibit GSK 3ß. It is still unresolved how DSH is activated (Kishida et al. 1999). This complex formed at the membrane at FZD/ LRP 5/6 prevents the degradation of ß-CAT and consequently leads to the stabilization and accumulation in the cytoplasm enabling a translocation in the nucleus to activate WNT target genes (Figure 2). ß-CAT signaling leads for example to the expansion of the cerebral precursor population and cortical surface area enlargement (Woodhead G., Mutch C. A., Olson E. C 2006). Additionally, to remark is that there is recent evidence that cell adherent-junctions protein N-CADHERIN (N-CAD) impacts WNT/ß-CAT signaling. Adherent junctions have an important role in signal transduction from the cerebrospinal fluid into the aRG cells during cortical development. It has been shown that N-CAD interacts with AXIN and LRP 5/6 to negatively regulate WNT/ß-CAT signaling in osteoblasts by decreasing the soluble cytoplasmic tool through binding ß-CAT at the membrane (Hay et al. 2009; Marie and Hay 2013). In addition, cadherins are also required for augmented activation of the WNT/ß-CAT pathway during epithelial-mesenchymal transition (Howard et al. 2011). Furthermore, Zhang et al. showed that AKT activation by N-CAD impacts ß-CAT and neuronal differentiation during cortical development in a cell-autonomous fashion (J.

Zhang et al. 2013). AKT signaling is crucial for multiple organ developmental processes. How N-CAD promotes the phosphorylation of AKT remains largely unknown, there is evidence that N-CAD adhesion cause phosphatidylinositol 3-kinase (PI3K)-mediated activation of AKT (Tran et al. 2002). Downstream signaling of AKT includes direct phosphorylation of ß-CAT at residue Serine 552, which stabilize the soluble cytosolic form. Moreover, AKT inhibits the negative regulator of ß-CAT, GSK 3ß, by phosphorylation at Serine 9 leading also to stabilization and nuclear accumulation of ß-CAT. How exactly AKT and WNT-signaling are regulated during neural development and the underlying mechanisms through which AKT and WNT mediate cortex development remains elusive. To shed more lights on the complex signaling choreography during corticogenesis further intensive research needs to be done. To face such human developmental questions the young field of 3D organoid cell culture has emerged as very promising tool.

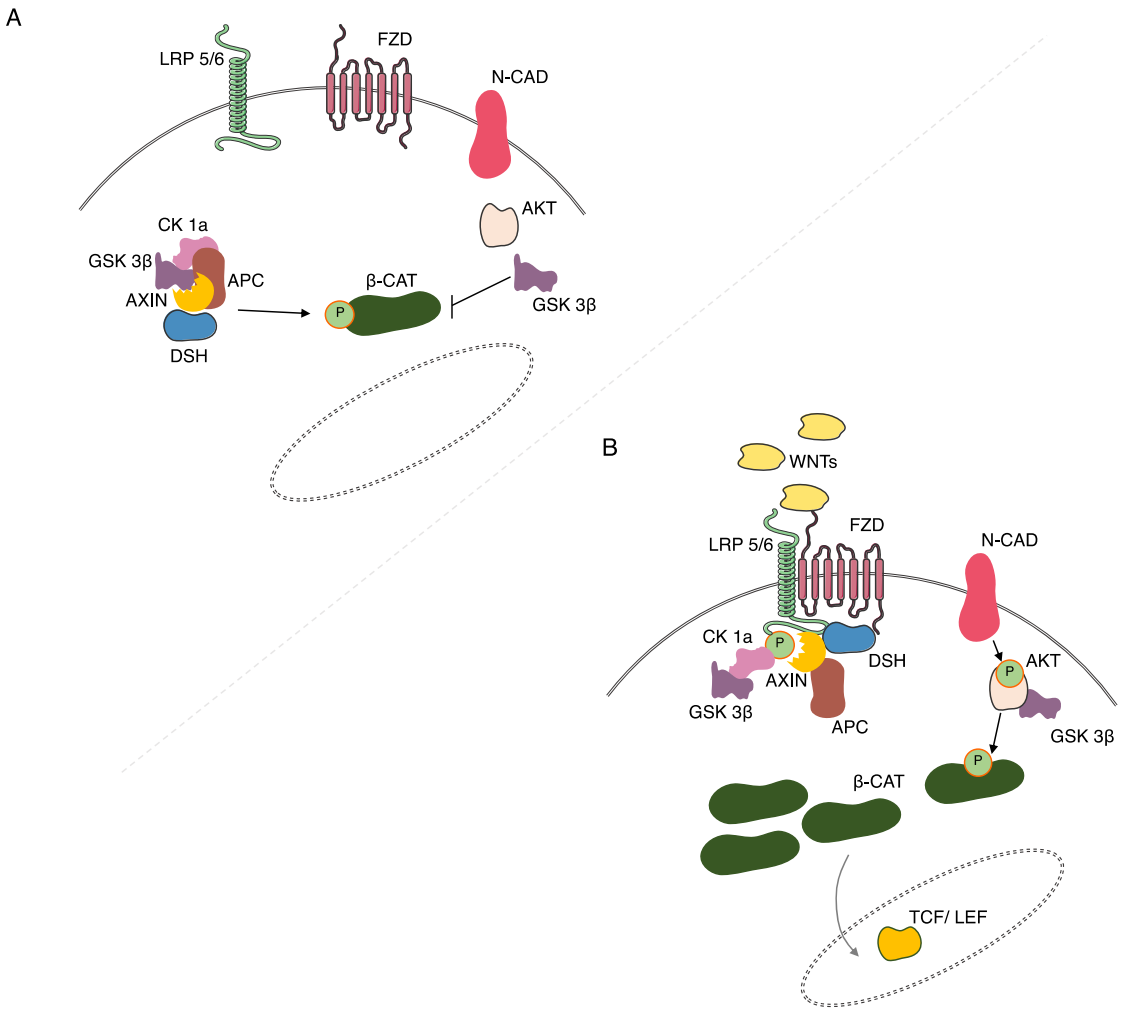

Figure 2: Illustration of the canonical WNT-signaling cascade. (**A**) In the absence of WNTs the destruction complex composed of AXIN, ADENOMATOSIS POLYPOSIS COLI (APC), GLYCOGEN SYNTHASE KINASE 3ß (GSK 3ß) and CASEIN KINASE 1a (CK 1a) primes the phosphorylation of ß-CATENIN (ß-CAT) by GSK 3ß and CK 1a leading to the ubiquitination and subsequent proteolytic destruction by the proteasomal machinery. (**B**) In the presence of WNTs FRIZZLED (FZD) and LOW-DENSITY LIPOPROTEIN RECEPTOR-RELATED PROTEIN (LRP 5/6) are forming a complex, which induces the membrane translocation of AXIN. GSK 3ß and CK 1a leading to the phosphorylation of LRP 5/6, which promotes the binding of AXIN together with the destruction complex to the co-receptor. Furthermore, WNT activation leads to the recruitment of DISHEVELLED (DSH), which is also known to bind to AXIN and FZD to inhibit GSK 3ß. This complex formed at the membrane at FZD/ LRP 6 prevents the degradation of ß-CAT and consequently leads to the stabilization and accumulation in the cytoplasm enabling a translocation into the nucleus to active WNT target genes including TRANSCRIPTIONFACTOR (TCF)/ LYMPHOID ENHANCER-BINDING FACTOR (LEF). ß-CAT is also positive regulated by AKT signaling through direct phosphorylation at residue Serine 552 or through the inhibition of the negative regulator GSK 3ß, by phosphorylation at Serine 9. In addition, there is recent evidence that N-CADHERIN (N-CAD) is involved in the canonical WNT-signaling pathway.

1.3. Cerebral organoids – cutting edge technology

Human developmental processes have always been most challenging to understand due to fetal tissue inaccessibility and the lack of *in vitro* model systems. Early human corticogenesis and its precise choreography remains largely elusive. Within the last decade the field of 3D cell cultures have emerged as a promising tool to model organ development *in vitro* facilitating completely new perspectives in understanding embryogenesis. Since the pioneer work from Yoshiki Sasai (Eiraku et al. 2008) paved the way, organoid technology has made one of the most rapid advances in the field of cell biology. Potential applications can not only include embryogenesis, the field of tissue regeneration as well as drug screening can also be covered by organoid research. Here, I focus on brain organoids of cortical identity to analyze malformation of cortical development (MCD). Cortical organoid development started in 2008 when Eiraku et al. (Eiraku et al. 2008) differentiated iPS cells aggregates under serum free conditions, so called SFEBq (short for: serum-free floating cultures of embryoid body-like aggregate with quick reaggregation) showing apico-basally polarized cortical tissue with spatially organization including VZ, SVZ and a CP-like regions. The real organoid hysteria started in 2013, when Madeline Lancaster and coworkers from the Knoblich laboratory (M. Lancaster et al. 2013) described cerebral organoids containing multiple brain regions like retina, choroid plexus, midbrain, hindbrain and forebrain tissue. At the same time also the Saisai laboratory (Kadoshima et al. 2013) contributed to the organoid publicity by further improving the SFEBq approach and introducing the rolling

morphogenesis of region-specific cortical organoids. From that time on various of publications aimed to improve organoid culture protocols to faithfully recapitulate specific aspects of human brain development, all using the self-organizing capacity of iPS cells (Paşca et al. 2015; Camp et al. 2015; X. Qian et al. 2016; Watanabe et al. 2016; Iefremova et al. 2017; Renner et al. 2017; Karzbrun et al. 2018). My coworkers and me also developed a reproductible forebrain-type organoid protocol leading to highly homogenous cultures within and across organoid batches (Krefft et al. 2018; Iefremova et al. 2017) (outlined in Figure 6). Like most of the cortical region-specific organoid protocols, it is based on an iPS cell aggregation phase, followed by a cortical induction phase by small molecule pathway modulators including SMAD signaling inhibitors to counteract mesoderm and endoderm differentiation and WNT-signaling inhibitors to evade posterization (Chambers SM, Fasano CA, Papapetrou EP, Tomishima M, Sadelain M 2009). Further differentiation includes stabilization and enhancement of the organoids cortical VZ structure architecture by extracellular matrix (ECM) embedding. The nutritive support and the oxygen exchange are enriched through constant agitation on a shaker. Additionally, at later timepoints, further molecules and growth factors are implanted to promote the formation of the developmental zones distinctive by their cell types over a time course up to 100 days (Figure 3). After 20 days of differentiation, organoids show remarkable similarities in cell composition and cytoarchitecture to its *in vivo* counterparts including an aRG cell pool with apico-basal polarity and few IPs representing early gestation period (Figure 3). Prolonged differentiation leads to cortical structures including a VZ with aRG cells, SVZ containing IPs and bRG cells as well as a cortical-plate like regions showing diverse layer-specific neurons denoting the first to second gestation trimester (Figure 3). Important to consider is that organoids are still an artificial system missing for example cells form other germ layers such as endothelia cells or microglia. It still needs to be addressed to what extend organoids have the same degree of complexity as their *in vivo* organs. Impressively, single-cell transcriptomics revealed significant resemblances in cell composition in accordance to different developmental stages with impressive intersection of their transcription profile comparing to *in vivo* brain cells (Camp et al. 2015; Kanton et al. 2019). In the future, the innovative single-cell sequencing technique will hopefully provide a depth understanding of spatiotemporal gene expression trajectories in cortical organoids shedding more light on the degree of correlation between organoids and *in vivo* organs (Marsoner, Koch, and Ladewig 2018). It is undeniable that organoids already enormously improved *in vitro* research. The advantage of *in vivo*-like cell-cell interactions as well as human-specific cell populations such as bRG cells already

elevates *in vitro* research in terms of mimicking physiological cell behavior on a completely different level compared to 2D cell culture. Previously inaccessible aspects of human corticogenesis can be elucidated *in vitro* without the need of fetal tissue. Not only in health but also in disease. The complexity of the human brain has made it difficult to study many MCDs in model organisms like mice. MCD-associated phenotypes often show a reduction or absence of gyrification limiting the use of natural lissencephalic brains and suggesting that MCD causing human genes might have gained new functions compared to their mouse orthologs. We, and also the Kriegstein laboratory modeled the Miller-Dieker Syndrome (MDS), a severe lissencephaly, in cortical organoids to address pathophysiological changes (Bershteyn et al. 2016; Iefremova et al. 2017). We could identify human-specific non-cell autonomous disruption in WNT-signaling, leading to perturbations in aRG cells division modes (Iefremova et al. 2017). The Kriegstein laboratory (Bershteyn et al. 2016) showed MDS pathophysiological defects in bRG cells in the SVZ. Moreover, cortical organoids displayed a useful tool to model the impact of infectious disease on cortical development like the relatively recent outbreak of the ZIKA virus leading to microcephaly (X. Qian et al. 2016; Cugola et al. 2016; H. et al. 2018; Janssens et al. 2018; Dang et al. 2016; Garcez et al. 2016; Wells et al. 2016). The sensitivity of cortical organoids to model different disease severities and analyze individual pathologies has not been examined yet. This project explored the ability to recapitulate different disease severities of LIS1-lissencephaly using mild, moderate and severe affected LIS1-patient specific iPS cells and thereof derived forebrain-type cerebral organoids.

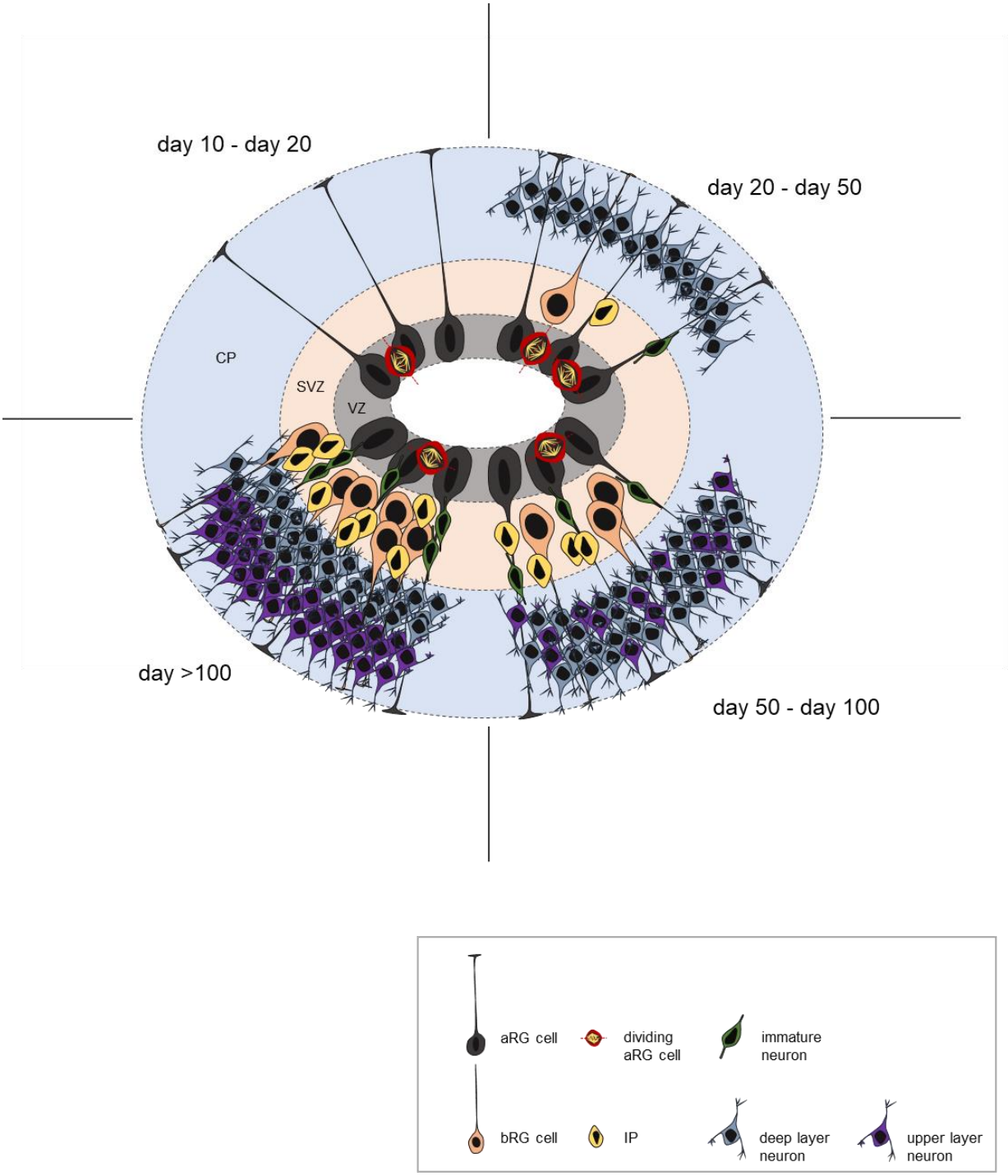

Figure 3: Scheme of maturing organoid and timepoint depend cytoarchitecture. At the timepoint of matrix embedding and differentiation the organoid mainly consists of apical radial glia (aRG) cells. In the next 10 days aRG cells divide symmetrically and increase their progenitor pool, so that the organoid ventricular zone structures expand and consist at day 20 mainly of aRG cells. Between day 20 and day 50 aRG cells start to divide asymmetrically, leading to the generation of intermediate progenitors (IP) and neurons, which form the subventricular-like zone (SVZ) and the cortical plate-like structure (CP). The human-specific basal radial glia (bRG) cells start to emerge around day 50 within the SVZ. Prolonged differentiation leads to organoid ventricular structures containing deep and upper layer neurons.

1.4. Lissencephaly – a rare second group MCD

MCDs were first grouped in 1996 as disorders resulting from disturbance of the normal developmental processes of the human cerebral cortex causing a wide range of developmental disorders (Barkovich A.J., Kuzniecky R.I., Dobyns W.B., Jackson G. D. 1996). Depending on the appearance of the first developmental abnormalities, these disorders were classified into 3 major classes (Barkovich et al. 2005, 2012a; Desikan and Barkovich 2016). The first group includes those disorders thought to be caused by abnormal progenitor cell proliferation or apoptosis such as microcephaly (reduced brain size) and macrocephaly (abnormal large brain), while the second group is compost of those cases believed to be largely caused by alterations in neuronal migration including lissencephaly (smooth brain) as well as heterotopia (abnormal displaced neurons leading to cytoarchitecture alterations). The third described group includes malformations secondary to abnormal postmigrational development, such as polymicrogyria (overfolding and abnormal lamination of the cortex). This project focuses on lissencephaly, a heterogenous spectrum of MCDs associated with a smooth brain and a disorganized thickened cortex (Francis et al. 2006; Barkovich et al. 2012b). Patients suffer from mental retardation and untreatable epilepsy (Aronica, Becker, and Spreafico 2012; Guerrini and Dobyns 2017). Continuous advancement of molecular genetics has led to the identification of many lissencephaly-related genes, most are related to microtubule structural proteins (tubulin) or microtubule-associated proteins (MAPs). LIS1 was the first gen associated with this MCD (Dobyns et al. 1993; Reiner et al. 1993).

1.4.1. LIS1 – an indispensable protein

Sporadic heterozygous mutations in the human LIS1 gene, also called PAFAH1B1 (short for: platelet-activating factor acetylhydrolase isoform1B, α subunit) cause lissencephalic brains with different severe gyrification alterations. The protein is a homodimer, made of a N-terminal dimerization domain and a C-terminal ß-propeller structure, which is important for protein interactions (Figure 4).

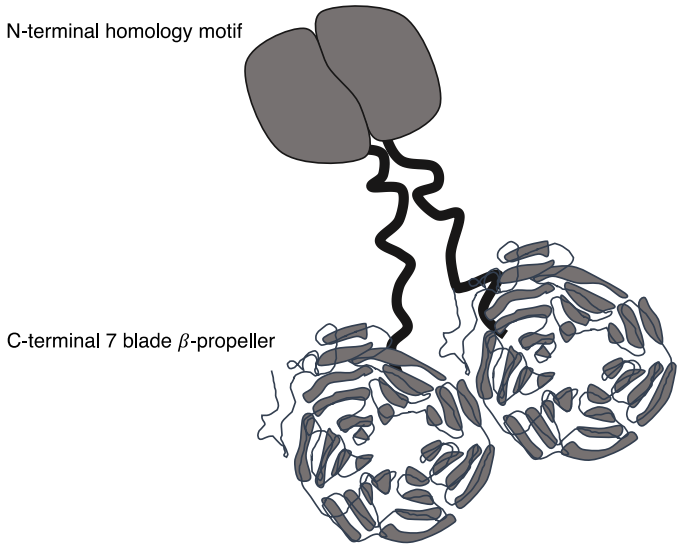

Figure 4: Scheme of the wildtype LIS1 protein dimer conformation. The N-terminal homology motif is important for dimerization and the C-terminal 7 blade β-propeller structure is indispensable for protein interactions.

LIS1 is assigned to 2 main cellular functions. Originally, it was identified as a stoichiometric component of PAFAH1b functioning as enzyme in the deactivation of the lipid messenger platelet-activating factor. However, mice null for the catalytic subunit of PAFAH1b showed normal brain development (Koizumi et al. 2003; Yan et al. 2003). Consequently, there had to be an additional function of LIS1 causing lissencephaly. Because of the lethality of LIS1 null mice, it became precipitously clear that LIS1 is an essential gene during brain development (Hirotsune, Gambello, et al. 1998; Cahana et al. 2001). The reduction of LIS1 dosage led to migration defects in mice causing dosage-depended cellular disorganization of cortical layers, hippocampus, cerebellum and olfactory bulb (Hirotsune, Fleck, et al. 1998; Gambello, Darling, Yingling, Tanaka, Gleeson, and Wynshaw-boris 2003; Tanaka et al. 2004). The necessity of LIS1 for correct neuronal migration has been also shown by direct examination of neuronal migration in mouse embryonic brain slice cultures, which were *in utero* transfected with green fluorescent protein to label migrating neurons (Shu et al. 2004). Using RNAi knockdown of LIS1 undoubtfully demonstrated that LIS1 is required of neuronal migration and that LIS1 deficiency leads to neuronal migration defects associated with lissencephaly (Shu et al. 2004; Tsai J, Chen Y, Kriegstein A 2005; Youn et al. 2009). Consequently, LIS1-lissencephaly was long time considered to be a neuronal migration disorder. However, to date it is known that the underlying disease triggers are characterized by a broader spectrum of disease-causing pathology also including progenitor abnormalities like mitotic spindle formation as well as perturbed radial glial cell proliferation (Tsai J, Chen Y, Kriegstein A 2005; Tanaka et al. 2004;

N. E. Faulkner et al. 2000; Yingling et al. 2008). Extended mouse studies showed an additional role of LIS1 in cell proliferation during neurogenesis as well as for neuronal survival (Gambello, Darling, Yingling, Tanaka, Gleeson, and Wynshaw-Boris 2003). LIS1 knock-down was associated with impaired neural stem cell division (Tsai J, Chen Y, Kriegstein A 2005). Already Tanaka et al. (Tanaka et al. 2004) showed that LIS1 is required for nuclear movement during neuronal migration by coupling the nucleus to the centrosome. In fact, to date there are multiple publications confirming the function of LIS1 as important DYNEIN regulator (Nicole E Faulkner et al. 2000; Smith et al. 2000; Huang et al. 2012; Toropova et al. 2014; Mi Moon and Wynshaw-boris 2013; DeSantis et al. 2017; Sasaki et al. 2000). Tai and colleagues (Tai et al. 2002) showed that the interaction is substoichiometric and occurs through 3 distinct sites within DYNEIN's cargo binding domain and the motor domain. Moreover, Faulkner et al. found (N. E. Faulkner et al. 2000) that LIS1 is co-localized with cytoplasmic DYNEIN at the mitotic kinetochores indicating a role of LIS1 in chromosomal behavior. Microinjections of anti-LIS1 antibody caused delay in mitotic progression as well as chromosomal defects at the metaphase during mitosis (N. E. Faulkner et al. 2000; Moon et al. 2014). Additionally, it was shown that LIS1 is also localized at the marginal area of the developing cortex in NES cells. The overexpression led to mitotic spindle disorganization potentially caused by reduction of DYNEIN distribution pointing out the importance of DYNEIN/ LIS1 interactions for the regulation of spindle orientation (N. E. Faulkner et al. 2000). It was also shown that LIS1 deficient mice had 80 % thinner and severely disorganized cortices due to reduced numbers of progenitors, potentially caused by a failure of mitotic spindle function (Pawlisz et al. 2008). This was further shown by Yingling et al. (Yingling et al. 2008) by using a Cre-loxP strategy to induce a complete loss of LIS1 in defined spatial-temporal patterns in NES- and RG cells. The loss of LIS1 in NES cells completely diminished those cell population, whereas loss of LIS1 in RG cells resulted in depletion of progenitors without catastrophic loss. They proposed a model to explain these findings, saying, that the cleavage planes early in development in the NES cells are tightly controlled to a vertical (symmetric) division to produce daughter cells both becoming progenitor cells. Explaining the massive cell loss when LIS1 deficiency leads to incorrect spindle orientation. Whereas in RG cells later in development, when more spindle planes are orientated horizontally (asymmetric) LIS1 deficiency leads to the reduction of progenitors and the decrease of neuron production resulting in a smaller brain size, but without catastrophic consequences (Yingling et al. 2008). Moreover, they postulated that due to the LIS1 function of cortical microtubule capture and stability resulting from its function in DYNEIN regulation, LIS1 stabilizes microtubules by plus-end capture at the cell cortex via

localization of DYNEIN components, providing an explanation for the spindle orientation defects in LIS1 deficient NES and RG cells (Yingling 2008). It is also to add that LIS1-lissencephlic mouse models also helped to elucidate the question how LIS1 deficiency results in defects of cortical DYNEIN localization. It is postulated, that LIS1 mediates anterograde transport of cytoplasmic DYNEIN to the plus-end of cytoskeletal microtubules as a complex on transportable microtubules (Masami Yamada et al. 2013). Consequently, LIS1 deficiency would lead to impaired plus-end directed DYNEIN transport and accumulation around the centrosome associated with peripheral depletion leading to nucleokinesis defects displayed by migrating neurons (Tanaka et al. 2004). In addition, one mouse study rescued cortical DYNEIN localization and phenotypic LIS1 mutant defects by inhibiting LIS1 degradation by intra-peritoneal injection of ALLN, a calpain inhibitor, rescuing apoptotic neuronal cell death, reduction of brain weight as well as neuronal migration defects (M. Yamada et al. 2009). Important interaction partners of LIS1 to regulate cytoplasmic Dynein are NUDE (also known as NDE1) and its isoform NUDEL (also known as NDEL1) (Kitagawa et al. 2000; Niethammer et al. 2000; Morris et al. 1998) also found in Aspergillus through the ortholog interaction of NUDF (Efimov and Morris 2000). The physiological necessity for such a complex interaction network is poorly understood. It can be assumed that the complexity in interactions relates to a precise control of DYNEIN activity, which plays a role in all microtubule-depend processes, but how exactly LIS1 regulates DYNEIN is not known yet. Mesngon and colleagues (Mesngon et al. 2006) reported that LIS1 causes some stimulation of DYNEIN ATPase activity. Concluded it is to say that LIS1-lissencephaly is not just, as traditionally considered, an isolated neuronal migration disorder (Mi Moon and Wynshaw-boris 2013). LIS1 is imperative for microtubule-dynamic processes, which are fundamental important for the correct function of neuronal progenitor dynamics during cortical development (Bizzotto and Francis 2015). Recent data clearly highlights an important role of LIS1 in various progenitor-depended processes like mitotic progression, altered spindle orientation and consequently defects in aRG cells division mode leading to incorrect timing of neurogenesis (Tsai J, Chen Y, Kriegstein A 2005; Yingling et al. 2008; Francis et al. 2006).

1.4.2. LIS1-lissencephaly – a disorder displaying multiple faces

Heterozygous deletions or mutations in the LIS1 gene are most common to cause lissencephaly in humans (Kato M. 2003). LIS1-lissencephaly includes isolated lissencephaly sequence (ILS, also known as classical or type I lissencephaly), MDS and very rarely subcortical band heterotopia (SBH) (Dobyns and Das 2014). This study focuses on ILS, which

is caused by *de novo* mutations in the LIS1 gen, including small intragenic deletions or insertions as well as point mutations. Common MRI LIS1 phenotypes include an anomalous thickened cortex of 12-20 mm (normal 3-4mm) and absent or abnormally broad cerebral gyri (Barkovich, Koch, and Carrol 1991). Those phenotypes are seen in vastly different severe manifestations (Figure 5). Dobyns and Truwit (Dobyns and Truwit 1995) established a grading system of gyral malformation including agyria (grade 1), mixed agyria-pachygyria (grades 2 and 3) and pachygyria (grades 4 to 6) to better define several recognized subtypes according to their MRI phenotype (Pilz et al. 1998; Dobyns and Truwit 1995) (outlined in Figure 5).

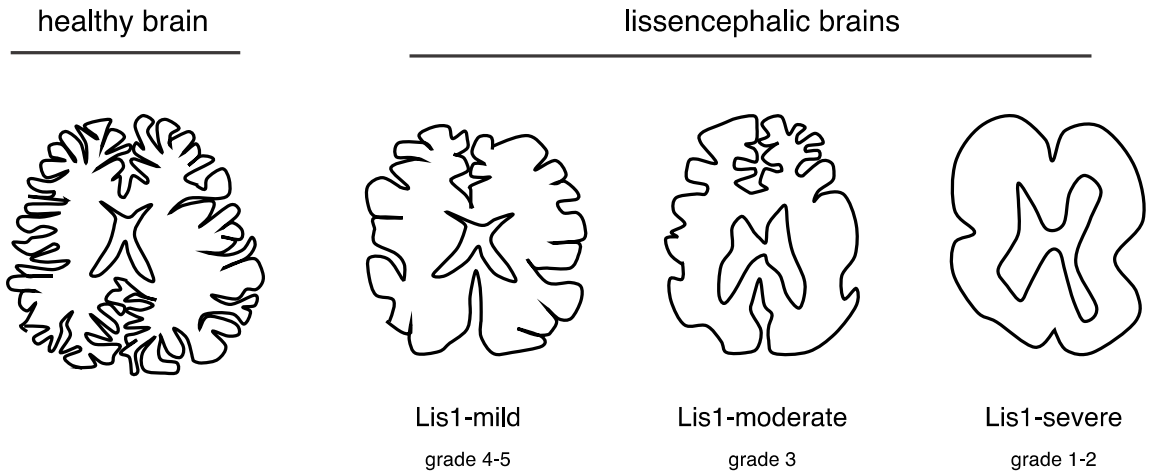

Figure 5: Scheme of the lissencephalic severity spectrum. The healthy primate brain is characterized by multiple folds, so called gyri and sulci. This gyrification developed evolutive by the expansion of the neocortex. One of the main phenotypes of lissencephalic brains is a reduction of gyrification, which occurs in different severities. The milder phenotypes are characterized by broader gyri. Moderate lissencephalic brains often show a gradient of severity from anterior to posterior with anterior pachygyria and posterior agyria. The most severe lissencephalic phenotypes are characterized by the complete absents of gyrification (smooth brain).

The clinical severity generally correlates with the degree of agyria, but not with the LIS1 gene mutation (Saillour et al. 2009). Much of our knowledge about LIS1-lissencephaly comes from post-mortem analyzes of patient's brains, which provided valuable insight into neuropathological condition. However, such tissue represents the final stage of disease and cannot be used to analyze the development of MCD or causative mechanisms. Pre- and prenatal imagine might provide more detailed information on disease progression, however, not permit functional studies. The translation into mouse models has generated fundamental insight into the pathological mechanisms associated to the disease phenotype (Collins et al. 2019; Uzquiano et al. 2019; Chevassus-Au-Louis et al. 1999; Mi Moon and Wynshaw-boris 2013). The basic sequence of events during corticogenesis are commonly shared across species making mouse

models a well-suited system to unravel neurodevelopmental disorders. Transgenic mice represent a powerful tool for examining genetic mechanisms. Consequently, several mouse models of lissencephaly were created based on LIS1 protein dosage variations, leading to the identification of many molecular functions of the LIS1 protein (see 1.4.1). However, many phenotypes observed in humans are not recapitulated in non-human models, highlighting severe difference in development, the structure of the brain and gene function between human and non-human models. One example is the healthy lissencephalic mouse brain, which is an imperative restriction when analyzing lissencephalic disorders, failing to recapitulate the severity of human-specific phenotypes. Even though these studies could show that LIS1 gene dosage is relevant for the phenotypic severities. However, the impact of specific mutations within the LIS1 gene as identified in LIS1-patients on alterations of human-specific processes during cortical development was so far not investigated. Therefore, to overcome those structural and technical hurdles iPS cells derived cerebral organoids have emerged as an attractive tool to model and study human-specific aspects of MCDs recapitulating the 3D cytoarchitecture, cell composition and spatial organization reminiscing of early human brain development (M. A. Lancaster et al. 2017; Camp et al. 2015; Kanton et al. 2019). This study elucidates whether cerebral organoids are sensitive to recapitulate variable disease severities to analyze individual pathologies for personalized medicine.

1.5. The variable phenotypic manifestations of LIS1-lissencephaly – an unsolved phenomenon

To date little is known about the underlying pathologies leading to the diverse LIS1-lissencephalic severities. Mouse models have unraveled many molecular pathologies but failed to capture disease severity. Therefore, studies utilizing human and patient-specific model systems are needed for severity cause elucidation. A more in-depth understanding is important as it may lead to more specific approaches to comfort and help affected children. Multiple clinical case studies describe that there is no correlation between disease causing LIS1 mutation and patients disease severity. Neither the mutation type nor the location of the mutation within the LIS1 gene were found to predict the severity grade of LIS1-lissencephaly (Saillour et al. 2009; Uyanik et al. 2007; Philbert et al. 2017; Pilz et al. 1998). There are known cases were the same mutation leads to different disease severities (oral communication, Nadja Bahi-Buisson). That raises the question in how far the genetic plays into pathology. Are environmental factors or any by-chance effects involved or is it mainly the degree of LIS1-function disruption which determines disease severity. Initially, one publication suggested a putative correlation with the

mild lissencephaly associated missense mutations and truncating mutations localized at the 3' end of the LIS1 gene (Cardoso et al. 2000). Although more recent studies did not confirm this relationship (Uyanik et al. 2007; Saillour et al. 2009). Saillour et al. (Saillour et al. 2009) analyzed a large LIS1-patient cohort including 40 patients carrying LIS1 mutations (75%) or small deletions (20%). They tried unsuccessfully to correlate the severity of the disease in terms of epileptic seizures, radiological findings, and body movement impairments with the LIS1 mutations. Moreover, Uyanik et al. (Uyanik et al. 2007) revealed 21 intragenic mutations distributed over the entire LIS1 gene. Except 2 mutations in the LIS1 homology domain and 2 in the region encoding the coiled-coil domain were all found in one of the seven WD40 repeat domains. But neither the type nor the position of the mutation correlated with a particular phenotype. Rather, they found that the clinical severity correlates only with the degree of agyria and cortical thickening, which supports the statement of Barkovich and colleagues already in 1991 (Barkovich, Koch, and Carrol 1991). Due to the lack of accessibility of patient's brain, it is difficult to analyze molecular pathologies in living cells. Post-mortem analyzes show the final stage of disease but are not suitable for functional studies or disease progression analysis leading to disease heterogeneity. To date there are only a few studies analyzing LIS1-lissencephalic severity cause in human *in vitro* models. Early on, in 1999, Fogli et al. (Fogli et al. 1999) did genotype-phenotype correlations of 7 patients with classical lissencephaly carrying a heterozygous LIS1 splice-site or truncation mutation. The patient harboring a splice-site mutation suffered from more severe disease than the patients with LIS1 truncation mutation. Using lymphoblastoid cell lines of those patients, they found that patient cells containing the splice-site mutation were suggestive of partial protein synthesis from the mutated allele, whereas cells harboring truncation LIS1 mutation did not show detectable protein translation. Consequently, their data propose that the intracellular dosage of the LIS1 protein correlates with the severity, which was also shown by murine studies (Y. H. Youn et al. 2009; Gambello, Darling, Yingling, Tanaka, Gleeson, and Wynshaw-Boris 2003). Caspi et al. (Caspi et al. 2003) analyzed different LIS1 point mutations by examining protein stability, folding, intracellular localization and protein-protein interactions by utilizing *in vitro* models. Their data suggest that the mutated proteins were affected at different levels and no single assay could be used to predict the lissencephalic phenotype. They found that the cellular phenotype of cells, expressing mutant proteins that retain partial folding and interactions may be modified by overexpression of specific LIS1 interacting proteins. These findings implicate that there are probably different biochemical and cellular mechanisms obstructed in each patient yielding the varied lissencephaly phenotypes. Our collaboration

partners (Philbert et al. 2017, Camille Maillard, unpublished Data) analyzed fibroblasts of 4 LIS1-patients including 2 patients characterized by mild disease, grade 4-5, as well as 2 patients suffering from severe disease, grade 1-2. The analysis of LIS1 mRNA levels in patient fibroblasts showed that wildtype transcript levels from those 4 patients (mild and severe) are reduced by approximately half compared to controls due to the heterozygous mutations. But only the mutant transcript levels from patients with mild disease, carrying a frameshift, are degraded by non-sense mediated decay (NMD), as shown by inhibition of NMD by Emetine. In contrast, mutant transcripts of patients with severe disease, with in-frame missense mutation, are not degraded, so that the missense mutation would lead to misfolded proteins in the severe patients, which might be degraded by the proteasome. By proteasomal inhibition they (Philbert et al. 2017, Camille Maillard, unpublished Data) found clusters of LIS1 in cells from patients with severe disease, in which mutant transcripts are not degraded. Cells from patients with mild disease did not show this phenomenon supporting the assumption that only cells from severe patients contain misfolded protein variants. They further hypothesized that the observed LIS1 clusters in severe conditions might be stress granules (SG), which are cytosolic membrane-less organelles that form temporarily, allowing the cell to bear a cellular stress by stalling mRNA translation and enhancing the synthesis of cytoprotective proteins (J.-Y. Youn et al. 2019). This hypothesis was supported by fibroblast treatment with sodium arsenate, a cellular stressor, and co-labeling of LIS1 and G3BP1, a SG marker. Moreover, they found that LIS1 clusters are observed only after MG132 treatment, suggesting LIS1 mutant proteins are misfolded and then degraded by proteasome. These findings suggest that the wildtype transcript reduction by 50 % together with the 50 % of misfolded proteins are more harmful to the cell physiology than only the 50 % wildtype transcripts as found in cells from patients with mild disease. To further elucidate potential underlying pathologies leading to disease severity heterogeneity in neuronal progenitors and during brain development, fibroblasts (and lymphocytes) of the 4 patients (mild, severe) named above as well as cells from 2 additional patients suffering from moderate disease were send to me for reprogramming into iPS cells and 3D *in vitro* disease modelling.

1.6. Aims and research objectives

MCDs are the consequence of alterations in the precise choreography of progenitor proliferation, neurogenesis and neuronal migration during corticogenesis. LIS1-lissencephaly is a heterogeneous MCD. To date little is known about the molecular origin for such lissencephalic heterogeneity and no effective treatment is available. LIS1 mouse models show that LIS1 gene dosage is relevant for the phenotypic severities. However, the impact of specific mutations within the LIS1 gene as identified in LIS1-patients on alterations of human-specific processes during cortical development was so far not investigated. Therefore, the here presented project had the main aim to shed light on the underlying pathology leading to different lissencephalic disease severities caused by LIS1 mutations. To do so 7 patients were selected from a LIS1-patient cohort comprising 63 cases who cover the whole spectrum of gyrification alterations of LIS1-lissencephaly ranging from Dobyns grade 5 (mild) to 1 (severe). Somatic cells of those patients (all harboring heterozygous mutation in the LIS1 gene) were reprogrammed and 2 clones for each LIS1-patient iPS cell line characterized. To analyze specific early human developmental aspects in the different lissencephalic conditions a reproducible protocol for the generation of homogenous human cerebral forebrain-type organoids was developed. Furthermore, to analyze the mutational consequences on human cortical development the ability of my 3D organoid models to sensitively recapitulate different disease severities of LIS1-lissencephaly should be explored. To that end, I also planned to develop precise quantitative assessment protocols to detect phenotypic differences sensitively and accurately in the developed 3D *in vitro* model systems. Moreover, I had the intention to use my 3D organoid models for unraveling molecular pathologies, which might be specific for the different disease severities. The last major aim was to identify substances, which counteract *in vitro* disease phenotypes as potential candidates for disease therapy.

Summarized, to shed more light on lissencephalic disease heterogeneity following aims arise:

I. To generated and characterize a large LIS1-patient iPS cell cohort which covers the whole spectrum of gyrification alterations of LIS1-lissencephaly.

II. To develop an *in vitro* cortical forebrain-type organoid protocol to reconstruct cortical stem cell niche and analyze corticogenesis in health and disease.

III. To design quantitative 3D organoid assessment protocols to precisely compare healthy and different disease severity conditions.

IV. To test the sensitivity of the established 3D organoid system to mirror different disease severities and reflect LIS1-lissencephaly associated phenotypes.

V. To investigate underlying molecular pathology in the LIS1-patient derived organoids from different disease severities.

VI. To identify substances, which counteract LIS1-lissencephlic associated phenotypic alterations.

2. Materials

This study was completed at the Hector Institute of Translational Brain Research (HITBR) headed by Prof. Dr. Philipp Koch. All used cell lines, technical equipment, consumables as well as chemicals, cell culture media, enzymes, buffers, solutions, primers, antibodies and software are listed in this section. The entire experiments were completed in compliance with Germany's legal provisions and ethical guidelines and the 'Declaration of Helsinki – Ethical Principles for Medical Research Involving Human Subjects' from the World Medical Association. The employment of all human cell lines was in full ethical agreement with institutional regulations.

2.1. Cell lines

The cell lines used in this study included fibroblasts, peripheral blood mononuclear cells (PBMCs) and iPS cells. Control skin fibroblasts were obtained from Coriell Biorepository (control 1, 2-year-old female, catalog ID GM00969; control 2, 5-month old male donor, catalog ID GM08680). LIS1-patient fibroblasts and lymphocytes were collected and send from Nadja Bahi-Buisson from the Necker Enfants Malades university hospital in France (mild LIS1-patient 1, 8-year old male donor, c.569-10T>C LIS1 mutation; mild LIS1-patient 2, 5-years old male donor, c.569-10T>C LIS1 mutation; moderate LIS1-patient 1, 6-years old female donor, c.13del LIS1 mutation; moderate LIS1-patient 2, 13-year old female donor, delEx11 LIS1 mutation; severe LIS1-patient 1, 4-year old female donor, c.1002+1G>A; severe LIS1-patient 2, 18-year old female donor, c.531G>C LIS1-mutation; severe LIS1-patient 3, 3-year old female donor, c.445>T LIS1 mutation, see table 1). iPS cell lines were generated with patient consent, and this study was ethically approved. In additional 4 control iPS cell lines were received from Dr. Sandra Horschitz (Ethics Committee II of Medical Faculty Mannheim of Heidelberg University approval no. 2014-626N-MA, control 3, 21-years old female donor; control 4, 44-year old female donor; control 5, 25-year old female donor; control 6, 26-year old female donor).

Table 1: Overview of LIS1-lissencephaly patients including age, sex, mutation and severity grade.

	mild P1	mild P2	moderate P3	moderate P4	severe P5	severe P6	severe P7
age	8	5	6	13	4	18	3
sex	male	male	female	female	female	female	female
mutation	c.569-10T>C	c.671-10T>G	c.13del	delEx11	c.1002+1G>A	c.531G>C	c.445>T
severity grade	4-5	4-5	3	3	1-2	2	1-2

Table 2: Generated LIS1-patient iPS cell lines and utilized control iPS cell lines

Cell line	Source
control C 1.1	Coriell Biorepository, catalog.ID GM00969 (2-year-old female donor)
control C 1.2	Coriell Biorepository, catalog.ID GM00969 (2-year-old female donor)
control C 2.1	Coriell Biorepository, catalog.ID GM08680 (5-month-old male donor)
control C 2.2	Coriell Biorepository, catalog.ID GM08680 (5-month-old male donor)
control C 3.1	Sandra Horschitz, HITBR Mannheim (21-year-old female donor)
control C 3.2	Sandra Horschitz, HITBR Mannheim (21-year-old female donor)
control C 4.1	Sandra Horschitz, HITBR Mannheim (44-year-old female donor)
control C 4.2	Sandra Horschitz, HITBR Mannheim (44-year-old female donor)
control C 5.1	Sandra Horschitz, HITBR Mannheim (25-year-old female donor)
control C 5.2	Sandra Horschitz, HITBR Mannheim (25-year-old female donor)
control C 6.1	Sandra Horschitz, HITBR Mannheim (26-year-old female donor)
control C 6.2	Sandra Horschitz, HITBR Mannheim (26-year-old female donor)
mild LIS1-patient P1.1	Olivia Krefft, HITBR Mannheim, Germany (8-year-old male donor)
mild LIS1-patient P1.2	Olivia Krefft, HITBR Mannheim, Germany (8-year-old male donor)
mild LIS1-patient P2.1	Olivia Krefft, HITBR Mannheim, Germany (5-year-old male donor)
mild LIS1-patient P2.2	Olivia Krefft, HITBR Mannheim, Germany (5-year-old male donor)
moderate LIS1-patient P3.1	Olivia Krefft, HITBR Mannheim, Germany (6-year-old female donor)
moderate LIS1-patient P3.2	Olivia Krefft, HITBR Mannheim, Germany (6-year-old female donor)
moderate LIS1-patient P4.1	Olivia Krefft, HITBR Mannheim, Germany (13-year-old female donor)
moderate LIS1-patient P4.2	Olivia Krefft, HITBR Mannheim, Germany (13-year-old female donor)
severe LIS1-patient P5.1	Olivia Krefft, HITBR Mannheim, Germany (4-year-old female donor)
severe LIS1-patient P5.2	Olivia Krefft, HITBR Mannheim, Germany (4-year-old female donor)

severe LIS1-patient P6.1	Olivia Krefft, HITBR Mannheim, Germany (18-year-old female donor)
severe LIS1-patient P6.2	Olivia Krefft, HITBR Mannheim, Germany (18-year-old female donor)
severe LIS1-patient P7.1	Olivia Krefft, HITBR Mannheim, Germany (3-year-old female donor)
severe LIS1-patient P7.2	Olivia Krefft, HITBR Mannheim, Germany (3-year-old female donor)

2.2. Technical equipment

All used technical equipment is listed in this section.

Table 3: Technical equipment

Device	**Manufacture**
10X Vortex Adapter	10X Genomics (San Francisco, USA)
10X Magnetic Separator	10X Genomics (San Francisco, USA)
2100 Bioanalyzer Laptop Bundle	Agilent (Waldbronn, Germany)
4200 Tape station	Agilent (Waldbronn, Germany)
Analytical Balance BP121-S	Sartorius Stedim Biotech S. A. (Aubagne Cedex, France)
Centrifuge 5415D	Eppendorf AG (Hamburg, Germany)
Centrifuge Z 216 MK	HERMLE Labortechnik GmbH (Wehingen, Germany)
Chromium Controller	10X Genomics (San Francisco, USA)
Chromium Next GEM Secondary Holder	10X Genomics (San Francisco, USA)
CO_2 Incubator HERAcell 150i	Thermo Fisher Scientific Inc. (Waltham, Massachusetts, USA)
Confocal Microscope Leica TCS SP5II	Leica Microsystems GmbH, (Mannheim, Germany)
Electrophoresis Power Supply EPS 301	Amersham Pharmacia Biotech (Little Chalfont, UK)
Extraction hood mc6® das Laborsystem	Waldner GmbH & Co (Wangen, Germany)
Fluorescence Microscope Axioskop 2 plus	Zeiss Microscopy GmbH (Oberkochen, Germany)

Fluorescence Microscope Celldiscoverer 7	Zeiss Microscopy GmbH (Oberkochen, Germany)
Fluorescent Lamp ebq 100	Lighting & Electronics Jena GmbH, (Jena, Germany)
Fragment Analyzer Automated CE System 12, and 48/96 cap	Advanced Analytical Technologies (Heidelberg, Germany)
Heraeus Sorvall Four Place Swinging Bucket, Rotor 6445	Thermo Fisher Scientific Inc. (Waltham, Massachusetts, USA)
Heraeus® Herasafe™ 2030i Biological Safety Cabinet	Thermo Fisher Scientific Inc. (Waltham, Massachusetts, USA)
Heraeus® Labofuge® 400R Centrifuge	Thermo Fisher Scientific Inc. (Waltham, Massachusetts, USA)
HiSeq 4000 Sequencing system	Illumina (San Diego, USA)
Illumina Nova Seq 6000 system	Illumina (Berlin, Germany)
Inverted Leica DMIL LED Microscope	Leica Microsystems GmbH, (Mannheim Germany)
Light-Sheet-Microscope	Leica Microsystems GmbH, (Mannheim Germany)
LUNA™ Automated cell counter	Logos Systems (Weilerswist, Germany)
Micro Balance iso9001	Sartorius Stedim Biotech S. A. (Aubagne Cedex, France)
MilliQ Integral Water Treatment System	Merck Millipore (Burlington, Massachusetts, USA)
MJ Research PTC-200 Thermal Cycler	Biozym Diagnostik GmbH (Oldendorf, Deutschland)
Nanodrop™ ND-1000 Spectrophotometer	Thermo Fisher Scientific Inc. (Waltham, Massachusetts, USA)
Neurolog System Stimulator Module	Digitimer LLC (Ft. Lauderdale, Florida, USA)
NovaSeqTM 6000 sequencing system	Illumina (San Diego, USA)
Odyssey Imaging System	Li-Cor Bioscience (Bad Homburg vor der Höhe, Germany)
Orbital shaker KS 250 basic	IKA Labortechnik ® GmbH, staufen (Germany)

pH-Meter Profi Lab WTW pH597	SIGMA-ALDRICH (St. Louis, Missouri, USA)
Quant Studio 7 Flex	applied Biosystems by Thermo Fisher Scientific Inc. (Waltham, Massachusetts, USA)
Qubit 4.0 Fluorometer	Thermo Fisher Scientific Inc. (Waltham, Massachusetts, USA)
Sunlab Roll Mixer SU 1400	Sustainable lab instruments (Heidelberg, Germany)
Thermal Cycler C1000 Touch (with 96-deep well reaction module)	Bio-Rad Laboratories (Essen, Germany)
Thermal MasterCycler Pro	Eppendorf AG (Hamburg, Deutschland)
Thermal Cycler MJ Research PTC-200	Biozym Scientific GmbH (Hessisch Oldendorf, Germany)
Termal Cycler Veriti (96-well)	Thermo Fisher Scientific Inc. (Waltham, Massachusetts, USA)
Thermomixer comfort 5355	Eppendorf AG (Hamburg, Deutschland)
UV lamp GeneFlash	Syngene (Cambridge, UK)
Vortex Reax control	Heidolph Instruments GmbH & CO. KG, Schwabach (Germany)
Warm bath ED-17	JULABO Labortechnik GmbH (Seelbach, Deutschland)
Warm bath for cell culture	Köttermann GmbH & Co. KG (Uetze/Häningsen, Germany)

2.3. Plastic ware

All used plastic ware is listed in this section.

Table 4: Plastic ware

Product	**Manufacturer**
Cell Scrapper 16 cm	SARSTEDT AG & Co. KG, (Nümbrecht, Germany)
Coverslips 12, 15 mm Ø	VWR International (Radnor, Pennsylvania, USA)
CryoPure Tubes 1 ml	SARSTEDT AG & Co. KG (Nümbrecht, Germany)

Disposable bag	SARSTEDT AG & Co. KG (Nümbrecht, Germany)
DNA LoBind Tubes 1,5 and 2 ml	Eppendorf (Hamburg, Germany)
Eppendorf tubes 0,1, 0,5, 1,5 and 2 ml	SARSTEDT AG & Co. KG, (Nümbrecht, Germany)
Falcons 15, 50 ml	SARSTEDT AG & Co. KG, (Nümbrecht, Germany)
Flowmi Strainer P1000 Pipette Tip, 40 uM	Bel-Art SP Scienceware™ (New jersey, USA)
Frame Star 96 well semi-skirted PCR Plate	4titude (Wotton, UK)
Glass Pasteur pipettes	Thermo Fisher Scientific Inc. (Waltham, Massachusetts, USA)
Imaging 35 mm Ø dish, polymer coverslipbottom	Ibidi GmbH (Martinsried, Germany)
MicroAmp 8-Tube Strip 0,2 ml	Thermo Fisher Scientific Inc. (Waltham, Massachusetts, USA)
MicroAmp 8-Cap Strip, clear	Thermo Fisher Scientific Inc. (Waltham, Massachusetts, USA)
Micropipettes 1000, 200, 100, 20, 10, 2 µl	ABIMED GmbH (Langenfeld, Deutschland)
Microscope slides 76x26 mm	Carl Roth GmbH & Co. KG (Karlsruhe, Deutschland)
Nitrile Powder-Free Gloves	ABENA®, Culver City (USA)
Parafilm M	Pechiney Plastic Packaging (Chicago, USA)
Pasteur pipettes	Alpha Laboratories Limited (Hampshire, UK)
PCR Seal	4titude (Wotton, UK)
PCR Single Cap 8-Soft Strips, 0,2 ml	Biozym Scientific GmbH (Hessisch Oldendorf, Germany)
PCR Tubes 0,2 ml 8-tube stripes	Eppendorf (Hamburg, Germany)
Petri-dishes 60x15 mm and 100x15mm with Nocken	SARSTEDT AG & Co. KG (Nümbrecht, Germany)
Pipet tips 1000, 200, 20, 10 µl	SARSTEDT AG & Co. KG, (Nümbrecht, Germany)
Serological Pipets, 50, 25, 10, 5 ml	SARSTEDT AG & Co. KG, (Nümbrecht, Germany)

TC 6, 12, 24, 96 Well-Cell Culture Plate, Standard F	SARSTEDT AG & Co. KG, (Nümbrecht, Germany)
TempAssure PCR 8-tube strip	USA Scientific (Ocala, USA)
Ultralow Cluster, 96-well plate, ultra-low attachment round bottom with lid	Costar® by SIGMA-ALDRICH (St. Louis, Missouri, USA)

2.4. Cell culture consumables

This section contains all information what cell culture consumables have been used within this study including compounds, chemicals and media compositions.

2.4.1. Cell culture compounds and chemicals

All used compounds and chemicals are listed in this section.

Table 5: Cell culture compounds and chemicals

Product	**Manufacturer**
A83-01	Tocris (Wiesbaden, Germany)
B27® Supplement (50X)	Gibco® Thermo Fisher Scientific Inc. (Waltham, Massachusetts, USA)
BSA solution (7.5%)	SIGMA-ALDRICH (St. Louis, Missouri, USA)
BDNF	Peprotech (Hamburg, Germany)
cyclisches adenosin-monophosphat (cAMP)	SIGMA-ALDRICH (St. Louis, Missouri, USA)
CHIR99021	Cell Guidance Systems Ltd (Cambridge, UK)
D-Glucose	SIGMA-ALDRICH (St. Louis, Missouri, USA)
DMEM (1X) + GlutaMAX™-I	Gibco® Thermo Fisher Scientific Inc. (Waltham, Massachusetts, USA)
DMEM/F-12 (1:1) (1X) + L-Glutamine	Gibco® Thermo Fisher Scientific Inc. (Waltham, Massachusetts, USA)
DMEM/F-12 (1:1) (1X) + L-Glutamine + HEPES	Gibco® Thermo Fisher Scientific Inc. (Waltham, Massachusetts, USA)
DMSO	SIGMA-ALDRICH (St. Louis, USA)
Dorsomorphin	Stem Cell Technologies (Cologne, Germany)
Dulbecco´s Phosphate Buffered Saline	SIGMA-ALDRICH (St. Louis, Missouri, USA)

EDTA	SIGMA-ALDRICH (St. Louis, Missouri, USA)
Epothilone D	SIGMA-ALDRICH (St. Louis, Missouri, USA)
Fetal bovine serum (FBS)	Invitrogen (Waltham, Massachusetts, USA)
FLT3	Gibco® Thermo Fisher Scientific Inc. (Waltham, Massachusetts, USA)
GDNF	Cell Guidance Systems Ltd (Cambridge, UK)
Gelantine	SIGMA-ALDRICH (St. Louis, Missouri, USA)
GelTrex™ (GT)	Gibco® Thermo Fisher Scientific Inc. (Waltham, Massachusetts, USA)
GlutaMAX™-I (100X)	Gibco® Thermo Fisher Scientific Inc. (Waltham, Massachusetts, USA)
Heparin	SIGMA-ALDRICH (St. Louis, Missouri, USA)
HEPES	Carl Roth GmbH & Co. KG (Karlsruhe, Deutschland)
Human FGF-2 (154)	Cell Guidance Systems Ltd (Cambridge, UK)
Human recombinant bFGF	Invitrogen (Waltham, Massachusetts, USA)
Human Recombinant Insulin	SIGMA-ALDRICH (St. Louis, Missouri, USA)
Human TGF-β1	Cell Guidance Systems Ltd (Cambridge, UK)
Interleukin 3 (IL-3)	Gibco® Thermo Fisher Scientific Inc. (Waltham, Massachusetts, USA)
Interleukin 6 (IL-6)	Gibco® Thermo Fisher Scientific Inc. (Waltham, Massachusetts, USA)
Knockout™-Serum Replacement (KOSR)	Gibco® Thermo Fisher Scientific Inc. (Waltham, Massachusetts, USA)
L-Ascorbic Acid	Cell Guidance Systems Ltd (Cambridge, UK)
L-Ascorbic Acid 2-Phosphate (LAAP)	SIGMA-ALDRICH (St. Louis, Missouri, USA)
L-Tryptophan	SIGMA-ALDRICH (St. Louis, Missouri, USA)
Laminin	Gibco® Thermo Fisher Scientific Inc. (Waltham, Massachusetts, USA)
LDN-193189	StemMACS™ (Bergisch Gladbach, Germany)
LM22A	SIGMA-ALDRICH (St. Louis, Missouri, USA)
LM22B 10	Tocirs (Wiesbaden, Germany)
MEM Non-Essential Aminoacids (NEAA),	Gibco® Thermo Fisher Scientific Inc.

(100X)	(Waltham, Massachusetts, USA)
2-Mercaptoethanol	Invitrogen (Waltham, Massachusetts, USA)
Natrium chloride (NaCl)	SIGMA-ALDRICH (St. Louis, Missouri, USA)
Natrium selenite (NaSe)	SIGMA-ALDRICH (St. Louis, Missouri, USA)
Penicillin Streptomycin 10,000 units/ml	Gibco® Thermo Fisher Scientific Inc. (Waltham, Massachusetts, USA)
PluriPro	Cell Guidance Systems Ltd (Cambridge, UK)
Pluronic	SIGMA-ALDRICH (St. Louis, Missouri, USA)
Poly-L-ornithine	SIGMA-ALDRICH (St. Louis, Missouri, USA)
Progesterone	SIGMA-ALDRICH (St. Louis, Missouri, USA)
Purmorphamine	Cell Guidance Systems Ltd (Cambridge, UK)
Puromycin	PAA (Pasching, Austria)
Putrescine	SIGMA-ALDRICH (St. Louis, Missouri, USA
Rho-Kinase-Inhibitor Y-27632 (Rock Inhibitor)	Cell Guidance Systems Ltd (Cambridge, UK)
Stem cell factor (SCF)	Gibco® Thermo Fisher Scientific Inc. (Waltham, Massachusetts, USA)
Transferrin	SIGMA-ALDRICH (St. Louis, Missouri, USA)
Trypan blue	Invitrogen (Waltham, Massachusetts, USA)
TrypLE Express	Gibco® Thermo Fisher Scientific Inc. (Waltham, Massachusetts, USA)
Trypsin-EDTA (10X)	Gibco® Thermo Fisher Scientific Inc. (Waltham, Massachusetts, USA)
Trypsin inhibitor (TI)	Gibco® Thermo Fisher Scientific Inc. (Waltham, Massachusetts, USA)
UltraPure™ EDTA	Invitrogen (Waltham, Massachusetts, USA)
XAV 939	Enzo (Lörrach, Germany)

2.4.2. Cell culture media composition

All base media were ordered from Life Technologies (Karlsruhe) and supplemented with 1X Penicillin/Streptomycin (Pen/Strep). The compounds and small molecules where added according to the listed concentrations. The complete cell culture media were stored at 4°C and used within 4 weeks. Directly after cell passaging all media were supplemented with 5mM Rock inhibitor Y-27632 (Rock inhibitor) for 1 day.

Table 6: Cell culture media

Medium	Composition	Concentration
Freezing medium	KOSR	70%
	Cytobuffer	20%
	DMSO	10%
E8 base medium	DMEM/F-12 (1:1) (1X) + L- Glutamine + HEPES	
	LAAP	0,64 mg/ml
	NaSe	28 nM
E8 complete medium	E8 base medium	
	Human recombinant insulin	10 µg/ml
	FGF-2 (154)	1 ng/ml
	H-Transferrin	2 µg/ml
	TGF-β1	10 ng/ml
HBS solution (2X)	NaCl	280 mM
	HEPES	50 mM
	$Na_2HPO*7H_2O$ (pH 7,05)	1,42 mM
	add 10 M NaOH to pH 7,05	add
Human ES cell medium	Knockout™-Serum Replacement (KOSR)	
	KOSR	1:5000,
	NEEA	1X
	GlutaMax	1X
	β-Mercaptoethanol	55 µM
	bFGF	4 ng/ml
	Pen/Strep	1X
Maturation medium	Neuronal differentiation medium	

	LM22A	1µM
	LM22B	1µM
	GDNF	10 nM
	Ascorbic acid	0,2 mM
	GelTrex	1:500
Mouse Embryonic Fibroblast (MEF) medium	DMEM (1X) + GlutaMAX™-I	
	FCS	10 %
	Pyruvat	1 %
	NEEA	1%
	Pen/Strep	1X
N2/B27 base medium	DMEM/F-12 (1:1) (1X) + L-Glutamine	
	N2 supplement	1X
	B27® Supplement	1X
	β-Mercaptoethanol	0,1 nM
	cAMP	1,5 µg /ml
	D-Glucose	0,4 µg/ml
	NEEA	1X
	GlutaMax	1X
	Pen/Strep	1X
N2 Supplement	DMEM (1X) + GlutaMAX™-I	
	H-Transferrin	2 mg/ml
	Human recombinant insulin	0,5 mg/ml
	Putrescine	1,6 µg/ml
	Progesterone	0,6 µm/ml
	NaSe	0,5 µg/ml
Neuronal differentiation medium	N2/B27 base medium	
	KOSR	1:50
	Human recombinant insulin	2,5µg/ml
Neuronal induction medium	N2/B27 base medium	
	Heparin	10 µg/ml

	LDN	180 nM
	A83	500 nM
	XAV	10 µg/ml
PBMC medium	StemPro34 medium	
	SCF	100 ng/ml
	FLT3	100 ng/ml
	IL-3	20 ng/ml
	IL-6	20 ng/ml
PluriPro (PP) medium	PluriPro	99 %
	Pen/Strep	1%
PP/E8 medium	PP	50 %
	E8 complete medium	50 %
StemPro34 medium	DMEM (1X) + GlutaMAX™-I	
	StemPro Supplement (50X)	1X
	BSA (25%)	2%
	GlutaMax	1X
	β-Mercaptoethanol	55 µM
	bFGF	4 ng/ml
Wash medium	DMEM (1X) + GlutaMAX	99 %
	Pen/Strep	1 %

2.5. Molecular biology consumables

This section contains all information what molecular biology consumables have been used within this study including compounds, chemicals and solution compositions.

2.5.1. Molecular biology compounds and chemicals

This section provides information about molecular compounds and chemicals used within this study.

Table 7: Molecular compounds and chemicals

Product	**Manufacture**
30% Acryl-bisacryl-amide	SIGMA-ALDRICH (St. Louis, Missouri, USA)
Agarose	SIGMA-ALDRICH (St. Louis, Missouri, USA)
Ammersham™ Hybond™ 0,2µm PVDFB Blotting Membrane	Healthcare Life Science (Freiburg, Germany)
Ammoniumperoxodisulfat (APS)	SIGMA-ALDRICH (St. Louis, Missouri, USA)
Calcium chloride ($CaCl_2$)	SIGMA-ALDRICH (St. Louis, Missouri, USA)
Cell staining buffer for Cell Hashing	BioLegend (Koblenz, Germany)
Chloroform	SIGMA-ALDRICH (St. Louis, Missouri, USA)
DAPI	SIGMA-ALDRICH (St. Louis, Missouri, USA)
ddH_2O	Merck Millipore (Burlington, Massachusetts, USA)
DNA 100 bp ladder	New England Biolabs (Ipswich, New England, USA)
dNTPs	Peqlab GmbH (Erlangen, Germany)
Eosin G-Lösung 0,5% wässrig	Carl Roth GmbH & Co. KG (Karlsruhe, Deutschland)
Ethanol ≥99.8 %	SIGMA-ALDRICH (St. Louis, Missouri, USA)
FCS	Invitrogen (Waltham, Massachusetts, USA)
Galantine	SIGMA-ALDRICH (St. Louis, Missouri, USA)
U-shaped 2.5 mm glass capillaries	Hilgenberg (Malsfeld, Germany)
Glucose	Carl Roth GmbH & Co. KG (Karlsruhe, Deutschland)
Glycerol	Merck (Burlington, Massachusetts, USA)
Hämalaunlösung sauer nach Mayer	Carl Roth GmbH & Co. KG (Karlsruhe, Deutschland)
HEPES	Carl Roth GmbH & Co. KG (Karlsruhe, Deutschland)
Horse serum	Thermo Fisher Scientific Inc. (Waltham, Massachusetts, USA)
Human TruStain FcX Blocking Solution for Cell Hashing	BioLegend (Koblenz, Germany)
Isopropanol	SIGMA-ALDRICH (St. Louis, Missouri, USA)
Loading Dye	New England Biolabs (Ipswich, New England, USA)
Low melting agarose	Cambrex Bio Science (Wiesbaden, Germany)
Low TE Buffer (10 mM Tris-HCl pH 8,0,	Thermo Fisher Scientific Inc.

0,1 mM EDTA)	(Waltham, Massachusetts, USA)
Mowiol	SIGMA-ALDRICH (St. Louis, Missouri, USA)
N,N,N',N'-Tetrakis(2-hydroxypropyl)-ethylenediamine	TCl Chemicals (Eschborn, Germany)
Nuclease-free H_2O	Thermo Fisher Scientific Inc. (Waltham, Massachusetts, USA)
PeqGreen	Peqlab GmbH (Erlangen, Germany)
Paraformaldehyde (PFA)	SIGMA-ALDRICH (St. Louis, Missouri, USA)
Potasium Chloride (KCl)	AppliChem GmbH (Darmstadt, Germany)
Phosphatase inhibitor	Thermo Fisher Scientific Inc. (Waltham, Massachusetts, USA)
Protease inhibitor	Thermo Fisher Scientific Inc. (Waltham, Massachusetts, USA)
Qiagen Buffer EB	Qiagen (Hilden, Germany)
RNASE Away	Molecular Bioproducts Inc. (Leicestershire, UK)
Saponin	SIGMA-ALDRICH (St. Louis, Missouri, USA)
Sodium chloride (NaCl)	SIGMA-ALDRICH (St. Louis, Missouri, USA)
Sodium citrate ($Na_3C_6H_5O_7$)	SIGMA-ALDRICH (St. Louis, Missouri, USA)
Sucrose	SIGMA-ALDRICH (St. Louis, Missouri, USA)
TAE Buffer (10X)	SIGMA-ALDRICH (St. Louis, Missouri, USA)
ThermoPol® Reaction Buffer Pack	New England Biolabs (Ipswich, New England, USA)
TriFast peqGOLD	Peqlab GmbH (Erlangen, Germany)
Tris-Tricine-SDS Buffer (10X)	SIGMA-ALDRICH (St. Louis, Missouri, USA)
Triton X-100	SIGMA-ALDRICH (St. Louis, Missouri, USA)
Tween 20	Bio-Rad Laboratories (Hercules, California, USA)
Type F Immersion Oil	Leica Microsystems GmbH, (Mannheim, Germany)
Urea	SIGMA-ALDRICH (St. Louis, Missouri, USA)
WypAll X60 Wipes	Kimberly-Clark Professional™ (Koblenz, Germany)

2.5.2. Molecular biology buffer and solution compositions

All used molecular buffers and solutions are listed in this section.

Table 8: Molecular buffer and solution composition

Buffer	Composition	Concentration
3M Tris-HCl/ SDS Buffer	Tris base	182 g
	HCl to pH 8.45	add
	dH_2O to 500 ml	add
	SDS	1,5 g
6X SDS-PAGE Sample Buffer	Tris 375 mM, pH 6,8	25 ml
	10 % SDS solution	60 ml
	Glycerol 6%	6 ml
	β-Mercaptoethanol 9 %	9 ml
	Bromphenol-blue-solution 9 %	0,03 g
10% APS	Ammonium persulfate	1 g
	dH_2O to 10 ml	add
10X Anode buffer	Tris base 1M	242 g
	add HCl to pH 8,8	add
	dH_2O to 1000 ml	add
10X TBS	NaCl (150mM)	87,6 g
	Tris (50mM)	60,5 g
	add HCl to pH 7,4	add
	dH_2O to 1000 ml	add
50x Tris-acetate-EDTA-buffer (TAE)	Tris	242 g
	EDTA solution (0.5M; pH 8.5)	100 ml
	Water-free acetic acid (100%)	57.1 ml
	dH_2O to 1000ml	add
Blotting Transfer buffer	Glycine	2,9 g
	Tris	5,8 g

	SDS	0,37 g
	Methanol	200 ml
	dH_2O to 1000ml	add
Clearing blocking solution	Horse serum	10%
	Gelantine	0,2%
	Triton X-100	0,1%
	PBS	add
Cryo-embedding medium	PBS	82,5 %
	Sucrose	10 %
	Gelantine	7,5 %
dNTP Mix	dATP	25 mM
	dTTP	25 mM
	dCTP	25 mM
	dGTP	25 mM
HBS solution (2X)	NaCl	280 mM
	HEPES	50 mM
	$Na_2HPO*7H_2O$ (pH 7,05)	1,42 mM
	add 10 M NaOH to pH 7,05	add
Immuno-blocking solution	PBS	89,9 %
	FCS	1 %
	Triton X100 (only for intracellular epitopes)	0,1 %
Lysis buffer	Tris HCl	50 mM
	NaCl	50 mM

	EDTA	1 mM
	Triton™ X-100	1%
	HCl to 7.4	add
	Protease inhibitor	1 tablet/ ml
	Phosphatase inhibitor	1 tablet/ ml
Mounting solution	Tris solution (0.2 M; pH 8.5)	12 ml
	H2O	6 ml
	Glycerol	6 g
	Moviol	2.6 g
	DABCO	0.1 g
PCR master mix solution	Taq Buffer	2,5 µl
	$MgCl_2$	0,75 µl
	dNTPs (100mM, 25mM each dNTP)	0,2 µl
	Primer (1:10)	1,0 µl
	DNA	1,0 µl
	GoTaq G2 Flexi DNA polymerase	0,2 µl
	dH_2O to 25 µl	add
PFA fixation solution (4%)	PFA	40 g
	dH_2O	1000 ml
Protein loading buffer	Tris solution (0.1 M; pH 6.8)	75.75%
	Glycerol	20%
	SDS	4%
	Bromphenol blue	0.25%

ScaleCUBIC-1 solution	N,N,N',N'-Tetrakis(2-hydroxypropyl)-ethylenediamine	25%
	Triton X-100	15%
	Urea	25%
	in dH_2O	add
SDS-PAGE separation gel solution (10%)	3M Tris-HCl/ SDS, pH 8.45	13,33 ml
	30% acrylamide	13,33 ml
	50% glycerol	8,00 ml
	10% ammonium perlsulfat (APS)	112 µl
	TEMED	37µl
	dH_2O to 40 ml	add
SDS-PAGE stacking gel solution (4%)	3M Tris-HCl/ SDS, pH 8.45	4,96 ml
	30% acrylamide	2,56 ml
	10% ammoniumperlsulfat (APS)	134,4 µl
	TEMED	44,8 µl
	dH_2O to 20 ml	add
SDS-PAGE gel solution buffer	Tris solution (1.5M; pH 6.8)	99.6%
	SDS	0.4%
TBST-buffer	10X TBS	100 ml
	Tween 100X	1 ml
	H_2O to 1000 ml	add

2.6. Enzymes

All used enzymes are listed in this section.

Table 9: Molecular enzymes

Enzyme name	Manufacturer
Alkaline Phosphatase, Shrimp	Roche Diagnostics (Penzberg, Germany)
Dnase I (molecular biology)	Invitrogen (Karlsruhe, Germany)
Go Taq G2 Flexi DNA polymerase	Promega (Mannheim, Germany)
Phusion High Fidelity DNA Polymerase	New England Biolabs (Frankfurt, Germany)
T4 DNA Ligase	New England Biolabs (Frankfurt, Germany)
Taq DNA Polymerase, recombinant	Invitrogen (Karlsruhe, Germany)

2.7. Plasmids

All used plasmids are listed in this section.

Table 10: Molecular plasmids

Plasmid name	Source
Lentiviral-TOP-dGFP-reporter	Addgene plasmid #14715; Reya et al Nature. 2003 May 22. 423(6938):409-14.
Viral packing vector psPAX2	Addgene plasmid #12260
Viral packing vector pMD2.G	Addgene plasmid #12259

2.8. Kits

All used kits are listed in this section.

Table 11: Molecular kits

Kit	Manufacturer
CTS™ CytoTune™-iPS 2.1 Sendai Reprogramming Kit	Thermo Fisher Scientific Inc. (Waltham, Massachusetts, USA)
DNase I Amplification Grade	SIGMA-ALDRICH (St. Louis, Missouri, USA)
Dneasy Blood and Tissue Kit	Qiagen (Hilden, Germany)
Go Tag G2 Flexi DNA Polymerase Kit	Promega (Mannheim, Germany)

High Sensitivity D1000 ScreenTape Kit	Agilent (Waldbronn, Germany)
High Sensitivity D5000 ScreenTape Kit	Agilent (Waldbronn, Germany)
High Sensitivity NGS Fragment Analysis Kit	Advanced Analytical Technologies (Heidelberg, Germany)
High Sensitivity RNA ScreenTape Kit	Agilent (Waldbronn, Germany)
iScript cDNA Synthesis Kit	Bio-Rad Laboratories (Hercules, California, USA)
KAPA Library Quantification Kit for Illumina platforms	KAPA Biosystems (Amsterdam, Netherlands)
peqGOLD Gel Extraction Kit	Peqlab Biotechnologie (Erlangen, Germany)
peqGOLD Plasmid Miniprep Kit I	Peqlab Biotechnologie (Erlangen, Germany)
Pierce BCA Protein Assay Kit	Thermo Fisher Scientific Inc. (Waltham, Massachusetts, USA)
PureYield Plasmid Maxiprep System	Promega (Mannheim, Germany)
Qubit ds DNA HS Assay Kit	Thermo Fisher Scientific Inc. (Waltham, Massachusetts, USA)
Rneasy Kit	Qiagen (Hilden, Germany)
SPRIselct Reagent Kit	Beckman Coulter (Krefeld, Germany)

2.9. Primers

All used primers are listed in this section.

Table 12: Primers for LIS1-mutation validation and regional identity control

Primer	Forward	Reverse
18s	attccttggaccggcgcaa	gccgcatcgccggtcgg
Emx1	agacgcaggtgaaggtgtgg	caggcaggcaggctctcc
FoxA2	ccaccaccaaccccacaaaatg	tgcaacaccgtctccccaaagt
FoxG1	ccctcccatttctgtacgttt	ctggcggctcttagagat
HoxA4	ttcagcaaaatgccctctct	taggccagctccacagttct
HoxB2	tttagccgttcgcttagagg	cggatagctggagacaggag
HoxB4	acacccgctaacaaatgagg	gcacgaaagatgagggagag
HoxB6	gaactgaggagcggactcac	ctgggatcagggagtcttca
LIS1 exon 1	gagccagttcagaagggg	gtggaggagacagaggggag

LIS1 exon 2	ggttaacatgattgggagtggg	agaagagacctcccaaagctg
LIS1 exon 3	ggttgctgtcacagagccat	agttcagtaccaagtagaccaca
LIS1 exon 4+5	attccagctgtcagcccttg	tgaacccagtcagcaactcc
LIS1 exon 6	agacagggagcggactatgt	gcaagagaatctgggctcgt
LIS1 exon 7	gctttgacatagtgaaacccca	tcgaagtgactgcaacacca
LIS1 exon 8	tgtctgttagcttattgttcctact	tcagaattgctggatgcagat
LIS1 exon 9	ctgagtccttcctgtgtagcat	agcatctccccctcaaacac
LIS1 exon 10	aacagaactgctgcgacagg	ggcgtacatacccaaggagg
Nkx2.1	ccggaggcagtgggaag	ccctccatgcccactttctt
Otx2	tgcaggggttcttctgtgat	agggtcagagcaattgacca
Pax5	aggatgccgctgatggagtac	tggaggagtgaatcagcttgg
TUBB3	gagcggatcagcgtctacta	ggttccaggtccaccagaa

2.10. Antibodies

All used antibodies are listed in this section.

Table 13: Molecular primary antibodies

Antibody	Host	Dilution	Manufacturer
Acetylated α-tubulin (AC-TUB)	Rabbit	1:500	Cell Signaling
AFP	Mouse	1:200	Hölzel
ARL13B	Mouse	1:50	DSHB
ß-ACTIN	Mouse	1:5000	Millipore
β-Catenin	Mouse	1:1000	Cell Signaling
ß-III-TUBULIN (TUBB3)	Mouse	1:2000	Sigma-Aldrich
TUBB 3	Rabbit	1:2000	Cell Signaling
FOXG 1	Rabbit	1:300	TebuBio
EMX 1	Rabbit	1:500	Sigma-Aldrich

LIS1	Mouse	1:500	Sigma-Aldrich
N-CADHERIN (N-CAD)	Mouse	1:500	BD
NANOG	Mouse	1:200	DSHB
PAX 6	Rabbit	1:500	DSHB
OCT 3/4	Rat	1:500	R&D Systems
OTX 2	Goat	1:500	R&D Systems
phospho-VIMENTIN (p-VIM)	mouse	1:500	Novus Biologicals
TPX 2	Rabbit	1:500	Novus Biologicals
SMA	Rabbit	1:400	Abcam
SSEA 3	Rabbit	1:500	Abcam
SOX 2	Rat	1:500	Santa Cruz
ZO-1	Rabbit	1:100	DSHB

Table 14: Molecular secondary antibodies

Antibody	**Host**	**Anti**	**Dilution**	**Manufacturer**
488	Goat	Rabbit	1:10,000	Invitrogen
488	Goat	Mouse	1:10,000	Invitrogen
555	Donkey	Rabbit	1:10,000	Life technologies
555	Goat	Guinea pig	1:10,000	Invitrogen
568	Goat	Mouse	1:10,000	Invitrogen
647	Donkey	Mouse	1:10,000	Invitrogen
DyLightTM 680 Conjugate	Goat	Mouse	1:1000	Cell Signaling
DyLightTM 680 Conjugate	Goat	Rabbit	1:1000	Cell Signaling
DyLightTM 800 Conjugate	Goat	Mouse	1:1000	Cell Signaling
DyLightTM 800 Conjugate	Goat	Rabbit	1:1000	Cell Signaling

2.11. Software

All used software is listed in this section.

Table 15: Computational software programs

Software	Manufacturer
ApE v2.0.47	M. Wayne Davis
AxioVision 40 4.5.0.0	Zeiss Microscopy GmbH (Oberkochen, Germany)
FIJI (ImageJ)	National Institutes of Health (Rockville, Maryland, USA)
Leica Application Suite 2.3.1	Leica Microsystems GmbH (Wetzlar, Germany)
Microsoft Excel 2010	Microsoft Corporation (Redmond, Washington, USA)
Microsoft PowerPoint 2010	Microsoft Corporation (Redmond, Washington, USA)
Microsoft Word 2010	Microsoft Corporation (Redmond, Washington, USA)

3. Methods

To approach the in section 1.6 listed aims multiple methods were used, which are in detail described in this section.

3.1. Cell culture

The cell culture was completed at the HITBR in Mannheim. Employing the standard of the art, iPS cells were cultured under feeder-free condition as colonies in Essential 8 (E8) medium or Pluripro (PP) medium (Cell guidance) at a constant temperature of 37ºC and 5% CO_2. The in this study incorporated gender matched control lines were received as iPS cell lines (see 2.1), the LIS1-patient fibroblasts and PBMCs were reprogrammed by non-integrative delivery of OCT 4, SOX 2, KLF 4, and c-MYC using CytoTune-iPS 2.1 Sendai Reprogramming Kit (Thermo Fisher) (for more information to the LIS1-patient material see table 1).

3.1.1. Culture and maintenance of fibroblasts

Fibroblast cells were cultured on galantine-coated cell culture plates in MEF medium with daily medium change at 37ºC and 5% CO_2. When cell cultures reached 70-100% confluency, cells were dissociated and passaged. Before adding the dissociation reagent 0,05% Trypsin-EDTA (Gibco) (500µl) for 10 min, the cells were washed with PBS. The single-cell suspension was transferred into a 15 ml tube containing 5 ml of DMEM (1X) + GlutaMAX™-I and centrifugated at 800 rpm for 5 min. After the aspiration of the supernatant, the cell pellet was resuspended in fresh MEF medium (2 ml per well of a 6-well plate) without Rock inhibitor. The splitting ratio can be up to 1:5 depending on the required cell density.

3.1.2. Culture of peripheral blood mononuclear cells

PBMCs consist mainly of lymphocytes and monocytes and do not significantly proliferate *in vitro* (especially monocytes). The addition of mitogens can help expanding those cells, but the reprogramming should be performed closely after blood isolation. For this study, the LIS1-patient PBMCs were immediately frozen after isolation and send from the pediatric neurology, Necker Enfants Malades university hospital in France. Directly after arrival, the PBMCs were thawed in 2 ml StemPro34 medium, counted and centrifugated for 10 min at 300g (swinging bucket rotor needed). In the following 500,000 cells/well were seeded in 1 ml PBMC medium in one well of a 24-well plate. For the next 3 days half of the media was changed daily. At day 4 reprogramming was performed (see 4.1.3).

3.1.3. Generation of induced pluripotent stem cell cultures

The discovery in 2007 of Shinya Yamanaka to convert human somatic cells back to stem cells revolutionized the research field and received 2012 the noble price. The molecular basis relays on the reintroduction of 4 transcription factors including human OCTAMER BINDING PROTEIN 3/4 (hOCT 3/4), human SEX DETERMINING REGION Y-BOX 2 (hSOX2), human KRÜPPEL-LIKE FACTOR 4 (hKLF 4) and cMYC. To date different protocols for the cellular reinstatement of pluripotency exist. In this study, the highly efficient Sendai-virus approach was used. It is important to mention that no matter what somatic cell type is subjected, it is important to use young passages to ensure good reprogramming efficiency and a normal karyotype. Fibroblasts and PBMCs were reprogrammed by non-integrative delivery of OCT 4, SOX 2, KLF 4 and cMYC using the CST™- iPS 2.1 Sendai reprogramming kit (Thermo Fisher).

3.1.3.1. Sendai virus-based reprogramming of fibroblasts

The reprogramming of the fibroblasts was performed according to the manufacture's description (CTS™ CytoTune™-iPS 2.1 Sendai Reprogramming Kit User Guide). All fibroblast lines had a young culture passage (P) (P<10) and were tested negative for mycoplasmas. 1 day before transduction 2 wells with each 40% confluency were seeded on 1 well of a 6-well plate. 1 of the 2 wells was used to count the cells to calculate the needed virus amounts, which are determined by the MOI (CIU/cell) times the number of PBMCs divided by the titer of the virus (CIU/ml) times 0,010. The viruses were thawed at 37°C for 10 to 20 seconds (sec), placed at room temperature (RT) for complete thawing and then immediately placed on ice. In the next step, the calculated virus amounts of all 3 Sendai viruses were supplemented to 1 ml prewarmed MEF medium and added into the fibroblast well. It followed an incubation at 37°C overnight. The next day the medium was changed to MEF medium without virus. It followed further culturing for 6 more days with medium change every other day. At day 7 the fibroblasts were spitted in a 1:3 ratio. As soon as the first iPS cells clonal colonies appeared the medium was changed to hES medium (approximately 3 weeks later). When the iPS cell colonies were clearly visible by eye without using a microscope, they were clonal expanded (see 4.1.3.3).

3.1.3.2. Sendai virus-based reprogramming of PBMCs

The reprogramming of the PBMCs was performed according to the manufacture's description (CTS™ CytoTune™-iPS 2.1 Sendai Reprogramming Kit User Guide). 4 days after thawing the suspension PBMCs were counted to calculate the needed volumes of the viruses to reach the

target MOI. Virus amount calculation and virus thawing was performed as described in 3.1.3.1. In the next step, the calculated virus amounts of all 3 Sendai viruses were added to 1 ml PBMC medium. For each cell line 500,000 cells were pipetted into an 1,5 ml reaction tube and the virus containing PBMC medium was added. It followed a centrifugation step at 1000 xg for 30 min at RT. Afterwards an additional 1 ml of PBMC medium was added and the whole mixture was plated in 1 well of a 12-well plate for incubation at 37°C overnight. The next day the cell suspension was transferred into a 15 ml tube and centrifugated at 200 xg for 10 min to aspire the supernatant and resuspend in 0,5 ml of PBMC medium per well of a 24-well plate. For the next 2 days no medium change was performed. At day 3 after transduction the cells were centrifugated at 200 xg for 10 min to aspire the supernatant and resuspended in Stempro34 medium. 10,000, 50,000 and the rest of the cells were each plated on 1 well of a GT-coated 6-well plate. The next day and on day 6 half of the medium was changed. On day 7 half of the medium was replaced by hES medium and on day 8 the medium was completely changed to hES medium. From this timepoint the hES media was changed daily until iPS cells clones were ready to be clonal expanded (approximately 1 week later).

3.1.3.3. Clonal expansion of iPS cell lines

To generate monoclonal iPS cell lines, appearing clones were separated and expanded. Only cell dense colonies with sharp borders were selected and transferred into 1 well of a 24-well plate using a cut 100 µl pipette tip to scratch the clonal colonies from the GT-coated wells. The first passage was plated on 1 well of a 12-well plate, the second passage on 1 well of a 6-well plate and the third passage was placed on 2 wells of a 6-well plate (see 3.1.5 for passaging procedure). Next, 1 well was further passaged and the second well was cryo-conserved. At least 10 cryo-vials for each generated iPS cell line were generated. All iPS cell lines were quality controlled.

3.1.4. Quality control of iPS cell lines

Following iPS cell clonal expansion, 2 clones for each cell line were characterized using tripotente differentiation, immunochemical staining for pluripotency markers and whole-genome single nucleotide polymorphism (snp) analysis for chromosomal integrity control. In addition, the LIS1 mutations were validated via polymerase chain reaction (PCR) and sanger sequencing.

3.1.4.1. Whole-genome single nucleotide polymorphism genotyping

The snp analysis was performed at the Institute of Human Genetics at the University in Bonn. Genomic DNA was prepared using the DNeasy Blood & Tissue Kit (Qiagen) and 50 ng/ml was used for whole-genome amplification. In the following, the amplified DNA was fragmented and hybridized to sequence specific oligomers bound to beads on an Illumina Human610-Quad chip or a HumanCytoSNP-12 chip. The Data was analyzed by Josef Frank from the Genetic Epidemiology Department headed by Prof. Rietschel using Illumina Bead Studio.

3.1.4.2. Germ layer differentiation

To test the pluripotent capacity of the generated iPS cell lines, cells were tested for the ability to spontaneously differentiate into the 3 germ layers including endoderm, mesoderm and ectoderm. To achieve a 3D-like dense cell population, iPS cells were dissociated into single-cells using TrypLE Express (Gibco) and plated in a pluronic-coated U-bottom 96-well plate (6000 cells/well) in PP/E8 medium supplemented with 50 µM Rock inhibitor to induce embryoid body (EB) formation. After 2 days EBs were plated onto GelTrex (GT)-coated dishes in mouse embryonic fibroblast (MEF) medium and cultured for 4 weeks. In the following, differentiated cell cultures were fixed with 4 % PFA and then subjected to immunocytochemical analysis using the antibodies against α-1-fetoprotein (AFP) for endodermal cells, smooth muscle actin (SMA) for mesodermal lineage and bIII-tubulin (TUBB3) for ectodermal cells.

3.1.4.3. Validation of LIS1 genotype

The LIS1-patient iPS cell cohort is characterized by diverse LIS1 mutations in the different patient lines. To confirm the mutations 1 well of a 6-well plate of each LIS1-patient iPS cell line was harvested and used for DNA isolation using the DNeasy Blood & Tissue Kit (Qiagen). To amplify the mutation containing DNA regions specific primers for each iPS cell line were designed (see table 12) and PCR for target sequence amplification was performed (see 4.3.3). The PCR fragments were separated using DNA electrophoresis and extracted from the agarose gel using the Gel Extraction Kit (peqGOLD). The in water diluted PCR fragments were subjected to sanger sequencing by Microsynth-Seqlab.

3.1.5. Maintenance of iPS cell cultures

The iPS cell cultures can be grown in colony or monolayer formation determinant by the feeding medium used. For this project, the iPS cells were mainly cultured as monolayer cultures using the monolayer PP medium, which had a beneficial effect on the LIS1-patient cell vitality

especially when generating 3D cell cultures. One disadvantage of monolayer cultures is the need for daily medium change and a higher passaging frequency when comparing to colony cultures, which can lead to a faster accumulation of chromosomal abnormalities. Due to this, it is important to perform snp analysis on regular basis and to thaw young, snp analyzed cells. Colony culturing was induced by the usage of E8 medium and was implemented for the new reprogrammed iPS cell lines for backup generation and quality control. To transform the colony cultures to monolayer growth, 2 cell-dense wells of a 6-well plate were dissociated using TrpLE (Gibco) for 10 min, then transferred to a 15 ml tube and centrifugated at 800 xg for 4 min. The cell pellet was resuspended in 2 ml of half PP, half E8 (PP/E8) medium (1:1) supplemented with 5 μM Rock inhibitor (Cell guidance systems) and plated into 1 well of a 6-well plate. 50% of PP medium was sufficient to induce monolayer growth. The next day the medium was changed to PP medium.

3.1.5.1. Maintenance of iPS cell colony cultures

The iPS cell colonies were maintained on GT-coated cell culture plates in E8 medium with daily medium change. Colonies were passaged when reaching 70 % – 80 % confluency. First, cells were washed with 0,5 mM EDTA (Gibco) (1:1000 dilution in PBS) and then incubated with 0,5 mM EDTA (Gibco) for 4 min at RT. After EDTA aspiration cultures were gently dissociated into smaller fragments by gently washing them of the well with a 1000 μl pipette containing E8 medium supplemented with 5 μM Rock inhibitor (Cell guidance systems). The passaging ratio can vary between 1:4 to 1:6 depending on the cell line used. All human iPS cell lines were regularly checked and confirmed negative for mycoplasma.

3.1.5.2. Maintenance of iPS cell monolayer cultures

The iPS cell monolayers were maintained on GT-coated cell culture plates in PP medium with daily medium change. iPS cells were dissociated to single-cells by TrypLE Express (Gibco) treatment for 10 min when cultures reached 100% confluency and split in a 1:2 – 1:4 ratio depending on the proliferative capacity of the cell lines used. Following dissociation to single-cells, suspension was diluted in 5 ml DMEM (1X) + GlutaMAX™-I (Gibco) and transferred to a 15 ml tube. Following centrifugation at 800 xg for 4 min and supernatant aspiration, the cell pellet was diluted in PP medium supplemented with 5 μM Rock inhibitor Y-27632 (Cell guidance systems) to promote single-cell survival. All human iPS cell lines were regularly checked and confirmed negative for mycoplasma.

3.1.6. Generation of WNT-GFP reporter lines

For examining the level of WNT-signaling activation in control- (control 2.1, control 3.1) and LIS1-patient- (mild P1.1, mild P2.2, moderate P3.1, severe P5.1 and severe P7.1) derived organoids, iPS cells were transduced with a lentivirus (see 4.3.1 for virus production) expressing GFP under activation of WNT-signaling (lentiviral-top-dGFP reporter, Addgene plasmid #14715, Reya et al., 2003). Puromycin (1 µg/ml, Sigma-Aldrich) selection was initiated 48h following transduction. The iPS cell WNT-GFP reporter lines were used for cortical organoid generation (3.1.9).

3.1.7. Cryo-conservation of cells

Fibroblasts and iPS cells were stored at -150°C or in liquid nitrogen for cryo-conservation. When iPS cell cultures reached 100% confluency, the cells of at least 2 wells of a 6-well plate were dissociated to single-cells by TrypLE Express (Gibco) treatment for 10 min and diluted in 5 ml DMEM (1X) + GlutaMAX™-I (Gibco). Following centrifugation at 800 xg for 4 min and supernatant aspiration, the cell pellet (at least 1 million cells) was diluted in 1 ml of pause medium supplemented with 10 µM Rock inhibitor Y-27632 and then immediately transferred to a freezing container containing isopropanol at -80 °C. After 24 hours (h) cells were transferred to minus 150°C or liquid nitrogen for long term storage.

3.1.8. Generation of highly homogenous 2D cortical progenitor cultures

Within the project highly homogenous 2D cortical progenitors were used for western blot analysis. Consequently, iPS cells were cultured in PP medium as monolayer in 1 well of a 6-well plate until the cell culture reached 95% confluency. To initiate neural cortical induction the culture medium was changed to neural induction medium (see table 6). The medium composition was adopted from Chamber et al. 2009 and is based on the dual inhibition of SMAD signaling. The fate inducing small molecules were A83, a TGFβ signaling inhibitor, LDN, a BMP signaling inhibitor, and in addition XAV for WNT-signaling inhibition to avoid posterization to hindbrain fates. The very dense iPS cell cultures were kept on the same well for 10 days with daily medium change. After 10 days cells were harvested for molecular analysis or expanded by passaging in neural induction medium. The withdrawal of the small molecules after the passaging leads to the differentiation of the cortical progenitors to cortical neurons.

3.1.9. Generation of cerebral forebrain-type organoids

Within Dr. Julia Ladewigs research group, me and my colleagues developed a protocol for highly homogenous cortical forebrain-type organoids (outlined in Figure 7, Krefft et al. 2018; Iefremova et al. 2017). Due to the rapid progress within the organoid field, the published protocol was constantly further advanced and brought up to standard of the art technology. It included EB formation, neural induction, GT embedding and organoid maturation.

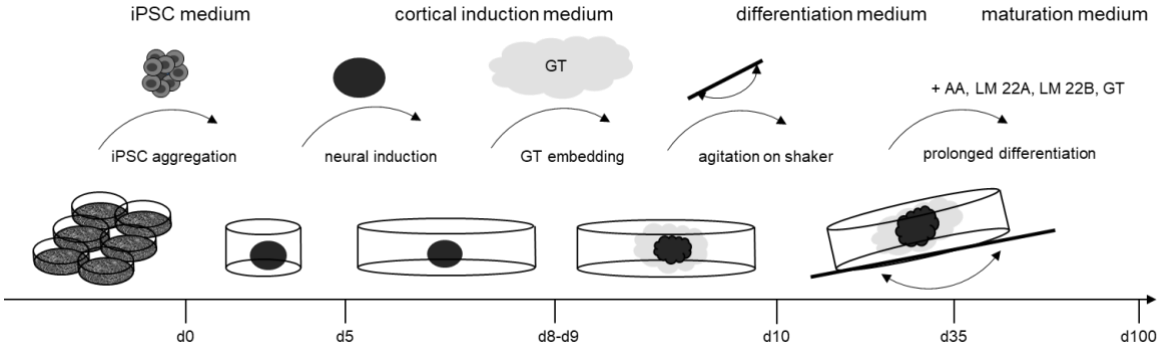

Figure 6: Protocol outline for cortical forebrain-type organoid generation. The organoid generation is initiated by embryoid body formation, which are restricted to the ectodermal fate by neural induction through dual SMAD and WNT inhibition. The outgrowth of neuroepithelial ventricular structures is supported by extracellular matrix proteins and mechanical scaffold provided by Geltrex (GT) embedding. To ensure good nutrient delivery into the tissue, organoids are cultured on a shaker. For further maturation growth factors including Ascorbic acid (AA), LM 22 A, LM 22 B and GT are added into the differentiation medium (maturation medium) from day 35 on.

3.1.9.1. Embryoid body formation and neural induction

Organoid generation is initiated by EB formation. The most important and crucial step during EB generation is the number of cells used. The optimal cell number is different for every cell line and needs to be tested. Most of the time less cells led to more compact EBs with clear and sharper borders, which led to highly homogenous organoids. Before starting EB generation, ultralow cluster 96-well plate ultra-low attachment round bottom with lid (Costar by Sigma-Aldrich) were covered and incubated for 10-20 min at 37°C with pluronic solution (50 mg/ml, Sigma-Aldrich). To generate EBs, iPS cells were dissociated into single-cells using TrypLE (Gibco) for 10 min. Single cell suspension was transferred into a 15 ml tube containing DMEM (1X) + GlutaMAX™-I (Gibco) and counted using the automated cell counter, LUNA (Logos Biosystem). After centrifugation at 800 xg for 4 min cells were diluted in PP medium supplemented with 50 µM Rock inhibitor. In the next step 6000 cells per EB for control iPS

cell lines and 8000 cells per EB for LIS1-patient lines were seeded into 1 well of a pluronic-coated 96-well plate ultra-low attachment round bottom with lid (Costar by Sigma-Aldrich). EBs were fed every other day for 4 days. On day 5 medium was changed to neural induction medium containing the dual SMAD inhibitors A83 and LDN as well as the WNT inhibitor XAV. For the next 5 days medium was changed every other day until the EBs developed translucent tissue at the edges. To promote the expansion of the neuroepithelium into cortical VZ structures, the EBs (now called organoids) are embedded into GT between day 8 and day 10, depending on the iPS cell line used.

3.1.9.2. Organoid embedding and differentiation

The organoid GT embedding was done in 2 different ways. One technique is called the parafilm droplet embedding, which is more time consuming than the second embedding technique but ensures that every organoid is separately embedded in a GT droplet. This method should be preferred when single organoids are needed afterwards. The second organoid embedding method is named “cookie embedding”. This technique is faster and needs less GT because multiple organoids are embedded in the same GT droplet. The disadvantage is that organoid fusion happens more frequently. For both embedding procedures, GT was thawed on ice 2-3 h before starting organoid GT embedding.

For the droplet embedding parafilm was cut into 4 cm x 4 cm pieces and placed over an empty tip tray for 100 µl tips to press dimples into the parafilm sheet, which was then sterilized with 70% ethanol and irradiated with UV light (power: 15 watts, wavelength: 435 nm) under the closed sterile bench for 30 min. In the next step, each EB were transferred into 1 dimple using a cut 100 µl tip. The medium surrounding the EB was gently aspirated using an uncut 100 µl pipette tip. Then 20 µl of undiluted GT was added to each EB, which was then positioned in the middle of the drop using an uncut 100 µl pipette tip. The plastic parafilm sheet was carefully transferred using sterile forceps into a 10 cm dish, which was placed in the incubator for 20 min to allow GT solidification. Afterwards, the embedded organoids were transferred into a pluronic-covered low-attachment 6 cm dish containing 6 ml of neural induction medium. To do so the parafilm was gently pressed upside down onto the dish using sterile forceps, so that the GT was gently squeezed into the tilted 6 cm dish and then slowly lifted, so that the drops gently slide of the parafilm into the medium. Each 6 cm dish had a maximum of 16 EBs. The 6 cm dish was then placed in the incubator at 37ºC.

For the cookie embedding the EBs of one batch (maximum 16) were all together transferred into a 1,5 ml Eppendorf tube. The medium was carefully aspired using an uncut 100 µl pipette

tip. In the following all EBs were diluted in 200 µl GT using a cut pipette tip and immediately transferred into a pluronic-covered low-attachment 6 cm dish, which was placed in the incubator for 25 min to allow GT solidification. In the following 6 ml of neural induction medium is added on top and then placed in the incubator at 37°C.

At day 10 medium was changed to organoid differentiation medium and the dish was placed on a shaker with a tilting angle of 5º and 14 rpm for further agitation. For the next 15 days medium was changed every third day until the desired time point was reached. For this study organoids were mostly fixed at day d20 for immunochemical analysis and quantitative assessment. For single-cell RNA analysis organoids were cultured for 58±2 days. On day 35 the medium was changed to maturation medium containing Ascorbic acid (AA), LM 22 A, LM 22 B and GT to promote better tissue complexity.

3.2. Histology and immunocytochemistry

A major part of this project was the immunocytochemical analysis of organoid cryo-sections and the quantitative assessment of cytoarchitectural parameters. The methodology from fixation, cryo-embedding, cryo-sectioning, tissue clearing and immunocytochemical- as well as hematoxylin-eosin staining are described in this section.

3.2.1. PFA fixation

For the preservation of cells and organoids after cultivation 4 % PFA fixation was used to reserve cell structures and crosslink proteins. Due to the toxicity of PFA the fixation was carried out under a chemical fume hood. First, organoids were transferred into a 24-well plate with a cut 1000 ul pipette and twice washed with PBS. iPS cells were directly fixed in the 3,5 cm culture dish and twice washed with PBS. After PBS aspiration, 4 % PFA (table 8) was added followed by a 10 min incubation at RT. Afterwards, 4 % PFA was carefully aspirated and organoids as well as iPS cells were washed 3 times with PBS. For tissue dehydration organoids were placed in 30 % sucrose solution and stored at 4 ºC overnight. Organoids can be stored up to 7 days until cryo-cutting or clearing. iPS cells can be stored for up to 4 weeks at 4 °C until further processing.

3.2.2. Organoid cryo-embedding and cryo-sectioning

To perform cryo-sectioning organoids were embedded in sucrose/galantine embedding solution (see table 8), which was stored at -20 °C. Before starting, the solution was liquified by warming to 75 ºC. The dehydrated organoids were transferred to 2 ml Eppendorf tubes. After aspirating

the 30 % sucrose solution, 1 ml embedding medium was added, and the tubes were placed at a heating plate (60 ºC). In the next step, embedding molds were covered with a layer of embedding solution and placed on ice to solidify. 1 to 4 organoids from the tube at the heating plate were placed on top and additional embedding medium was added to cover the organoids completely. Afterwards, the mold was hold in 100% ethanol/dry ice freezing bath (-30 to -50 ºC) for at least 1 min to shock-freeze the tissues. The embedded organoids were stored at -80 ºC for at least 30 min before cryo-cutting.

The cryo-sectioning was performed at the cryostat. Sections were made with 20 µm thickness and sequential collected on microscope slides, so that every slide had sections from all organoid regions. The sections dried at RT for at least 1 h before being stored at -80 ºC or directly be used for immunocytochemical staining.

3.2.3. Organoid clearing

For whole tissue mounting organoids were fixed in 4 % PFA for 2 h at RT. Subsequently, organoids were washed 3 times with PBS at RT for 2 h. Optical clearing was performed according to Susaki et al. (Susaki et al. 2014) by immersion of samples in ScaleCUBIC-1 solution for 48 h at 37 °C and subsequent washing in PBS 3 times for 2 h at RT. Following optical clearing samples were immersed in clearing blocking solution for 24 h at 37°, followed by primary antibody incubation for 48 h at 37 °C, and subsequent washing in blocking solution 3 times for 2 h at RT. Secondary antibody incubation was done for 48 h at 37°C, followed by washing samples 3 times for 4 h each in PBS at RT. Refractive index matching was performed by immersion of samples in an aqueous solution of glycerol (RI=1.457) for 48 h at RT. All incubations were carried out under protection of light and constant movement. Samples were mounted in U-shaped 2.5 mm glass capillaries by embedding in 0.1 % low melting agarose in ddH_2O. For light sheet microscopy, glass capillaries were transferred into 35 mm glass bottom dishes, immobilized by agarose embedding and immersed in RI-matched glycerol solution. For temperature adjustment, samples were kept in the microscopy room for at least 24 h prior to image acquisition. Image acquisition was done using a Leica Microsystems TCS SP8 DLS, equipped with LAS X software, L 1.6x/0.05 DLS illumination objective, HC APO L 10x/0.30 W DLS detection objective and 7.8 mm Glycerol DLS TwinFlect mirrors. Image stacks were acquired with a step size of 3.7 µm and fused with LAS X. Organoid clearing and whole tissue imaging was performed with the help of Elina Nürnberg.

3.2.4. Immunocytochemical staining

To analyze the cytoarchitecture of cortical organoids and visualize specific proteins immunocytochemical staining`s were performed on 2D cells and 3D organoid sections. A liquid barrier pen was used to circle the sample material so that smaller amounts of antibody solutions were needed to cover the area of interest. After washing with PBS, an incubation with blocking solution (0,1 % Triton and 10% FCS) followed for 1 h at RT. For nuclear proteins the triton concentration was increased to 0,5% for a better nucleus permeabilization. Primary antibodies were diluted according to the manufacturer's instructions (see table 13) and incubated over night at 4 °C. The next day samples were washed 3 times with PBS. The secondary antibodies were diluted according to the manufacturer's instructions (see table 14) and incubated for 1 h at RT with subsequent washing. It followed 3 times washing with PBS and a 5 min incubation with DAPI (1X) staining solution (see table 14) with subsequent washing. The slides were then covered with mounting solution (see table 8) and enclosed with a cover slip. Immunocytochemically stained sections were stored at 4 °C and imaged using the Inverted Leica DMIL LED Microscope with Thunder imaging software (Leica), the confocal microscope TCS SP5II (Leica) or the Fluorescence Microscope Celldiscoverer 7 (Zeiss).

3.2.5. Hematoxylin and eosin staining

Hematoxylin-eosin staining was used to visualize cell morphology within the organoid cortical VZ structures to analyze cellular organization. Hematoxylin has a deep blue-purple color and stains nucleic acids while Eosin is pink and stains proteins nonspecifically resulting in blue nuclei and pinkish cytoplasm and extracellular matrix. In the first step organoid sections was placed in ddH_2O for 10 sec, stained with hematoxylin solution (Carl Roth) for 10 min, shortly put in ddH_2O and then rinsed under running tap water for 10 min. In the next step the slide was twice hold in 70% ethanol for 10 sec and then again rinsed in tap water for 10 min. Next, the slide was stained with 0,5% eosin solution (Carl Roth) for 5 min and afterwards shortly put in ddH_2O. For dehydration and clearing, it followed an alcohol series incubation starting with 70 %, 80 % and 90 % ethanol solution for 10 sec and then twice 100% ethanol incubation for 5 min each. Afterwards the slide was dried and mounted with Mowiol. Slides were stored at 4 °C and imaged using the inverted Leica DMIL LED Microscope with Thunder imaging software (Leica).

3.3. Molecular biology

In addition to the histological investigations, molecular biological analysis played an important part within this project to decipher the molecular basis of observed LIS1-associated phenotypes in 3D organoids and to understand the variable lissencephalic severities.

3.3.1. Lentivirus production

For the generation of WNT-GFP reporter iPS cell lines lentivirus was produced in HEK293T cells, which were received from Bettina Bohl. Prior to the virus transfection the medium was changed to MEF medium supplemented with chloroquine (25 µM; 0,129g in 10 ml H_20) to prevent autophagy and prevent DNA degradation. In the next step 7,9 µg of psPAX2 packing vector (coding for viral envelop proteins), 3,5 µg pMD2.G packing vector and 10 µg of the transfer vector pRRL.sin-18.ppt (Addgene plasmid #14715) were mixed in 450 µl H_2O. Additionally, 50 µl 2M CaCl2 solution was added to the vector mix. Next, 500 µl 2x HBS in 15 ml tube was prepared and fizzed by using a 5 ml pipette to blow air into the solution. During this fizzing process the DNA solution was added dropwise on the outside of the 5 ml plastic pipette into the HBS frizzed solution. It followed 30 min incubation at RT and then dropwise adding to the HEK293T cells. After 8 h fresh MEF medium was added. 2 days after the transduction the medium was collected and fresh medium added, which was again collected on day 3 after transduction. The conditioned medium from day 2 and 3 were pooled and centrifugated at 12,000 xg for 5 min. The supernatant (17 ml) was filtered through a 0,45 µm filter. It followed the addition of 4,2 ml 50% PEG-600 solution, 1,8 ml 4M NaCl and 1,9 ml PBS and mixing by inverting. Afterwards the solution was incubated for 1,5 h at 4 °C and inverted every 30 min during this incubation time. After centrifugation for 5000 xg for 20 min at 4 °C supernatant was discarded, and virus pellet was dissolved in 100 µl HBS/1 % BSA and stored at -80 °C. Virus production was performed together with Bettina Bohl.

3.3.2. DNA isolation

Genomic DNA was isolated from 2D iPS cells for LIS1 mutation validation using the Dneasy blood and tissue kit (Qiagen) to isolate high-quality DNA with great yields. The kit provides buffers, proteinase, collection tube and columns for isolation and provides a simple protocol with lysis and precipitation steps.

3.3.3. RNA isolation

To analyze gene expression via PCR, RNA was isolated using peqGOLD TriFast (Peqlab). 3 to 4 organoids were transferred into a 2 ml Eppendorf tube and washed twice with PBS before adding 500 µl peqGOLD TriFast. Suspensions were resuspension until cell clumps were dissolved. 2D cells were washed twice with PBS and then scratched of the well using a cell scrapper. The cells were suspended in PBS and transferred into a 2 ml Eppendorf tube for centrifugation at 800 xg for 4 min to pellet the cells. PBS was discarded and cells were resuspended in 1 ml of peqGOLD TriFast until no cell clumps were observable. The lysates were incubated for 10 min at RT and then 200 µl of chloroform was added. In the following the Eppendorf tubes were inverted for 15 sec and then incubated for 10 min at RT. In the next step lysates were centrifuged at 12,000 xg for 5 min at 4 °C. The resulting pink phase containing the proteins was discarded and the clear phase containing the nucleic acid was transferred into a new Eppendorf tube and supplemented with 500 µl isopropanol (1:1 ratio). The RNA precipitation was done for 2-3 h on ice or overnight at -20 °C. After incubation the sample was centrifuged 15 min at 12,000 xg at 4 °C. Supernatant was discarded and the pellet was washed twice with 1 ml of 75 % ethanol in DEPC water followed by a centrifugation step of 12,000 xg for 10 min at 4 °C. In the last washing step, the 75% ethanol was thoroughly discarded, and the RNA pellet was left to air dry at RT for about 30 min. Once the pellet was dry, it was resolved in 20 µl of DEPC-H_2O by 37 °C and shaking at 400 rpm in the heating block for 15 min. It followed DNA treatment to prevent DNA contamination using the DNase I Amplification Grade kit. For this the samples were supplemented with 2,5 µl of DNase and 2,5 µl reaction buffer and incubated 15 min at RT. To stop the reaction 2,5 µl of STOP solution were added and another incubation for 10 min at 70 °C was performed. Concentration (ng/ µl) was measured with the nanodrop and RNA was stored at -80 °C.

3.3.4. Reverse transcription

To qualitatively study gene expression, the isolated RNA needed to be reversed transcript back to DNA to perform PCR or qPCR. Consequently, the iScript cDNA synthesis kit from Bio-Rad systems was used. Following the manufactures instruction 1 µg RNA was added to 4 µl 5X iScript reaction mix and supplemented with 1 µl iScript reverse transcriptase enzyme. The reaction mix was added to 20 µl with nuclease free H_2O. The reverse transcription was done using the MJ Research PTC-200 Thermal

Cycler (Biozym Diagnostics) using the steps shown in table 16. Afterwards cDNA concentration (ng/µl) was measured using the nanodrop and diluted in H_2O to 250 ng/µl. The samples were stored at -20 °C.

Table 16: Steps and condition of the iScript program

Cycle Step	Temperature	Time
Priming	25 °C	10 minutes
Reverse Transcription	46 °C	20 minutes
Inactivation	95 °C	1 minute

3.3.5. PCR and DNA electrophoresis

The PCR was used to amplify specific gen regions of interest. For the validation of mutated genome sequences genomic DNA (gDNA) was isolated from the cells (see 3.3.2). To analyze the presence and quantity of gene expression for specific marker genes RNA was isolated, reverse transcription (RT) performed and cDNA generated (see 3.3.3). 1 PCR reaction mix contained 2,5 µl of tag polymerase buffer comprising 10mM MgCl2, 5 µl of dNTPs (100mM, 25mM each dNTP, see table 8), 1 µl primer (see table 12), 1 µl DNA (250 ng/µl) and 0,25 µl tag polymerase added to 25 µl total volume with nuclease free H_2O. The reaction was done using the MJ Research PTC-200 Thermal Cycler (Biozym Diagnostics) using the steps shown in table 17.

Table 17: Reaction conditions RT PCR

Cycle Step	Temperature	Time	Cycles
Initial denaturation	95 °C	30 seconds	1
Denaturation	95 °C	30 seconds	35-45
Annealing	55-65 °C	1 minute	35-45
Extension	72 °C	30 seconds	35-45

To separate the target DNA amplicons from other PCR components, electrophoresis was performed using a 1% Agarose gel containing 20,000X pegGreen DNA and RNA binding dye (Peqlab). The PCR products were mixed with 6X loading dye and pipette into the gel. To determine the DNA fragment size a 100 bp DNA ladder were loaded, and the gel was placed inside the electrophoresis chamber with 1X TAE buffer. To separate the fragments 100 V and 400 mA were applied for 50 min. Afterwards PCR bands were revealed using the UV light lamp and if necessary isolated from the agarose gel using the Gel Extraction Kit (peqGOLD).

3.3.6. Quantitative protein assessment

For the detection of LIS1 protein levels western blot analyzes were performed using the blotting system from Bio-Rad.

3.3.6.1. Sample collection and lysis

2D progenitors or iPS cells were washed with ice-cold PBS, scraped off into 1 ml PBS using a cell scrapper and collected via centrifugation at 800 xg for 4 min. The cell pellets were lysed in lysis buffer (50 mM Tris-HCl pH 7.4, 50 mM NaCl, 1 mM EDTA, 1% Triton X-100) containing pierce protease inhibitor mini tablet (1 tablet per 10 ml, Thermo Fisher) and pierce phosphatase inhibitor mini tablet (1 tablet per 10 ml, Thermo Fisher) for 1 h on ice. Subsequently, cell debris was pelleted by centrifugation at 12,000 xg for 10 min. The supernatant containing the proteins were transferred into a new 1,5 ml Eppendorf tube and used for protein concentration measurements using the Bicinchoninic acid (BCA) protein assay kit (ThermoFischer).

3.3.6.2. BCA protein assay

The BCA protein assay is a widely used method for protein concentration determination, which uses the reduction of copper (II) sulfate (Cu^{2+}) to CU^{1+} by protein in an alkaline medium. The pierce BCA protein assay kit (Thermo Fisher) provides 2 components necessary to perform this reduction reaction and absorption measurements containing BCA, sodium carbonate, sodium bicarbonate, sodium tartrate and CU^{2+}. The protein amount is proportional to the amount of reduced CU^{2+} and 2 molecules of BCA form with each CU^{1+} ion a purple colored complex that intensively absorbs light at a wavelength of 562nm. Concluded, can the protein concentration be measured by the absorption spectra. The exact steps were performed according to the manufacturer's instructions (Thermo Fisher).

3.3.6.3. SDS-PAGE

To separate the proteins according to their mass sodium dodecyl sulfate–polyacrylamide gel electrophoresis (SDS-PAGE) was performed. SDS acts as a surfactant covering the proteins intrinsic charge properties. For immunoblotting, 30-50 µg of protein were boiled in 6x SDS sample buffer for 5 min at 95 °C. Lysates were put on 12 % SDS-PAGE gels (see table 8 for information about the buffers used) and separated using the blotting system from Bio-Rad with the PowerPac HC power supply for SDS PAGE (40 V the first 10 min, then 120 V until loading dye runs out the gel). To transfer proteins from the gel on a membrane semi-dry western blotting was performed.

3.3.6.4. Semi-Dry western blotting and band detection

The semi-dry western blot was done using the trans-blot turbo transfer system (Bio-Rad) for 45 min at 20 V and 10 A. In between the electrodes the "blotting sandwich" was prepared from down to top as follows: 6 layers of wypall-hydroknit wipes (Kimberly-Clark), 0,2 µl nitrocellulose membrane (GE Healthacare Life Science), SDS-PAGE gel and again 6 layers of wypall-hydroknit wipes. All components were socked in blotting buffer (see table 8) for 10 sec before assembly. Following blotting the membrane was put into a 50 ml tube containing 2,5 ml of 5 % purified BSA (Sigma-Aldrich) in PBS for blocking on a rolling mixer (sustainable lab instruments) for 1 h. In the next step the membrane was incubated over night at 4 °C with the primary antibody diluted according to the manufacturer's instructions (see table 13) in TBS (see table 8). The next day the membrane was washed 2 times with TBST for 10 min and 1 time with TBS for 10 min. Then the secondary antibody (DyLightTM Conjugate antibody) was diluted according to the manufacturer's instructions (see table 14) in TBS. After subsequent washing the protein band detection was done using the odyssey imaging system from Li-cor.

3.4. Quantification and statistics

To have persuasive data and make conclusive assumptions it is necessary to put observed phenotypes in numbers and deliver trustworthy statistics. The organoid technology is a very young research field and reliable quantitative assessment protocols did not exist when I started my PhD project in 2017. Due to this, I developed complex quantification protocols for different organoid VZ structure parameters to precisely assess cortical development in a dish (published in Iefremova et al. 2017, see results 4.1).

3.4.1. Plane of cell division analysis

The orientation of the plane of cell division plays a crucial role during corticogenesis. Consequently, the mitotic planes were analyzed by marking dividing cells immunocytochemically for p-VIMENTIN (p-VIM) and the mitotic spindle with TPX2 in 20 µm thick organoid sections. The orientation of the mitotic spindle of aRG cells were investigated in at least 5 different VZ structures per organoid in relation to the prospective VZ surface. This quantification method was established by Vira Iefremova and George Manikakis.

3.4.2. Statistical analysis

Quantitative data was generated in at least triplicates and tested for gaussian distribution using the Kolmogorov-Smirnov-Test. The Levene-test was applied to test for homogeneity of

variances. If the data was characterized by gaussian distribution one-way-Anova was used to determine whether a significant difference exists between groups and can be termed significant (*$p < 0.05$, **$p < 0.01$, ***$p < 0.001$). If the Kolmogorov-Smirnov-Test or the Levene-Test were significant, the assumption of homogeneity of variances and gaussian distribution was hurt and the significance was determined using Kruskal-Wallis-Test and Post-Hoc-Test (see appendix statistics). Means and standard deviation (s.d.) were computed. All results presented as bar graphs show mean +/- s.d..

4. Results

To decipher the consequences of the diverse LIS1 mutations on human corticogenesis and test the sensitivity of our 3D organoid *in vitro* cell culture system to mirror disease severities a LIS1-lissencephaly patient iPS cell cohort was established, a forebrain-type organoid protocol was developed and quantitative assessment protocols were designed to sensitively detect fine differences. Furthermore, molecular explorations were conducted to analyze severity-specific pathology and specific substances were identified to rescue observed phenotypic alterations. Moreover, the consequences of the particular mutations on LIS1 folding and stability were elucidated. To decipher pathological gene expression alterations at later developmental stages transcriptional profiling was performed. The results are presented within this section.

4.1. Generation of a LIS1-lissencephaly patient iPS cell cohort covering the complete lissencephalic severity spectrum

The LIS1-patient iPS cell cohort was established by Sendai virus-based reprogramming of fibroblasts and PBMCs (see 3.1). The cohort comprised female and male patients between the age of 3 and 18 years with different severe brain alterations ranging from Dobyns grade 5 to 1 (Dobyns W.B., 1999) (see 2.1 and table 1). To quality control the generated iPS cell lines pluripotency stainings, snp-analysis and mutational validation by sequencing were performed.

4.1.1. Generated iPS cell lines express pluripotency transcription factors

In 2007 Takashi et al. (Takahashi et al. 2007) opened a completely new perspective for patient- and disease specific research by introducing the induction of pluripotent cells from adult human fibroblasts. The ability to manipulate and reverse cell fate to generate iPS cells relies on the defined mix of 4 transcription factors including OCT 3/4, SOX 2, KLF 4 and CMYC. Following the introduction of those 4 factors into the LIS1-patient PBMCs and Fibroblasts, the generated iPS cell lines were quality controlled for the expression of pluripotency factors by immunocytochemical analysis including SOX 2 and OCT 3/4, which are important transcription factors for the promotion of self-renewal of undifferentiated stem cells, NANOG (HOMEOBOX PROTEIN) a transcription factor important for the suppression of the expression of cell fate determining factors and STAGE-SPECIFIC EMBRYONIC ANTIGEN 3 (SSEA3), a cell surface glycosphingolipid, which is important for cell signaling and specific for mammalian pluripotent stem cells. All generated iPS cell lines showed a positive immunofluorescence signal for SOX 2, OCT 3/4, NANOG and SSEA 3 (Figure 7).

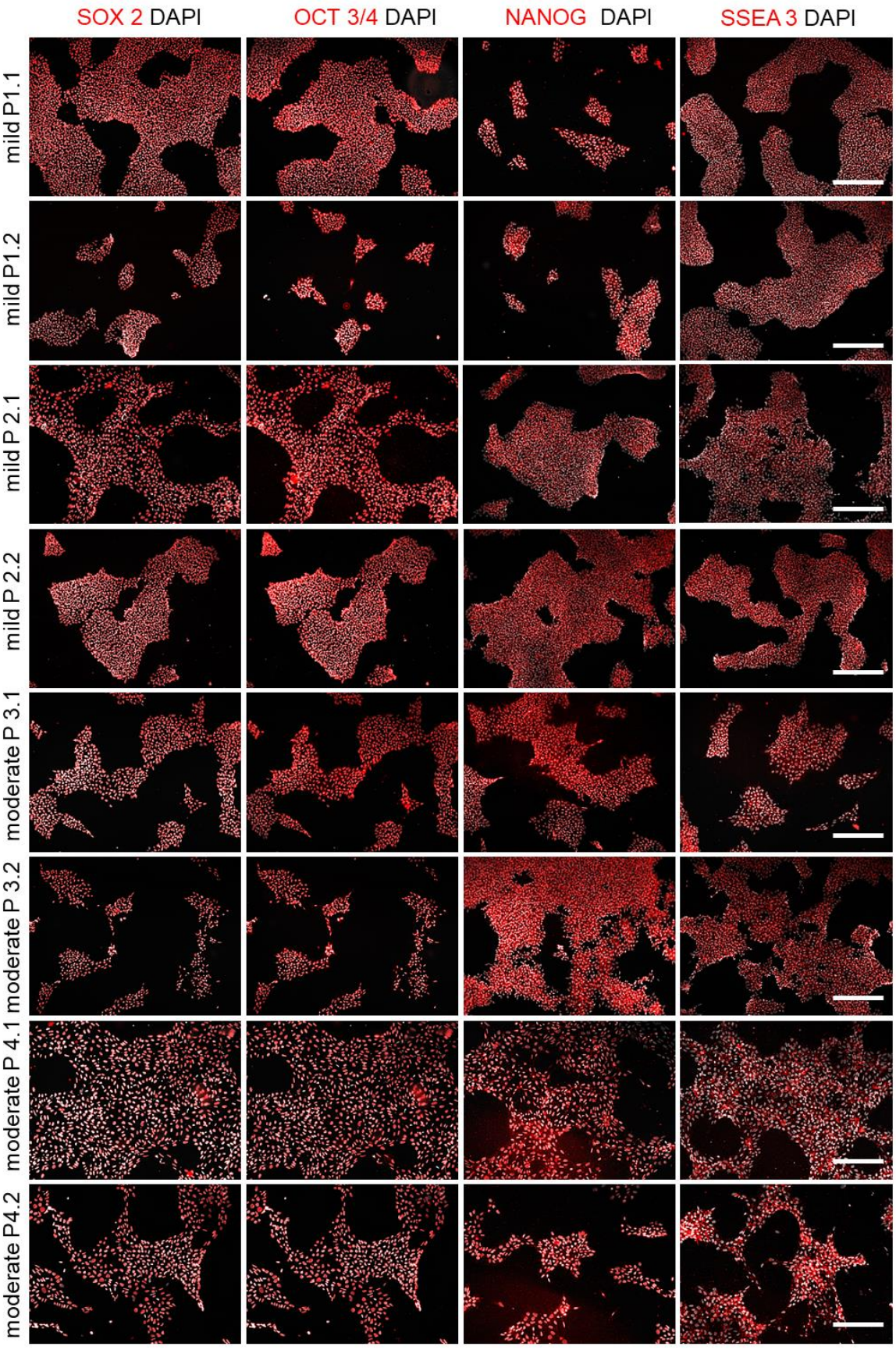
SOX 2 DAPI
OCT 3/4 DAPI
NANOG DAPI
SSEA 3 DAPI
mild P1.1
mild P1.2
mild P 2.1
mild P 2.2
moderate P 3.1
moderate P 3.2
moderate P 4.1
moderate P4.2

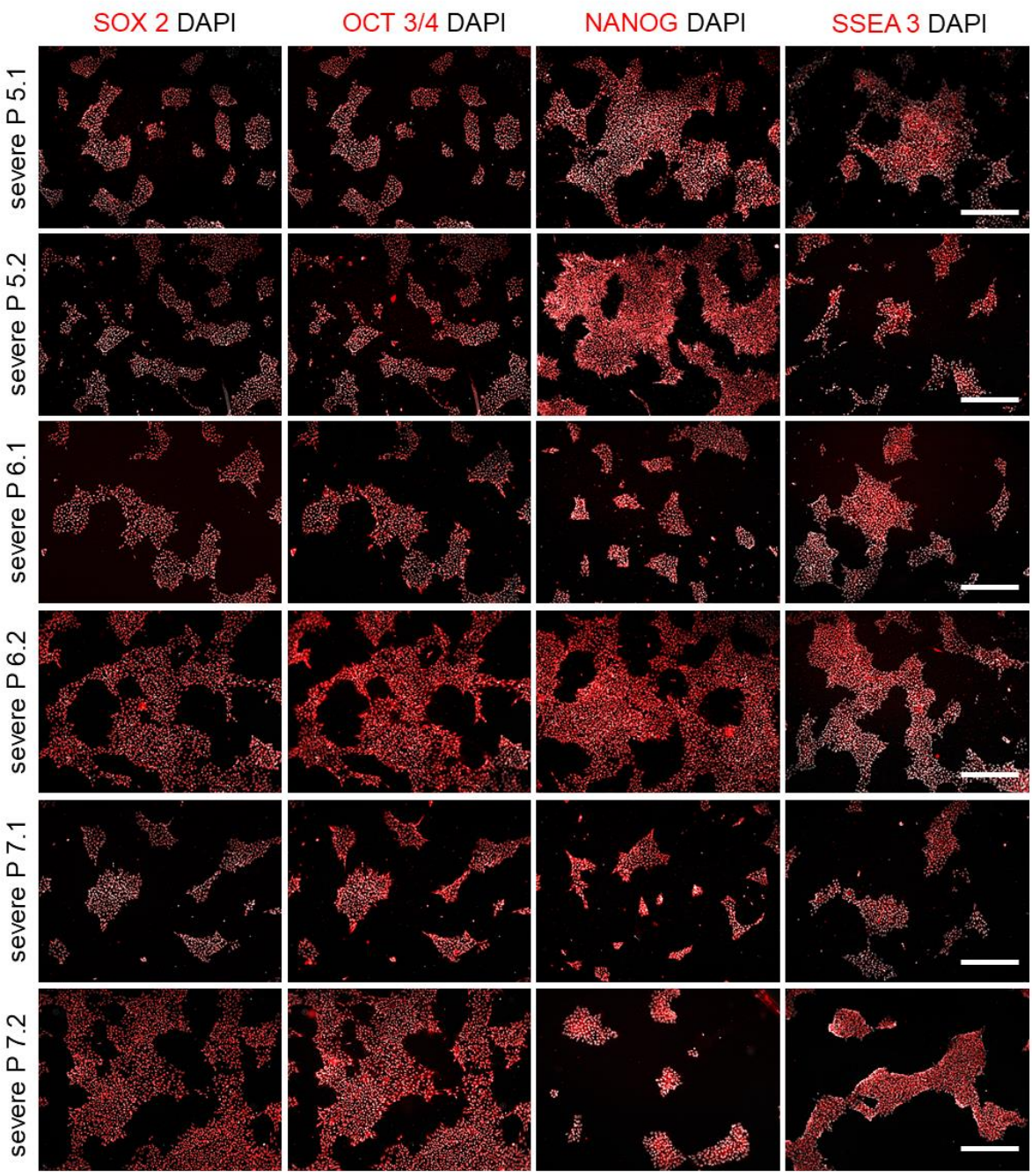

Figure 7: Immunocytochemical analysis of iPS cell pluripotency. All generated iPS cell lines (2 clones per line) were quality controlled for pluripotency including immunocytochemical staining`s for the pluripotency markers SOX 2 and OCT 3/4, which a transcription factors crucial for self-renewal of undifferentiated stem cells, NANOG, a transcription factor important for the maintenance of pluripotency through the suppression of cell determination factors, and SSEA 3, a glycosphingolipid, which is specifically on the cell surface of pluripotent stem cells. Scale bars, 50 µm.

4.1.2. Generated iPS cell lines have tripotente differentiation capacity

Pluripotency is defined by the ability of a cell to give rise to all cell types that make up the living body. To test the differentiation potential of the iPS cell lines *in vitro* into the 3 germ layers, EBs were generated and plated for spontaneous differentiation for 4 weeks without any fate determining signaling molecules. Figure 8 shows that the differentiation led to heterogenous cell populations containing a variety of cell identities. To identify the cell lineages immunocytochemical staining`s were performed for SMA, which is exclusively expressed by mesodermal lineage cells, AFP, a marker for endodermal cells and TUBB3 for the identification of ectodermal lineage cells. All generate iPS cell lines showed tripotente differentiation capacity (Figure 8 A-F).

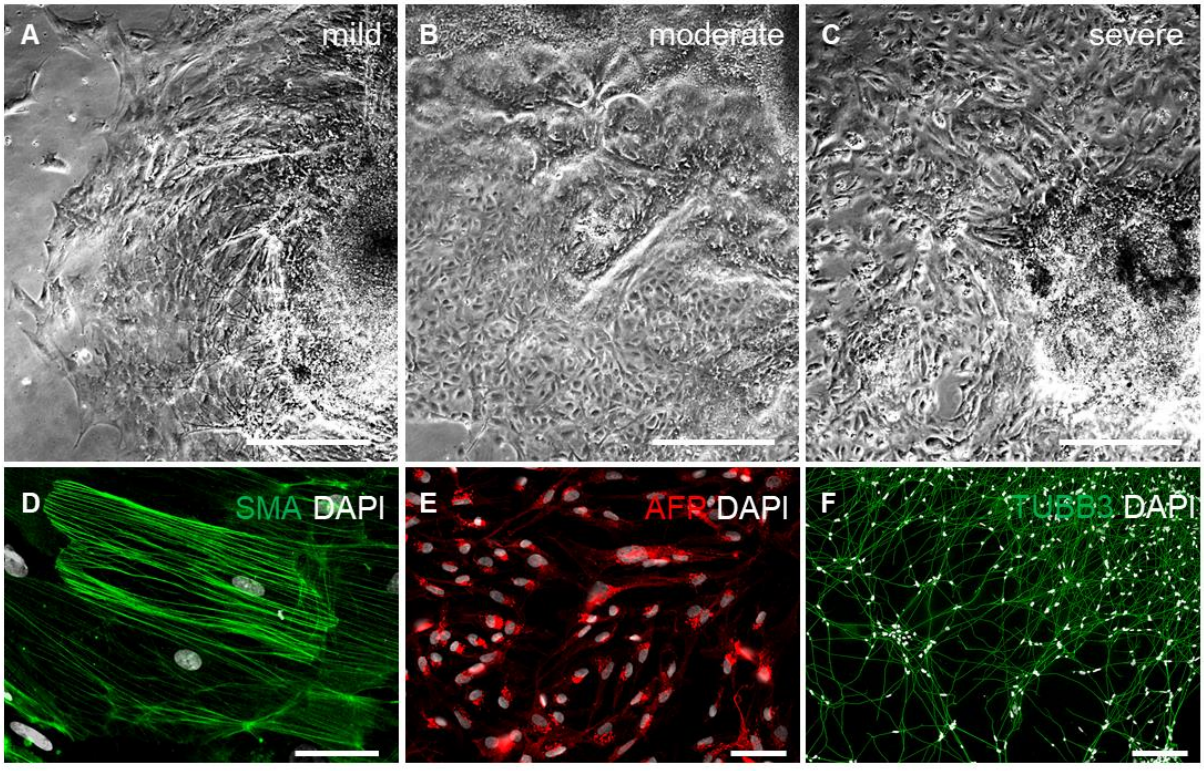

Figure 8: Assessment of tripotente differentiation capacity into the 3 germ layers endoderm, mesoderm and ectoderm. (**A-C**) Representative brightfield recordings of 4 weeks differentiated iPS cells without morphogenic cues from 1 mild LIS1-patient patient line (P2.1) (A), 1 moderate LIS1-patient patient line (P4.2) (B) as well as from 1 severe LIS1-patient line (P5.2) (C). (**D-F**) Representative immunocytochemical recordings for the mesoderm marker smooth muscle actin (SMA) (D), the endoderm marker α-fetoprotein (AFP) (E) and the ectoderm marker ß-III-tubulin (TUBB3) (F). Scale bars 20 µm.

4.1.3. Generated iPS cell lines have a normal karyotype

Since the reprogramming of somatic cells became a wide used tool to study development and disease, multiple studies have concentrated on the analysis of chromosomal stability during reprogramming and iPS *in vitro* cell culture using high-resolution genome-wide approaches (Chia et al. 2017; Taapken et al. 2011). Due to the high-frequent accumulation of genomic alterations in iPS cells, it is particularly important to continuously monitor the genomic integrity of generated and cultured iPS cells. Such genomic alterations may influence the developmental potential and can lead to non-disease-associated phenotypes as well to malignant capacity of the cell lines. Within this project high density snp analysis were performed to monitor the genomic status of the LIS1-patient iPS cell lines and detect possible chromosomal copy number variations (CNV) (Figure 9). Figure 9 shows for all generated iPS line the B allele frequents (BAF) and the Log R ratio (LRT) graph for every chromosome. To generate such graphs the allele-specific signal intensities from genotyping arrays were integrated with information on SNP spacing and SNP allele frequencies by a hidden Markov model (HMM) algorithm. BAF is a measurement of the allelic intensity ratio, the value should be around 0,5. The LRR is a normalized measurement of total signal intensity. All generated iPS cell lines showed BAF and LRR values in non-concerning ranges (Figure 9). The chromosomal integrity was given. When a deletion CNV would have occurred, the values would cluster around 0 or 1. In case of a duplication the values would have been around 0, 0,33, 0,67 and 1. The mathematical data integration and graph visualization was performed by Josef Frank from the Department of Genetic Epidemiology headed by Prof. Rietschel.

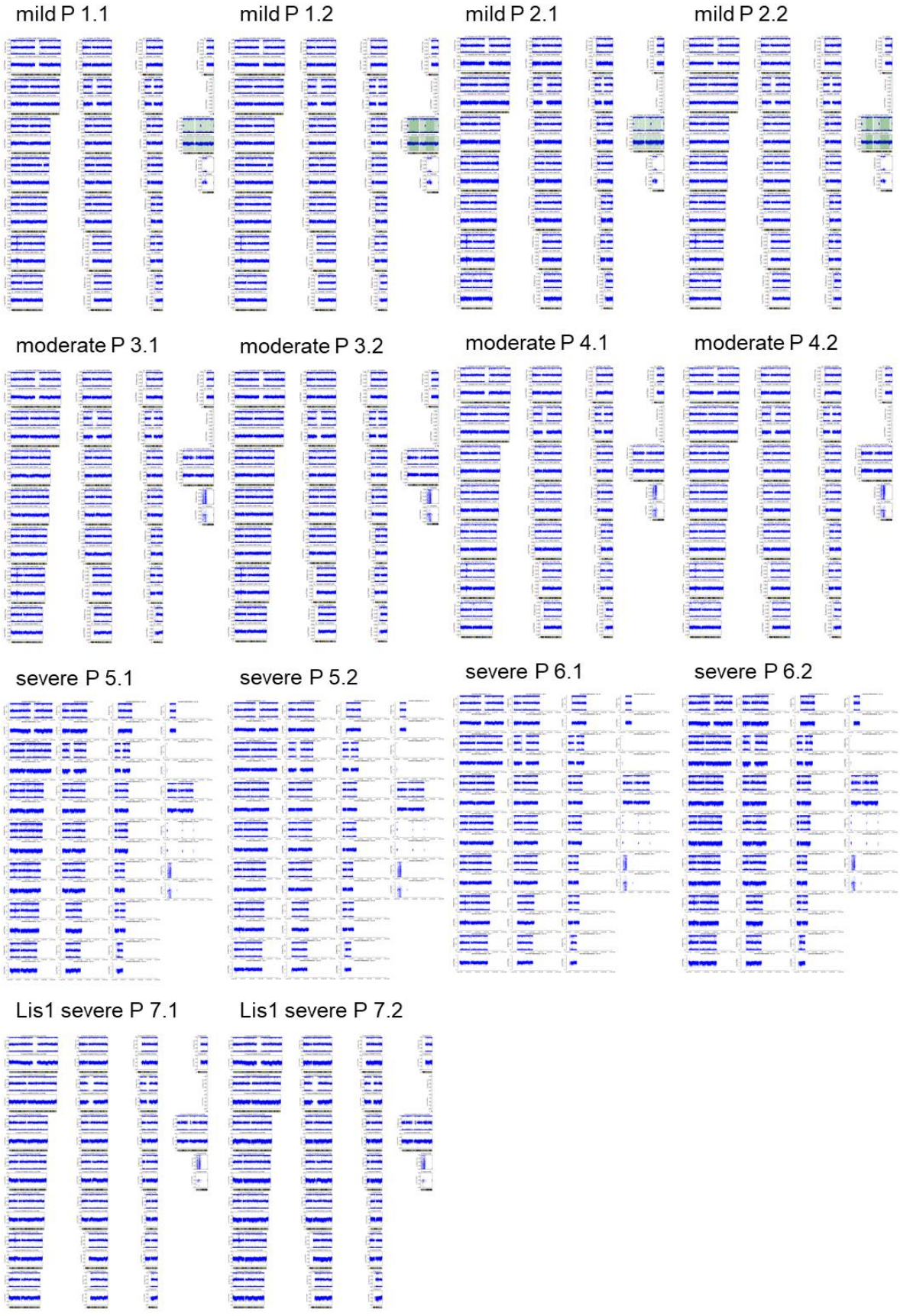
mild P 1.1
mild P 1.2
mild P 2.1
mild P 2.2
moderate P 3.1
moderate P 3.2
moderate P 4.1
moderate P 4.2
severe P 5.1
severe P 5.2
severe P 6.1
severe P 6.2
Lis1 severe P 7.1
Lis1 severe P 7.2

Figure 9: Validation of karyotypic integrity. All generated iPS cell lines were high resolution single-nucleotide polymorphism (snp) analyzed for chromosomal integrity. The graphs illustrate the B allele frequents (BAF) and the Log R ratio (LRT) for every chromosome. BAF is an allelic intensity ratio, the value should be around 0,5. When a deletion chromosomal copy number variation (CNV) occurred the value clusters around 0 or 1. When a duplication is present the values are around 0, 0,33, 0,67 and 1. The LRR is a normalized measurement of total signal intensity. When a deletion CNV happened the LRR values for snp markers in this region decreased and when a duplication is present the values increased.

4.1.4. Generated iPS cell lines harbor the respective patient-specific LIS1 mutations

One major goal of this project is to elucidate the consequences of patient-specific LIS1 mutations. Consequently, it was mandatory to validate the different LIS1 mutations in the generated iPS cell lines. To do so, the gene regions of interest were amplified by PCR, purified by DNA electrophorese and Gel extraction and then sanger sequenced. Each LIS1-patient line harbored the respective patient-specific LIS1 mutation (Figure 10 A-G). The 2 mild LIS1-patient lines (mild LIS1-patient P1 and P2) had a base exchange from cytosine to thymine (T>C) on position 569-10 in the coding sequence (c.569-10T>C) (Figure 11 A, B). The moderate line P3 had a deletion of nucleotide 13 in the coding sequence (c.13del) (Figure 10 C) and the moderate line P4 was characterized by a deletion of exon 11 (del Ex11) (Figure 10 D). Due to this deletion the validation of del Ex11 was done by whole exome sequencing. The 3 severe LIS1-patient lines (severe LIS1-patient) had different point mutations in the coding sequence. The severe LIS1-patient line P5 had a base exchange from guanine to adenine at position 1002+1 in the coding sequence (c.1002+1G>A) (Figure 10 E). The second severe LIS1-patient line P6 had a base exchange at position 531 from guanine to cytosine in the coding sequence (c.531G>C) (Figure 10 F) and the third severe LIS1-patient line P7 had a base exchange at 445 from cytosine to thymine in the coding sequence (c.445C>T) (Figure 10 G). The sequencing of the 2 mild LIS1-patient lines and the 2 moderate LIS1-patient lines were performed at the pediatric neurology, Necker Enfants Malades university hospital/ institute imagine (INSERM) by Camille Maillard.

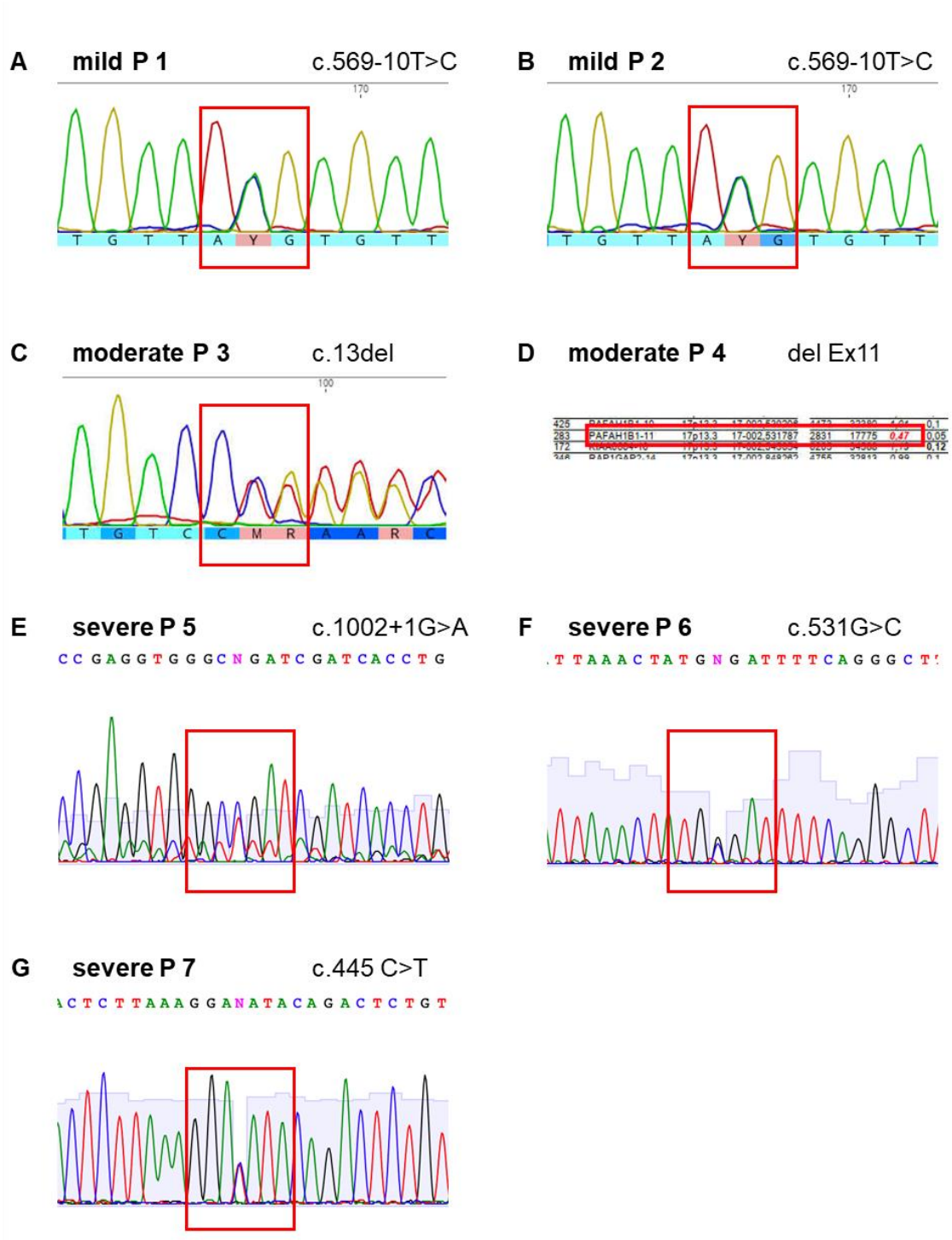

Figure 10: Validation of the respective patient-specific LIS1 mutation in the generated iPS cell lines. (**A-G**) Electropherograms generated by sanger sequencing. The mild LIS1-patient lines P1 and P2 carry a point mutation at c.569-10 T>C (A,B), the moderate LIS1-patient P3 have a deletion at position 13 in the coding sequencing causing a frameshift in the following sequence (C), the moderate LIS1-patient P4 has a deletion of exon 11 (D), the severe LIS1-patient P5 a point mutation at c.1002+1G>A (E), the severe LIS1-patient P6 a point mutation at c.531 G>C (F) and severe LIS1-patient P7 a point mutation at c.445 C>T (G). The sequencing for mild 1, 2 and moderate 1, 2 was done by Camille Maillard at the hospital Neckar Enfants Malades in France explaining the different illustration when comparing A-D with E-G (Sanger sequencing method was performed in the same way, except the exon 11 deletion of 732 was validated by whole exome sequencing).

4.2. Development of a 3D cerebral forebrain-type organoid protocol for the analyzes of early aspects of human brain development

In order to test the capacity of cortical organoids to recapitulate disease severities a standardized organoid protocol was developed (outlined in Figure 11 A, puplished in Krefft et al. 2018 and Iefremova et al. 2017), which leads to highly homogenous cortical forebrain-type organoid cultures. During the time course of the protocol there were several opportunities to quality control the generated organoid batches, defined as 'go' (continue the differentiation process) and 'no-go' (suboptimal cultures, it is recommended to terminate the batch) criteria (Figure 11 A-K). The first critical step in generating forebrain-type organoids was to start with high-quality monolayer iPS cell cultures without differentiated cells (Figures 11 B, C). In the second step, it was crucial to use the right cell number for EB formation (see 3.1.9), which was dependent on the cell line used. In general, a smaller cell number led to more vital organoids. The first detailed inspection of the iPS cells aggregates was performed on day 2. At this stage, the aggregates had formed compact cell buds with smooth edges ('go') whereas irregular appearing aggregates or aggregates with cavities were discarded ('no-go') (Figures 11 D, E). The next quality control step was performed at day 10 of the protocol. At this time point, the cell aggregates had smooth and optically translucent tissue on the outer surface representing induction of neuroectoderm ('go') whereas the absence of such tissue indicates suboptimal neural induction ('no-go') (Figures 11 F, G). Only those aggregates that exhibit a translucent surface (Figure 11 F) were embedded into GT. Once embedded, the cortical organoids developed continuous neuroepithelial VZ structures, which expanded quickly over time Figure 11 H, J ('go'). In case the organoids did not develop polarized neural ectoderm ('no-go' as illustrated in Figure 11 K) 3D cultures were discarded. Due to constant advances in the field of 3D cell culture the published protocol was in the following years further improved by adding specific substances for cell type maturation from day 35 on (see 3.1.9).

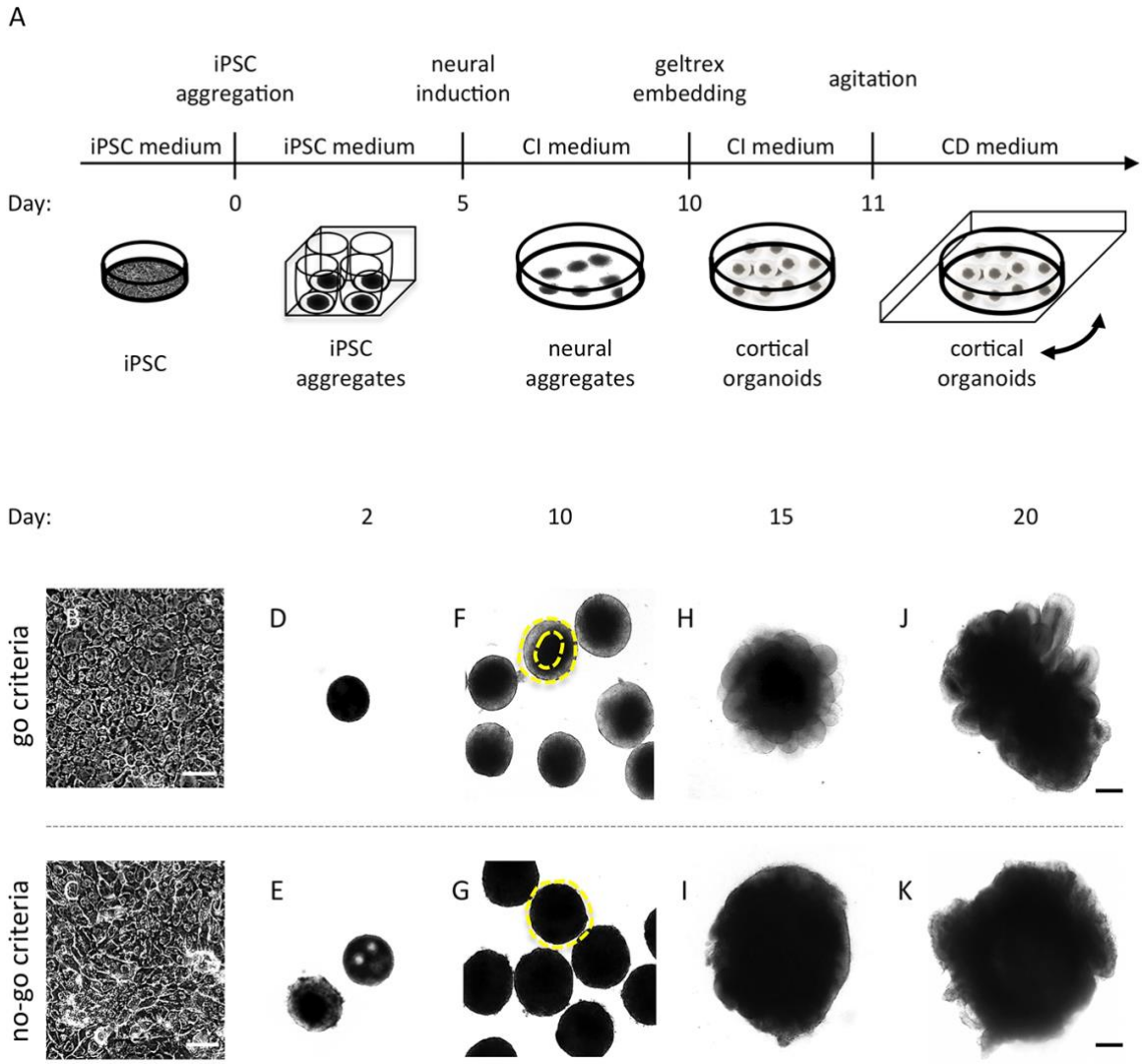

Figure 11: Schematic overview of the organoid protocol and illustration of 'go' and 'no-go' criteria. (**A**) Schematic overview of the protocol. CI medium: cortical induction medium; CD: cortical differentiation medium. (**B-C**) Image of an optimal 90% confluent iPS cells monolayer culture (B) and a non-suitable iPS cell culture exhibiting differentiation (C). (**D-E**) An iPS cells aggregate optimal in size, cell density, and surface appearance (D) and two 'no-go' cell aggregates, which exhibited either cell spares cavities (E, upper aggregate) or irregular edges (E, lower aggregate) 2 days following cell aggregation. (**F-G**) Cell aggregates exhibited translucent and smooth edges (F) and cell aggregates, which lacked optical clearing (G). The yellow line visualizes the area of interest. (**H-K**) An optimal organoid with continuous neuroepithelial ventricular zone structures (H, J) and an organoid that failed to develop radially organized neuroectoderm (I, K) imaged at day 15 and day 20, respectively. Scale bars, (B-C) 500 µm; (D-K) 200 µm. Figure published in JoVE (Krefft et al., 2018).

The established protocol led to highly homogenous organoid batches (Figures 12 A-C), with ≥ 90% homogeneity in polarized neural ectoderm formation within and across batches (Figure 12 C).

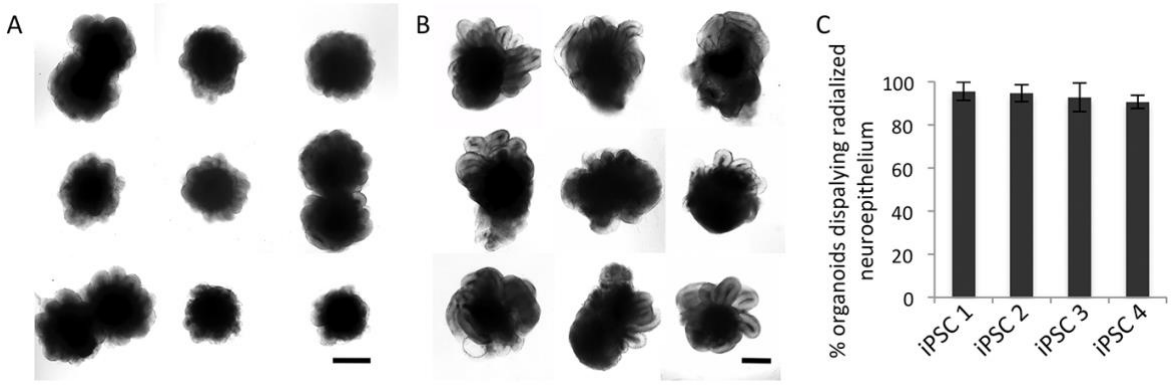

Figure 12: Homogeneity and reproducibility of the forebrain-type organoid protocol. (**A-B**) Representative bright-field images of organoids from 1 batch at day 15 (A) and day 26 (B). (**C**) Quantitative analyzes of organoids at day 20. Organoids which display at the outer surface a neuroepithelium, recognizable in bright-field as optically clear superficial tissue with a clear border and evidence of radial cellular architecture were quantified (n = 3 per iPS cell line with at least 16 organoids per experiment). Scale bars, A, B 500 μm. Error bars ± SD. Figure published in JoVE (Krefft et al., 2018).

To validate the telencephalic identity of the organoids immunofluorescence and PCR analysis were performed at day 20. Figure 13 shows that organoid neuroepithelial VZ structures expressed the neural stem cell marker SOX 2 (Figure 13 B, D), the forebrain markers PAX 6 and OTX 2 (Figure 13 C, E) and the dorsal cortical marker EMX 1 (Figure 13 F). Cell death was present in the inside of the organoids, which was normal and did not affect the development of cortical tissue. In addition, 3 organoids were used to assess the homogeneity of the protocol by gene expression analyzes using RT-PCR (performed by Ammar Jabali). The forebrain-type organoids showed expression of the dorsal forebrain markers (FOXG 1, OTX 2, EMX 1), while expression of midbrain marker (FOX 2, PAX 5) and hindbrain marker (HOXB2, HOXA4, HOXB4 and HOXB6) were not detectable (Figure 13 K).

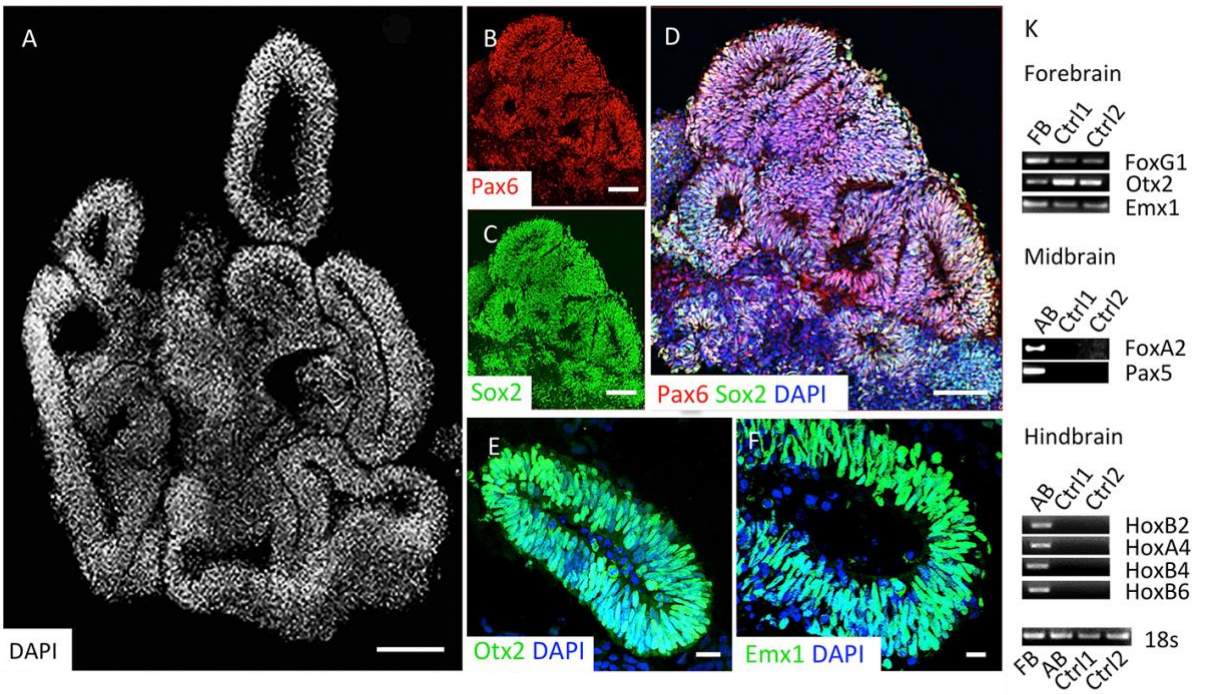

Figure 13: Validation of forebrain-type organoids at day 20. (**A-F**) Immunocytochemical characterization of organoids. Organoids organize in multiple neuroepithelial ventricular zone structures (A, counterstained with DAPI). Stratified organized cells within the neuroepithelial ventricular zone structures expressed the neural stem cell marker SOX 2 (B, D), the forebrain markers PAX6 (C, D) and Otx2 (E), as well as the dorsal forebrain marker Emx1 (F). (**K**) RT-PCR analysis for the region-specific transcription factors at day 20 of 2 independent sets of organoids derived from 2 different iPS cell lines, performed by Ammar Jabali. FB: fetal brain control; AB: adult brain control. Scale bars, A-D 200 µm; E-I 10 µm. Figure published in JoVE (Krefft et al., 2018).

Taken together the established organoid protocol led to highly homogenous forebrain-type organoid cultures, which could be used to test the utility of 3D system to model different disease severities. To be able to sensitivity detect severity-dependent phenotypic differences quantitative assessment protocols were designed.

4.3. Development of quantitative assessment protocols for 3D cerebral organoids

To have persuasive data and make conclusive assumptions it is necessary to put observed phenotypes in numbers and deliver trustworthy statistics. The organoid technology is a young research field and reliable quantitative assessment protocols were not published when I started my PhD project in 2016. Due to this, I developed complex quantification protocols for different organoid VZ structure parameters to precisely assess cortical development in a dish and to compare organoids derived from different disease severities, patients and batches (published in Iefremova et al. 2017).

4.3.1. Analyzing ventricular zone structure dimensions

Each organoid consists of many cortical VZ structures and each of those VZ structure is a model for cortical development mimicking neural tube-like morphology. Consequently, it can be said that each organoid VZ structure is a technical repeat when it comes to the quantitative assessment of cortical organoids and provides valuable information when analyzing corticogenesis in health and disease. To assess the structures in detail, I determined multiple parameters, which enabled thorough comparison of VZ dimensions between disease severities, patient iPS cell lines and organoid batches. The parameters included the VZ structure diameter (A), the length of apical (B) and basal membrane (C), the ventricle-like area (D), the VZ structure tissue area (E) and the total VZ structure area (F) (Figure 14 A-E). To perform the quantifications, organoid slices were stained with DAPI to visualize VZ structure dimensions. Images were acquired with the inverted Leica DMIL LED Microscope with the Thunder imaging software (Leica) and analyzed using FIJI. For the quantification of the VZ structure diameter 3 length measurements forming a right-angle fan area pointing to the nearest pial surface, at 0, 45 and 90 degree were pooled (Figure 14 A). The VZ structure tissue area was defined as the ratio of the total VZ structure minus the ventricle-like area (Figure 14 E). Calculations and data tablets were done in Microsoft Excel.

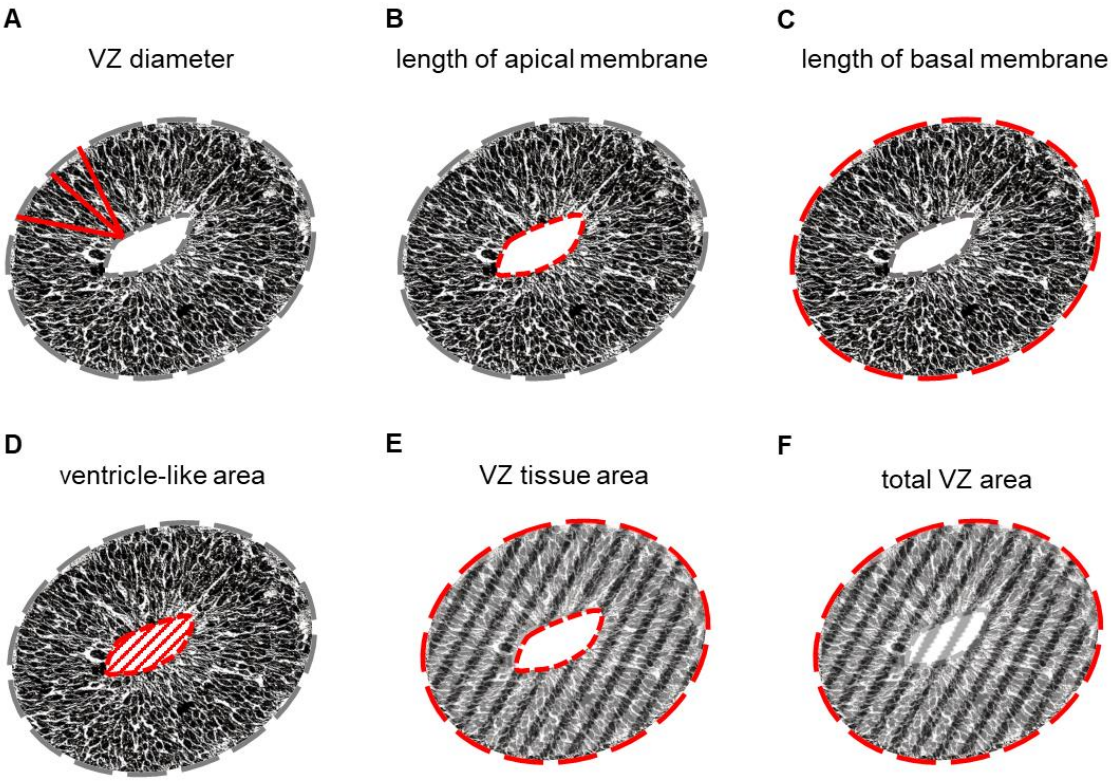

Figure 14: Schematic illustration of ventricular zone structure parameters. (**A-F**) Each ventricular zone (VZ) structure contained important information about the cytoarchitectural development of each neural tube-like structure. The VZ structure diameter was determinant by 3 length measurements (µm) forming a right-angle fan area pointing to the nearest pial surface, at 0, 45 and 90 degree (A). The apical (B) and basal (C) membrane length were determined by the diameter of VZ structure and ventricle-like structure. The other 3 parameters were area measurements (µm^2) for the VZ structures including the ventricle-like area (D), the VZ structure tissue area (E) and the total VZ structure (F). All parameters taken together enabled a reliable assessment of VZ structure dimensions and consequently a detailed comparison between organoid batches, patients and severities.

4.3.2. Quantification of astral tubulin strand densities

For the determination of stabilizing astral α-tubulin density, organoid slides were stained with acetylated ALPHA-TUBULIN (AC-TUB). Images were acquired with the inverted Leica DMIL LED Microscope with the Thunder imaging software (Leica). To determine the signal to noise ratio a plot profile line (Figure 15 A, yellow lines) was drawn into the AC-TUB recordings into the apical (3third percentile, apical side) and basal (66th percentile, basal side) region of the VZ structure using FIJI (Figure 15 A-B). The plot profile was pasted into a self-designed Excel file, which contained mathematical formulas to calculate the mean strand density. In the first step, the measurements of every second pixel were considered, because every strand was about 2 pixels wide. Then the background signal was determined, and the file automatically counted the signal peaks above the background signal (Figure 15 B, peaks above the red line). The number was normalized against the total length of the plot profile line resulting in a mean density of strands crossing the line (*100 = %).

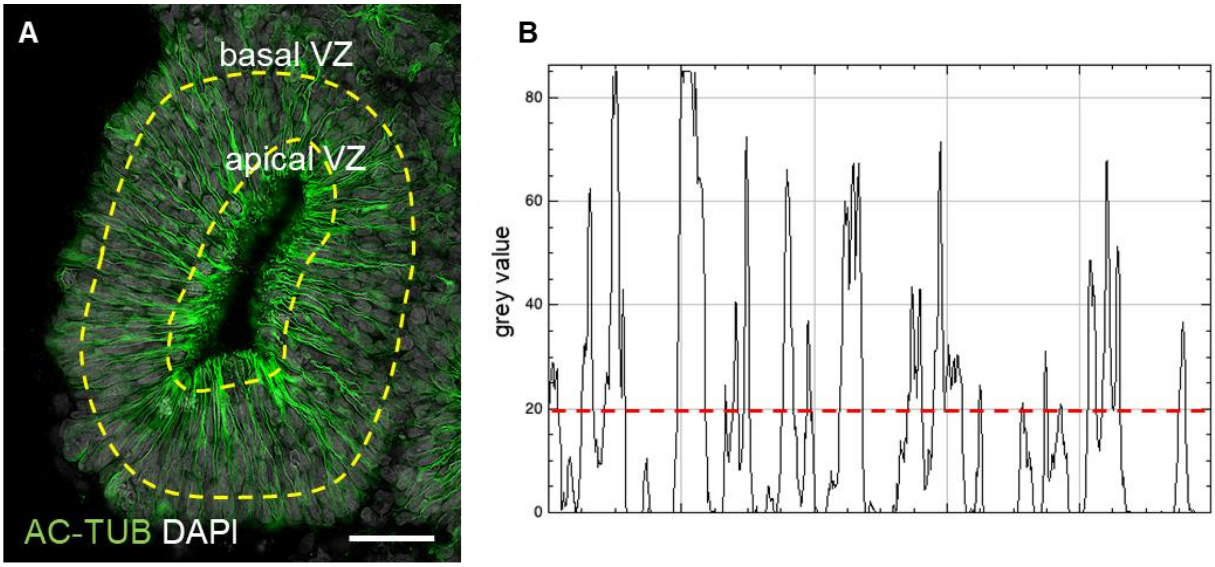

Figure 15: Quantification protocol of acetylated α-TUBULIN strand density. Organoid slices were stained for ACETYLATED α-TUBULIN (AC-TUB) and the signal plot profile was drawn into the apical and basal ventricular zone (VZ) region using FIJI. The Plot profile was pasted into a self-designed Excel file, which contained mathematical formulas to calculate the mean strand density. In the first step the measurements of every second pixel were considered, because every strand was about 2 pixels wide. Then the background signal was determined, and the file automatically gave the number of signals on the plot profile line, which were above the background signal. The number was normalized by the total length of the plot profile resulting in a mean density of strands crossing the line (*100=%). Scale bar, 20 μm.

4.3.3. Determination of apical membrane alignment diameter

Each VZ structure is surrounded by the apical membrane, which contains many important proteins and is important for organoid niche integrity for correct morphogenic signaling. Consequently, a quantification protocol for the assessment of apical membrane disruption was established by measuring the membrane thickness at 90°, 180°, 270° and 360° to the VZ structure center using FIJI (Figure 16). The mean value of those 4 measurements were analyzed as the mean disruption diameter of apical membrane alignment. The membrane alignment was visualized by N-CAD staining. The data was analyzed using Microsoft Excel.

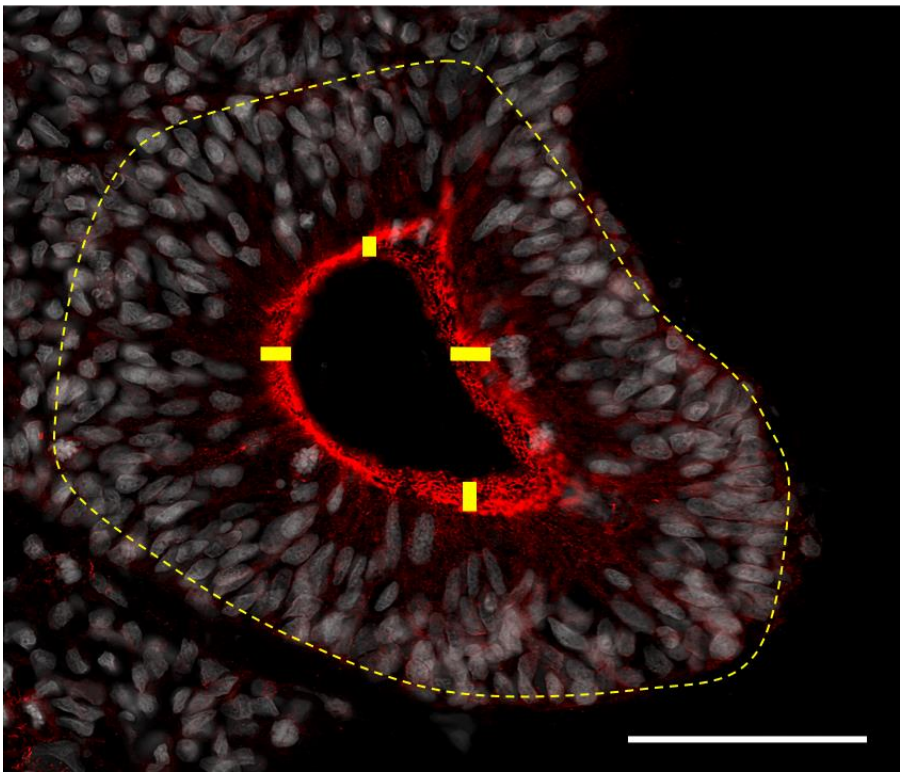

Figure 16: Apical membrane diameter quantification. Organoid slices were stained for DAPI for ventricular zone structure tissue visualization and N-CADHERIN (N-CAD) to analyze the apical membrane. The membrane thickness was measured at 90°, 180°, 270° and 360° to the ventricular zone structure center using FIJI. Scale bar, 20 μm.

4.4. Cerebral organoids derived from LIS1-patients reflect disease severity in the degree of alterations in cytoarchitecture and neurogenesis

The alteration of gyrification is one hallmark of lissencephalic brains. In terms of LIS1-lissenephaly this hallmark is differentially pronounced without known cause. For this study 7 patients were selected from a LIS1-patient cohort comprising 63 cases, which cover the whole spectrum of gyrification alterations of LIS1-lissencephaly ranging from Dobyns grade 5 (mild) to 1 (severe) (Barkovich et al. 2012a). Each patient harbors a different molecular characterized heterozygous mutation in the LIS1 gene (Table 1). One example magnetic resonance image (MRI) for control and each severity class (mild, moderate and severe) is depicted in Figure 17 A. Health human brains are characterized by manifold gyri and sulci. Whereas mild LIS1-patients often have a reduced number of gyri and sulci (Figure 17 A, mild LIS1-patient patient P1). In contrast, moderate LIS1-patients often show a gradient of severity with anterior pachygyria and posterior agyria (Figure 17 A, moderate LIS1-patient patient P3) and LIS1-patients suffering from severe disease are characterized by complete agyria (Figure 17 A, severe LIS1-patient P7). One major question which should be deciphered within this project was, whether the organoid system is sensitive enough to reflect those disease severities. To approach this question the generated LIS1-patient iPS cell cohort and 6 age and gender matched controls were subjected to the developed 3D cerebral organoid protocol and 3D tissues were analyzed with the designed quantitative assessment methods. The organoid morphology was specific for the LIS1-patients severity (Figure 17 B). While organoids from control and LIS1-patients with mild disease gradually developed smooth neuroepithelial loop-like structures which expanded over time, organoids from patients with moderate disease appeared to be generally smaller in size (Figure 17 B). In contrast, organoids from severe LIS1-patients did not seem to be smaller compared to control derived organoids but developed irregular edges with single cells growing out of the structures (Figure 17 B, magnification on the right). Following whole-tissue clearance and immunohistochemical staining I found that the organoids derived from patients with severe disease were covered by a large belt of neurons, which was less abundant in mild and moderate conditions and nearly absent in control derived organoids (Figure 17 C). This phenomenon was also apparent following cry-sectioning and immunohistochemical staining (Figure 17 D). Next, I analyzed the architecture of the neuroepithelial VZ structures within the organoids in detail. Organoids derived from healthy individuals exhibited multiple large cortical VZ structures at day 20. Whereas the LIS1-patient organoids displayed a size reduction of VZ structures (Figure 17 E).

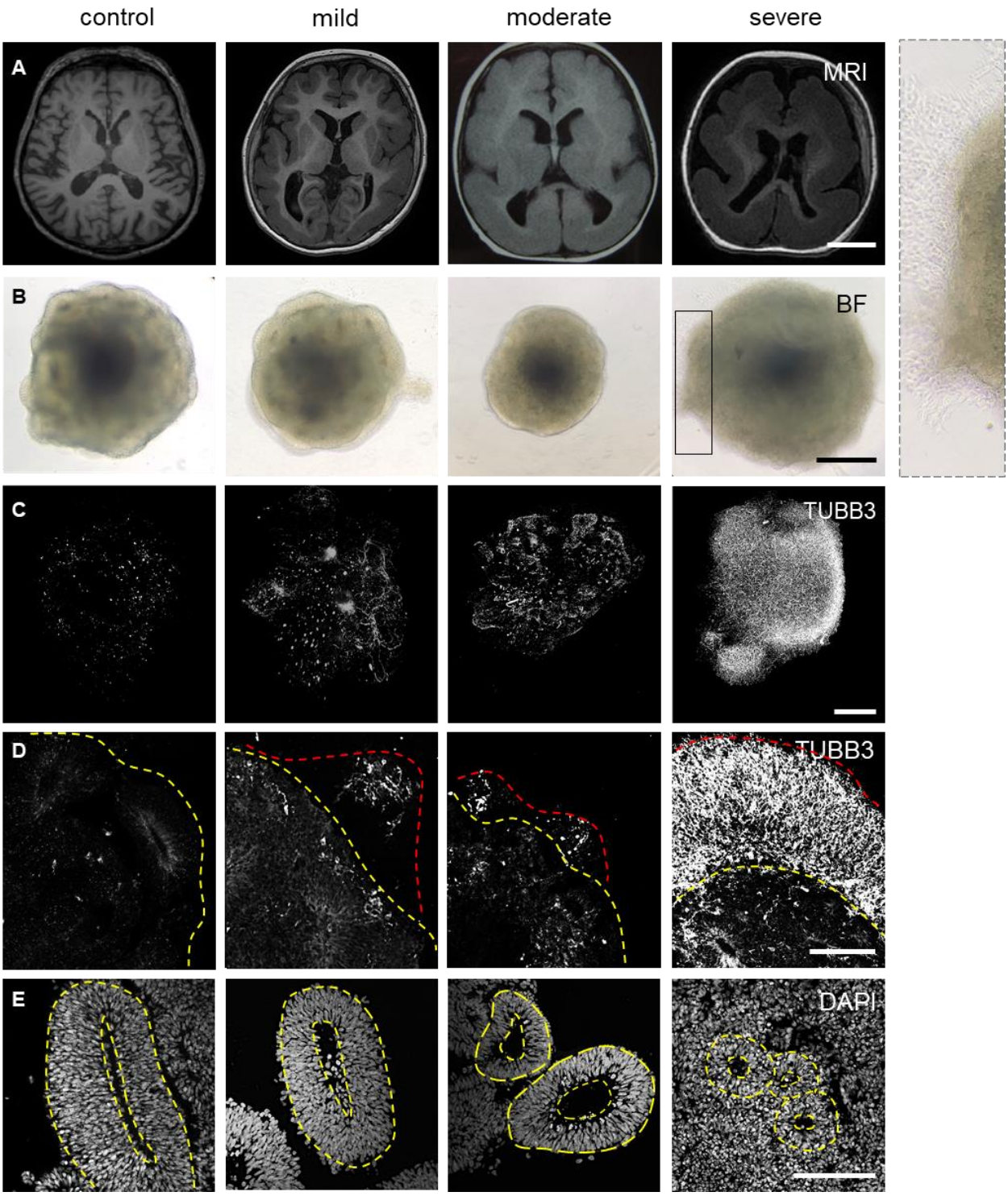
control
mild
moderate
severe
A
MRI
B
BF
C
TUBB3
D
TUBB3
E
DAPI

Figure 17: Organoid morphology is specific for LIS1-patient`s severity. (**A**) LIS1-patient MRI recordings provided from Dr. Nadja Bahi-Buisson from the hospital Neckar Enfants Malades (mild LIS1-patient patient 1, moderate LIS1-patient patient 1 and severe LIS1-patient 3). **(B**) Representative brightfield field (BF) recordings of control C1.2, mild LIS1-patient P1.1, moderate LIS1-patient P3.1 and severe LIS1-patient P5.1 patient derived organoids at day 20. **(C**) Representative light sheet microcopy (LSM) recordings of whole-tissue cleared control 2.1, mild LIS1-patient P1.1, moderate LIS1-patient P3.2 and severe LIS1-patient P5.1 derived organoids at day 20 stained for ß-III Tubulin (TUBB3). **(D**) Representative TUBB3 recordings of control C4.1, mild LIS1-patient P2.1, moderate LIS1-patient P4.1 and severe LIS1-patient P5.2 patient derived organoids at day 20. **(E**) Representative DAPI recordings of ventricular zone structures of control C1.2, mild LIS1-patient P1.1, moderate LIS1-patient P3.1 and severe LIS1-patient P5.1 patient derived organoids at day 20. Scale bars, (A) 5 cm, (B, C) 200 µm (D, E) 50 µm.

To that end, the VZ diameter, ventricle area, length of the apical and basal membrane, total VZ area and VZ tissue area were quantified (Figure 18 A-F). Here I found a significant reduction of all parameters in organoids derived from patients with moderate and severe lissencephaly as well as a significant reduction in 3 out of the 6 parameters analyzed in organoids derived from patients with mild lissencephaly compared to controls (Figure 18 E).

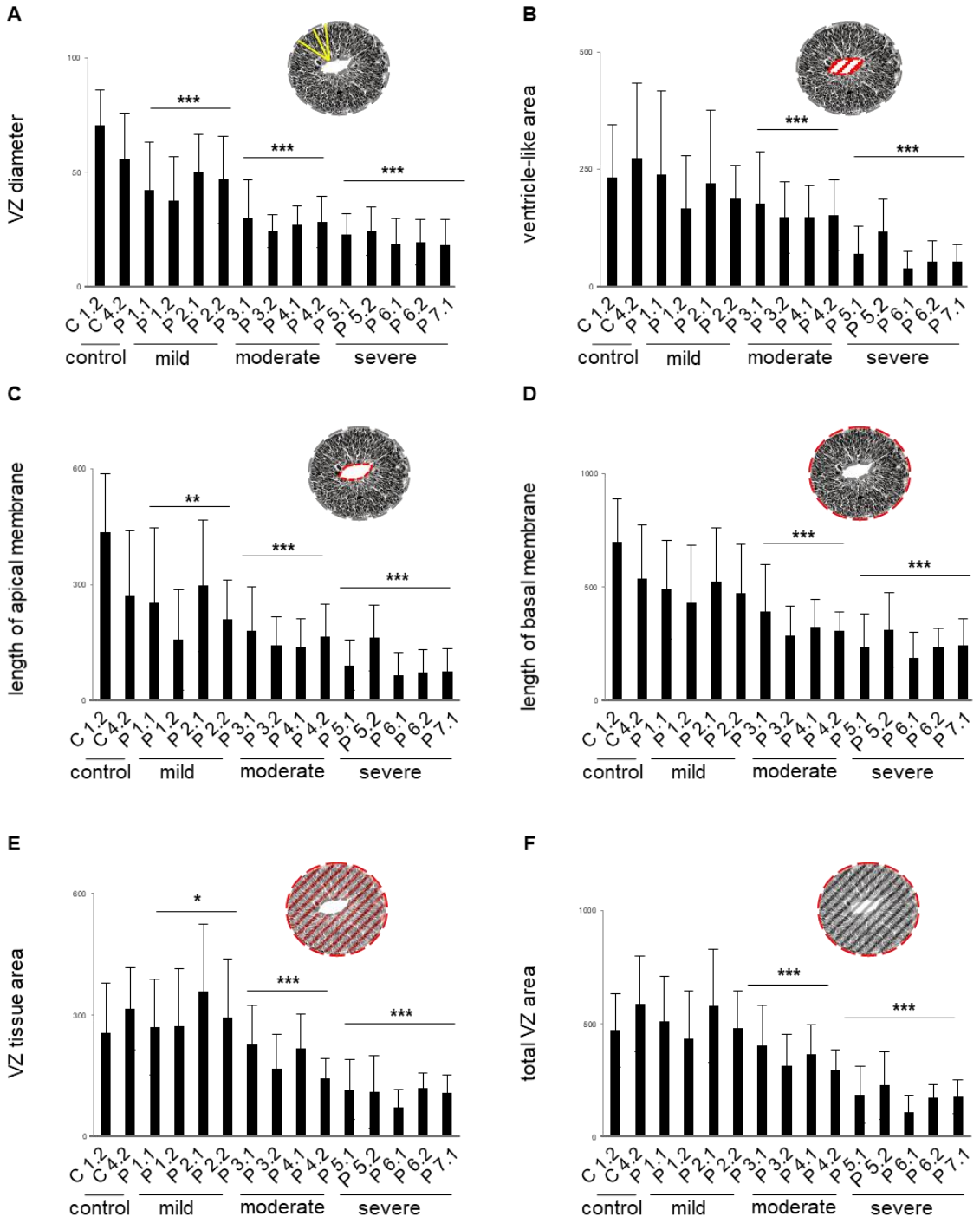

Figure 18: Ventricular zone parameter quantification reveals a gradually decrease of tissue dimensions with increasing LIS1-patient severity. (**A-F**) Quantification of ventricular zone (VZ) structure diameter, ventricle area, length of apical membrane, length of basal membrane, VZ structure tissue and total VZ structure area in control- and LIS1-patient derived organoids at day 20. control C1.2 N=38, control C4.2 N=33, mild P1.1 N=33, mild P1.2 N=19, mild P2.1 N=13, mild P2.2 N=17, moderate P3.1 N=20, moderate P3.2 N=19, moderate P4.1 N=20, moderate P4.2 N=18, severe P5.1 N=61, severe P5.2 N=49, severe P6.1 N=23, severe P6.2 N=48, severe P7.1 N=58. Error bars, ±SD. *p < 0.05, **p < 0.01, ***p < 0.001.

4.5. Molecular structure analyzes reveal a gradual breakdown of stabilizing astral tubulin and cellular organization

To assess the direct consequences of the patient-specific LIS1 mutations on LIS1 microtubule stabilizing function, the stability of the cytoskeleton of aRG cells within the VZ was analyzed by acetylated ALPHA-TUBULIN (AC-TUB) staining. Microtubules are a highly dynamic system. The acetylation stabilizes the tubulin strands, making them more prone to remodeling. Analyzes were performed in cryo-cut and whole-tissue cleared organoids to carefully detect cutting artefacts (Figure 19 A-D). The cleared organoids show an overall reduction of AC-TUB positive labeled structures with increased disease severity (Figure 19 A). The AC-TUB staining in moderate and severe condition could barely be detected in basal regions of the VZ structures, whereas in control conditions the staining was sufficient to visualize apical and basal regions of cortical structures. When investigating the individual VZ-structures in more detail I found, that in control conditions the astral tubulin strands span aligned and in close proximity from the apical- (visualized by ARL13b, Figure 19 C) to the basal side (Figure 19 B-D). In organoids derived from patients with mild lissencephaly I found a small percentage (around 10 %) of tubulin strands not reaching the basal side of the VZ structure (Figure 19 E), whereas in organoids derived from patients with moderate disease the tubulin density at the basal side was reduced by more than 20% and in organoids derived from severe patients the reduction was even more drastic (up to over 50%; Figure 19 E). This collapse of stabilizing cytoskeleton was supported by western blot analysis of AC-TUB protein level, which was with increasing patient severity progressively reduced in LIS1-patient-derived progenitors. The most drastic reduction of AC-TUB protein level was observed in cells derived from severe LIS1-patients compared to controls (Figure 19 F).

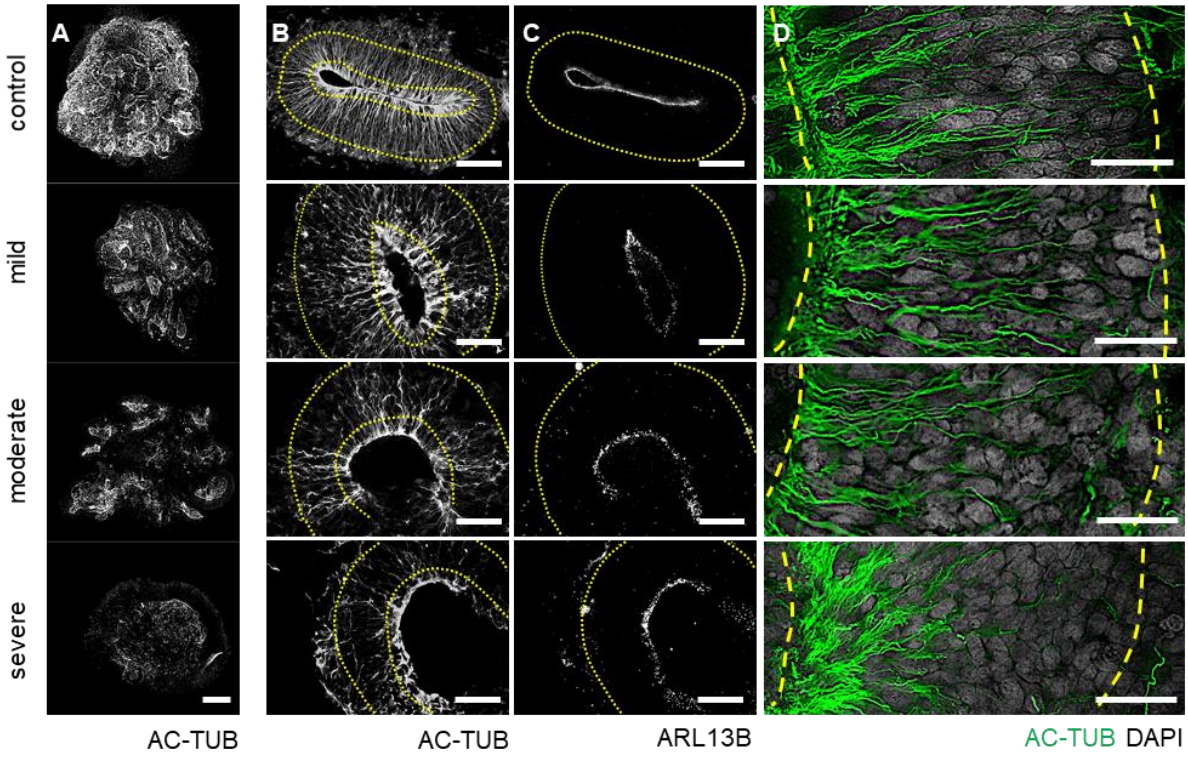
A
B
C
D
control
mild
moderate
severe
AC-TUB
AC-TUB
ARL13B
AC-TUB DAPI

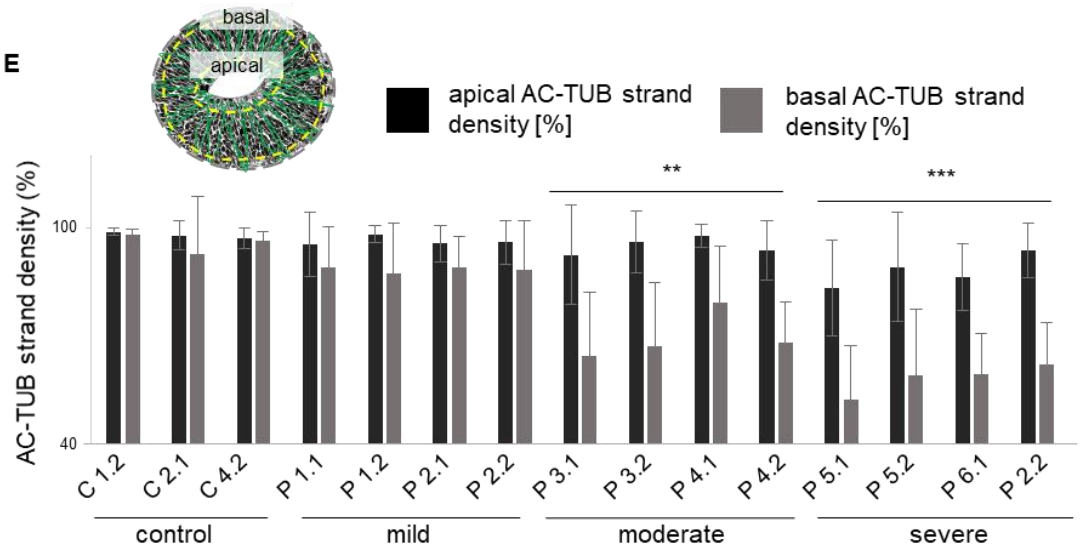
E
basal
apical
apical AC-TUB strand density [%]
basal AC-TUB strand density [%]
AC-TUB strand density (%)
100
40
**
***
C 1.2
C 2.1
C 4.2
P 1.1
P 1.2
P 2.1
P 2.2
P 3.1
P 3.2
P 4.1
P 4.2
P 5.1
P 5.2
P 6.1
P 2.2
control
mild
moderate
severe

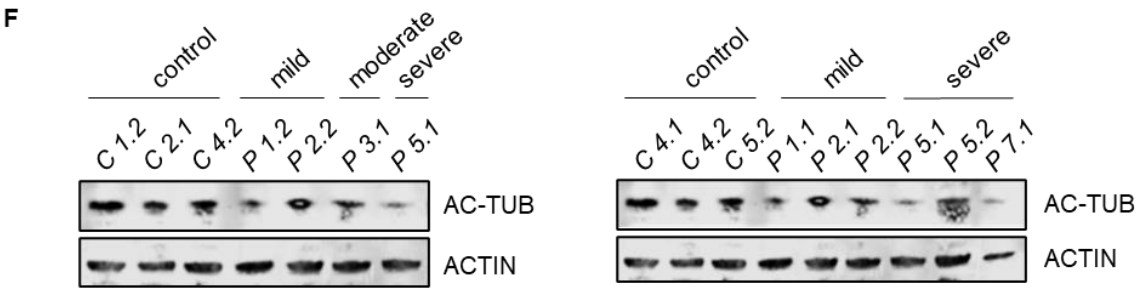
F
control
mild
moderate
severe
C 1.2
C 2.1
C 4.2
P 1.2
P 2.2
P 3.1
P 5.1
AC-TUB
ACTIN
control
mild
severe
C 4.1
C 4.2
C 5.2
P 1.1
P 2.1
P 2.2
P 5.1
P 5.2
P 7.1
AC-TUB
ACTIN

Figure 19: Gradually breakdown of cell stabilizing astral tubulin with increasing LIS1-patient severity. (**A, B**) Representative recordings of cleared and cryo-sectioned organoids from control C4.1, mild P1.1, moderate P3.2 and severe P5.2 LIS1-patient derived organoids stained for acetylated-α tubulin (AC-TUB) at day 20. (**C**) Representative recordings of ARl13b, a cilia marker, in control C4.1, mild P1.1, moderate P3.2 and severe P5.2 LIS1-patient derived organoids at day 20. (**D**) High magnification recordings of AC-TUB stained VZ structures in control C4.1, mild P1.1, moderate P3.2 and severe P5.2 LIS1-patient derived organoids at day 20. (**E**) Quantification of apical and basal AC-TUB strand density in control, mild-, moderate- and severe LIS1-patient derived organoids. control C1.2 N=12, control C2.1 N=12, control C4.2 N=20, mild P1.1 N=13, mild P1.2 N=13, mild P2.1 N=13, mild P2.2 N=15, moderate P3.1 N=13, moderate P3.2 N=12, moderate P4.1 N=12, moderate P4.2 N=14, severe P5.1 N=22, severe P5.2 N=20, severe P6.1 N=13, severe P6.2 N=13, severe P7.1 N=12). (**F**) Western blot analyzes of AC-TUB protein level in controls (C1.2, C2.1, C4.1, C4.2 and C5.2), mild- (P1.1, P2.1, and P2.2), moderate- (P3.1) and severe (P5.1, P5.2 and P7.1) LIS1-patient derived cortical progenitor cells. Scale bars, (A) 200 µm, (B) 20 µm. Error bars, ±SD. *$p < 0.05$, **$p < 0.01$, ***$p < 0.001$.

As a consequence of VZ destabilization, there was also a cellular disorganization observable by performing a hematoxylin-eosin (HE) staining of cryo-cut organoid slices at day 20 (Figure 20 A). Especially the organoids derived from moderate and even more drastic in severe disease displayed random arranged cell bodies with gaps in between cells, whereas in control conditions aRG cells arrange well organized, stringed and densely packed within the VZ. In LIS1-patient derived organoids derived from mild disease the cellular orientation was predominantly comparable to control conditions (Figure 20 A). Together with this gradient of declining cellular organization with increasing LIS1-patient severity I also found a disturbed apical membrane alignment by performing immunohistochemical staining for N-CAD (Figure 20 B). Whereas control organoids exhibit a fine adherent junction belt at the most apical side of 1-3 µm (measured by the accumulation of N-CAD), this organization was significantly altered in organoids derived from patients with severe lissencephaly (more than 10 times increased; Figure 20 C). A significant disturbed distribution of N-cadherin was also found in the moderate condition (around 20 µm) while in the mild condition a disruption could be detected although without significance (around 10 µm).

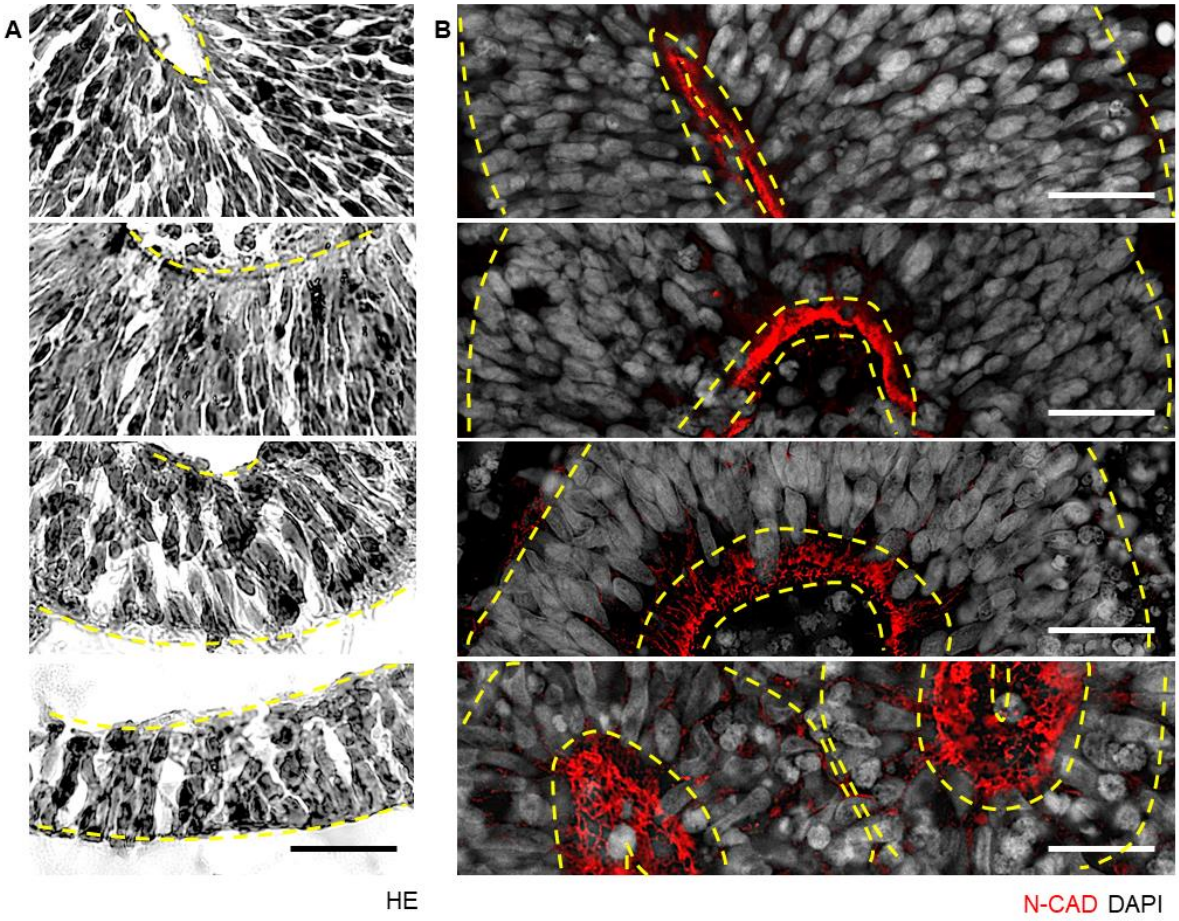
A
B
HE
N-CAD DAPI
C
apical disruption diameter (µm)
50
25
0
**
***
C 1.2
C 1.1
C4.2
P 1.1
P 1.2
P 2.1
P 2.2
P 3.1
P 3.2
P 4.1
P 4.2
P 5.1
P 5.2
P 6.1
P 6.2
P 7.1
control
mild
moderate
severe

Figure 20: Progressive disruption of cellular organization with LIS1-patient severity. (**A**) Representative recordings of hematoxylin-eosin (HE) recordings of control C4.1, mild LIS1-patient P1.2, moderate LIS1-patient P3.1 and severe LIS1-patient P5.1 derived organoids. (**B**) Representative recordings of cryo-cut organoids from control 3.1, mild LIS1-patient P2.1, moderate LIS1-patient P3.2 and severe LIS1-patient P5.1 derived organoids stained for N-CADHERIN (N-CAD) at day 20. (**C**) Quantification of apical disruption diameter in control, mild, moderate and severe LIS1-patient derived organoids at day 20. Schematic illustration of how the disruption diameter was quantified is illustrated on the right side of the diagram. control C1.2 N=12, control 2.1 N=12, control 4.2 N=20, mild P1.1 N=13, mild P1.2 N=13, mild P2.1 N=13, mild P2.2 N=15, moderate P3.1 N=13, moderate P3.2 N=12, moderate P4.1 N=12, moderate P4.2 N=14, severe P5.1 N=22, severe P5.2 N=20, severe P6.1 N=13, severe P6.2 N=13, severe P7.1 N=12. Scale bars 20 µm. Error bars, ±SD. *$p < 0.05$, **$p < 0.01$, ***$p < 0.001$.

Taken together, the analysis of molecular structures revealed a progressive breakdown of VZ structure stabilizing astral tubulin and with that a gradual disruption of cellular organization. To determine whether the patient-specific LIS1 mutations impair the microtubule stabilizing function of LIS1 protein and by that directedly course the observed phenotypic changes I tested whether a microtubule stabilizing agent rescues observed alterations.

4.6. Microtubule array stabilization can in part rescue phenotypic alterations

One major aim of *in vitro* models is to closely recapitulate *in vivo* development and associated malformations to identify molecular pathomechanisms. Such knowledge about malformation and disease-causing mechanisms can help to identify drugs, which counteract developmental mistakes. Within this project EpothiloneD, a food and drug administration (FDA)-approved macrolide binding to a common binding site on beta-tubulin for strand stabilization was tested (Fumoleau et al. 2007; Bollag et al. 1995; Giannakakou et al. 2000). Depending on the applied concentration there are 2 main objectives for EpothiloneD treatment. In high concentrations EpothiloneD binds in high doses to microtubules, completely stabilizing dynamic processes and preventing cell divisions. This utilization finds its relevance predominantly in cancer research, where malign cells divide abnormally, to stop harmful cell proliferation. The other objective acquires the usage of EpothiloneD in low dosage, to stabilize microtubules without affecting cell divisions. Based on LIS1 essentiality for microtubule stability I tested a low concentration of Epothilone D (1 nM). To determine whether the patient-specific LIS1 mutations impair the microtubule stabilizing function of the LIS1 protein and by that directedly course the observed phenotypic changes I applied EpothiloneD to LIS1-patient and control derived organoids from the start of differentiation (d10) for 5 days. The exposer of patient derived organoids to EpothiloneD resulted a significant increase in AC-TUB strand density at the basal side of the VZ structures only in LIS1-patient derived organoids, most significant in moderate and severe conditions (Figure 21 A, B). In contrast, control organoids were not significantly affected by the drug treatment (Figure 21 A, B). This stabilization of VZ structure stabilizing astral tubulin also had a positively impact, at least in part, on the cellular organization and apical membrane alignment of the LIS1-patient derived cultures (Figure 21 C, D). All LIS1-patient lines exhibited an alignment recovery of more than 10 % after 5 days of EpothiloneD treatment (Figure 21 D).

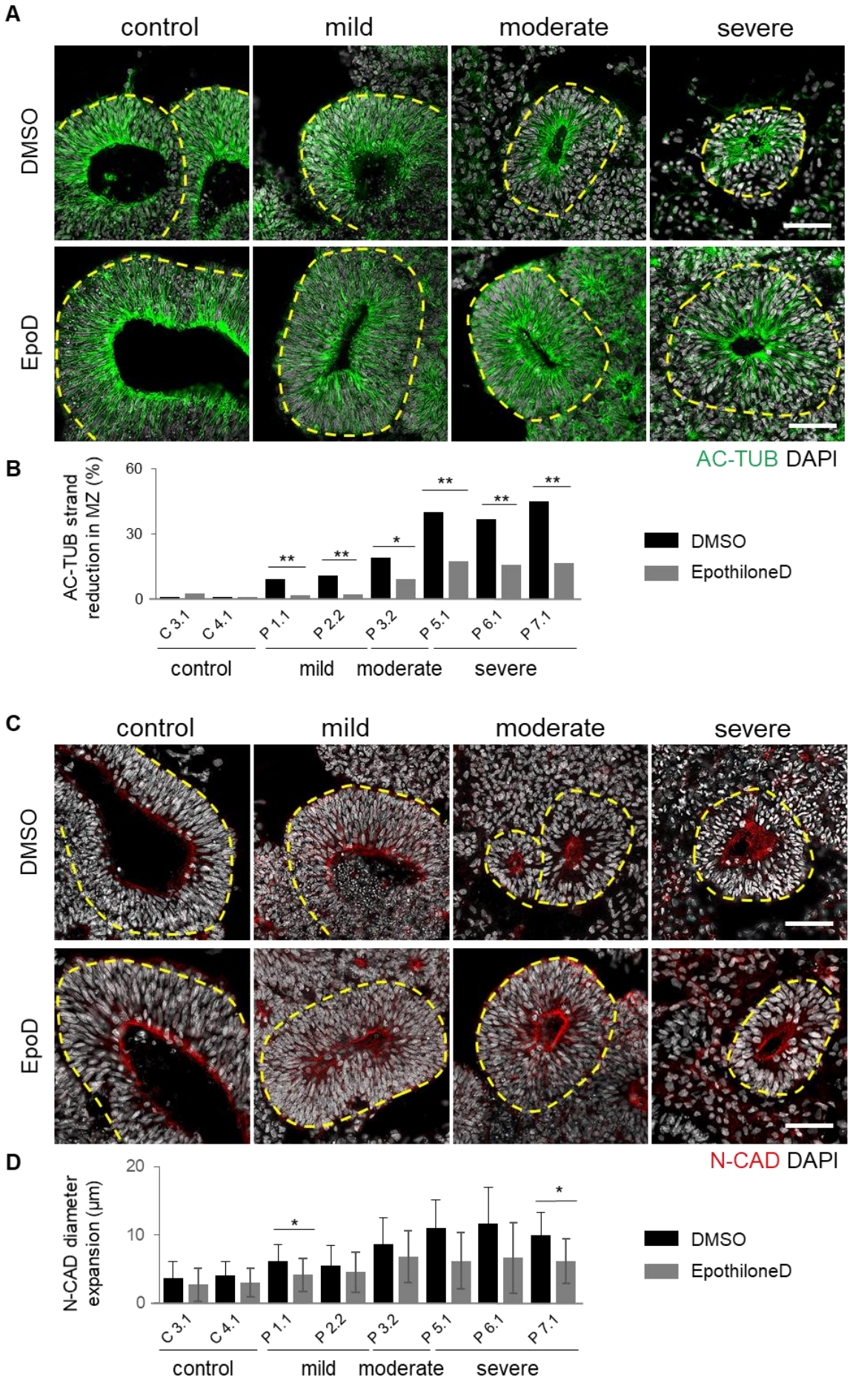
A
control
mild
moderate
severe
DMSO
EpoD
AC-TUB DAPI
B
AC-TUB strand reduction in MZ (%)
60
30
0
**
**
*
**
**
**
C 3.1
C 4.1
P 1.1
P 2.2
P 3.2
P 5.1
P 6.1
P 7.1
control
mild
moderate
severe
DMSO
EpothiloneD
C
control
mild
moderate
severe
DMSO
EpoD
N-CAD DAPI
D
N-CAD diameter expansion (µm)
20
10
0
*
*
C 3.1
C 4.1
P 1.1
P 2.2
P 3.2
P 5.1
P 6.1
P 7.1
control
mild
moderate
severe
DMSO
EpothiloneD

Figure 21: Epothilone D treatment in part rescues LIS1-associated microtubule instabilities stabilizing ventricular zone structure architecture. (A) Representative acetylated ALPHA-TUBULIN (AC-TUB) recordings of control C3.1, mild- P1.1, moderate- P1.2 and severe P5.1 patient derived organoids treated with DMSO or 1nM EpothiloneD. (**B**) Quantification of apical and basal AC-TUB strand density in DMSO and EpothiloneD treated control C3.1 (N=9), control C4.1 (N=9), mild P1.1 (N=9), mild P2.2 (N=9), moderate P3.2 (N=9), severe P5.1 (N=9), severe P6.1 (N=9) and severe P7.1 (N=9) LIS1-patient derived organoids at day 15. (**C**) Representative N-CADHERIN (N-CAD) recordings of control C3.1, mild P1.1, moderate P3.2 and severe P5.1 LIS1-patient derived organoids treated with DMSO or 1nM EpothiloneD. (**D**) Quantification of N-CAD diameter expansion in DMSO and EpothiloneD treated control C3.1 (N=10), control C4.1 (N=10), mild LIS1-patient P1.1 (N=10), mild LIS1-patient P2.2 (N=10), moderate LIS1-patient P3.2 (n=6), severe LIS1-patient P5.1 (N=6), severe LIS1-patient P6.1 (N=6) and severe LIS1-patient P7.1 (N=6) patient derived organoids at day 15. Scale bars (A) 200 µm, (A, C) 20 µm. Error bars, ±SD. *p < 0.05, **p < 0.01, ***p < 0.001.

Moreover, the recue effect on VZ structure cellular organization resulted in a much more clear and homogeneous generation of neuroepithelial loop structures and a marked decrease neuronal belt surrounding the structures (Figure 22 A). When quantitatively assessing the neuroepithelial structures following EpothiloneD treatment with the developed VZ structure dimension quantification protocol, an increase of nearly all VZ parameters in organoids from LIS1-patients was observed (Figure 22 B). Organoids from patients with severe disease exhibited a most significant enlargement of VZ structures in nearly all parameters most drastic for the VZ diameter. Organoids derived from mild and moderate disease show significant differences to the DMSO control in individual parameters while none of the parameters were significantly altered in control-derived organoids (Figure 22 B). Nonetheless, Epothilone D treatment was not sufficient to fully diminish the observed phenotypic alterations in LIS1-patient derived organoids, especially not in those derived from patients with severe disease. Consequently, I hypothesized that additional pathomechanisms had to play into disease pathology.

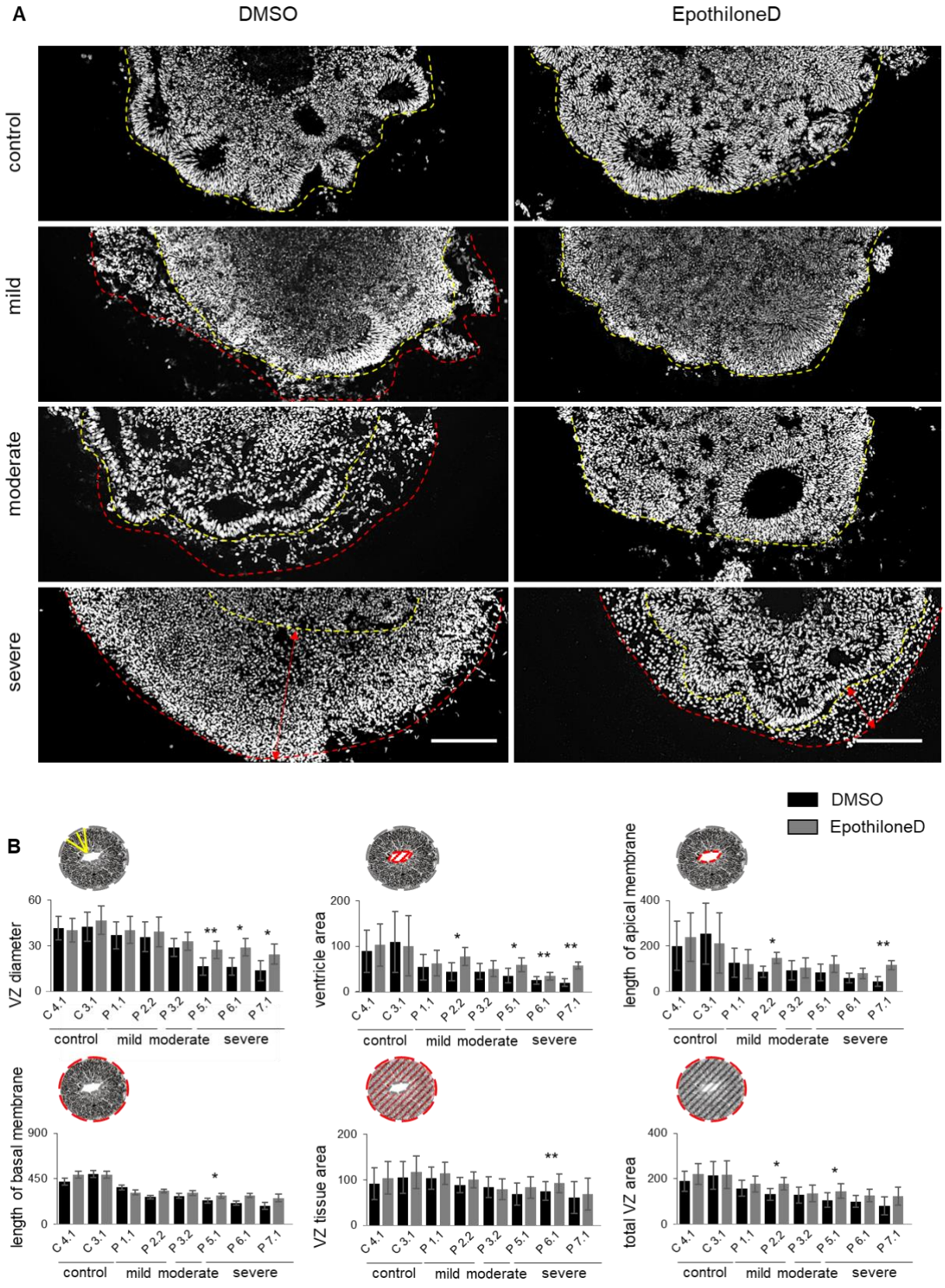
A
DMSO
EpothiloneD
control
mild
moderate
severe
B
DMSO
EpothiloneD
VZ diameter
ventricle area
length of apical membrane
length of basal membrane
VZ tissue area
total VZ area
C 4.1
C 3.1
P 1.1
P 2.2
P 3.2
P 5.1
P 6.1
P 7.1
control
mild
moderate
severe

Figure 22: Microtubule array stabilization by Epothilone D partially rescues ventricular zone structure dimensions in LIS1-pateint derived organoids. (**A**) Representative DAPI recordings of control C3.1, mild- P1.1, moderate- P1.2 and severe- P1.1 LIS1-patient derived organoids treated with 1nM Epothilone D (EpothiloneD) and DMSO control. (**B**) Ventricular structure (VZ) parameter quantification of EpothiloneD and DMSO control treated control- C3.1, control- C4.1, mild- P1.1, mild- P2.2, moderate- P3.2, severe- P5.1, severe- P6.1 and severe- P7.1 LIS1-patient- derived organoids at day 15. control C3.1 DMSO N=16, control C3.1 CHIR N=21, control C4.1 DMSO N=10, control C4.1 CHIR N=18, mild P1.1 DMSO N=16, mild P1.1 CHIR N=24, mild P2.2 DMSO N=12, mild P2.2 CHIR N=11, moderate P3.2 DMSO N=14, moderate P3.2 CHIR N=12, severe P5.1 DMSO N=14, severe P5.1 CHIR N=11, severe P5.2 DMSO N=16, severe LIS1-patient P5.2 CHIR N=11, severe P6.1 DMSO N=10, severe P6.1 CHIR N=10, severe P7.1 DMSO N=11, severe P7.1 CHIR N=11. Scale bars (A) 200 µm. Error bars, ±SD. *$p < 0.05$, **$p < 0.01$, ***$p < 0.001$.

My colleagues and me recently reported for MDS that alterations of the cortical cytoarchitecture can lead to non-cell-autonomous disturbance of WNT-signaling (Iefremova et al. 2017). Thus, I next questioned whether WNT-signaling might be also impacted in the LIS1-patient derived organoids.

4.7. Only Organoids derived from LIS1-patients with severe disease display a non-random aRG cell division switch due to niche-dependent WNT-signaling alterations

WNT-signaling is a major choirmaster during corticogenesis. During forebrain development WNT-signaling from the cortical hem is important for the regulation of the expansion and cell-type specification of aRG cells. My colleagues and me recently reported for MDS that alterations of the cortical cytoarchitecture can lead to a non-cell-autonomous disturbance of WNT-signaling (Iefremova et al. 2017). I thus wondered whether WNT-signaling might be also impacted in my LIS1 patient derived organoids. To monitor the onset and localization of WNT-target gene activity in patient and control derived organoids WNT-GFP iPS cell reporter lines were generated (pRRL.sin-18.ppt, Addgene plasmid #14715, Reya et al. 203; for virus generation see 3.3.1; for virus transduction see 3.1.6). The reporter lines expressed GFP under activation of WNT-signaling. The GFP was cloned downstream of a LEF-1/ TCF responsive promotor containing 3 LEF-1/ TCF binding motifs and a TATA box. When WNT-signaling was active in aRG cells LEF-1/ TCF were expressed and activated the expressions of GFP in correlation with WNT-signaling activity. Organoids derived from controls exhibited VZ structures with a strong GFP signal along the apical lining (Figure 23 A). In contrast, the apical lining of VZ-structures from LIS1-lissencephaly patients showed a gradual decrease in WNT-target gene activity with increased disease severity, most significant in organoids derived from severe patients (Figure 23 A, B). These WNT-signaling alterations were only observable within

the VZ structures, close to the apical membrane in patient derived organoids, but not in cells with neuronal morphology outside the VZ structures (Figure 23 A). I further speculated whether the perturbed niche-dependent WNT-signaling results in a premature non-random switch of aRG cell division from progenitor cell expansion to neurogenesis, as previously observed in organoids derived from MDS patients (Iefremova et al. 2017). Co-staining for p-VIM (phosphorylated by CDK 1 during mitosis and located in the nucleus marking all nuclei in the mitotic phase) and TPX 2 (microtubule associated protein that can visualize the mitotic spindle) were performed to analyze aRG cell division (Figure 23 C). When quantifying at least 3 organoid batches, with at least 3 organoids per batch and at least 6-8 VZ structures per organoids, I found a non-random aRG cell switch only in organoids derived from severe disease. Whereas mild and moderate patient organoids exhibited predominantly random arranged mitotic spindles leading to an increase in oblique division planes (Figure 23 D) most likely related to LIS1 and its important role in mitotic spindle orientation (Pawlisz et al. 2008; N. E. Faulkner et al. 2000; Tsai J, Chen Y, Kriegstein A 2005; Yingling et al. 2008).

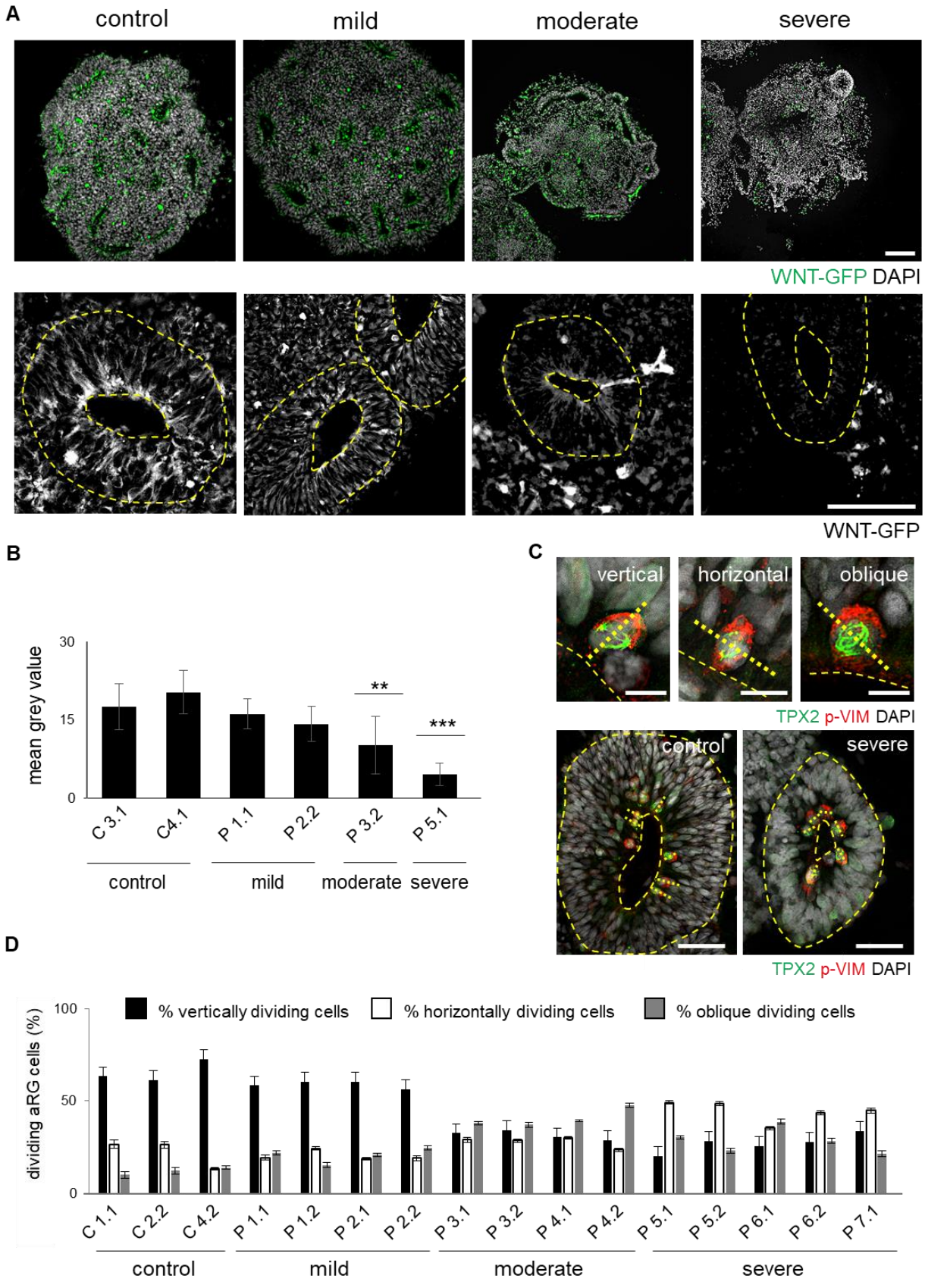
A
control
mild
moderate
severe
WNT-GFP DAPI
WNT-GFP
B
mean grey value
30
15
0
**
***
C 3.1
C4.1
P 1.1
P 2.2
P 3.2
P 5.1
control
mild
moderate
severe
C
vertical
horizontal
oblique
TPX2 p-VIM DAPI
control
severe
TPX2 p-VIM DAPI
D
dividing aRG cells (%)
100
50
0
% vertically dividing cells
% horizontally dividing cells
% oblique dividing cells
C 1.1
C 2.2
C 4.2
P 1.1
P 1.2
P 2.1
P 2.2
P 3.1
P 3.2
P 4.1
P 4.2
P 5.1
P 5.2
P 6.1
P 6.2
P 7.1
control
mild
moderate
severe

Figure 23: Organoids derived from LIS1-patients display niche-dependent WNT-signaling disruption leading to altered aRG cell division specific for the disease condition. (**A**) Representative WNT-GFP recordings of WNT-GFP reporter control C3.1, P1.1 mild- and P5.1 severe LIS1-patient derived organoids at day 20. **(B**) Quantification of mean grey value of WNT-GFP signal in VZ structures (control C3.1 N=10, control C4.1 N=10, mild P1.1 N=10, mild P2.2 N=10, moderate P3.2 N=10, severe P5.1 N=10). (**C**) Representative recordings of vertical-, horizontal and oblique division planes by marking dividing cells with p-VIMENTIN (p-VIMENTIN) and the mitotic spindle by TPX 2 in control- (C4.1) and severe LIS1-patient (P1.1) patient-derived organoids. (**D**) Quantification of orientation of plane of cell division in control and mild LIS1-patient, moderate LIS1-patient and LIS1- severe patient-derived organoids. (control C1.1 N=20, control C2.2 N=20, control C4.2 N=14, mild P1.1 N=15, mild P1.2 N=15, mild P2.1 N=15, mild P2.2 N=11, moderate P1.1 N=11, moderate P1.2 N=9, moderate P2.1 N=10, moderate P2.2 N=13, severe P1.1 N=17, severe P1.2 N=14, severe P2.1 N=9, severe P2.2 N=10, severe P3.1 N=11). Scale bars (A) 50 µm, (B) 10 µm, (C) 20 µm. Error bars, ±SD. *p < 0.05, **p < 0.01, ***p < 0.001.

4.8. GSK3ß inhibition rescues apical radial glia cell division in LIS1-patients with severe disease leading to improved ventricular zone structure dimensions

To test to which extend perturbed niche-dependent WNT-signaling contributes to the observed non-random aRG cell division switch and to the observed phenotypic alterations, control and patient derived organoids were exposed to the GSK3ß inhibitor CHIR99021 (CHIR). CHIR is an aminopyrimidine derivative, which promotes self-renewal of stem cells by promoting symmetric cell divisions by inhibiting GSK-3ß activity and potentiating the upregulation of ß-catenin. In addition, CHIR promotes self-renewal by modulating TGF-ß and upregulating the expression of CYCLIN A. The exposer to CHIR led to a significant rescue of non-random aRG cell division back to proliferative horizontal aRG cell division in severe disease conditions (Figure 24). While the impact of CHIR on control, mild and moderate LIS1-patient aRG cell divisions was insignificant, supporting the assumption of a greater impairment of canonical WNT-signaling in severe conditions.

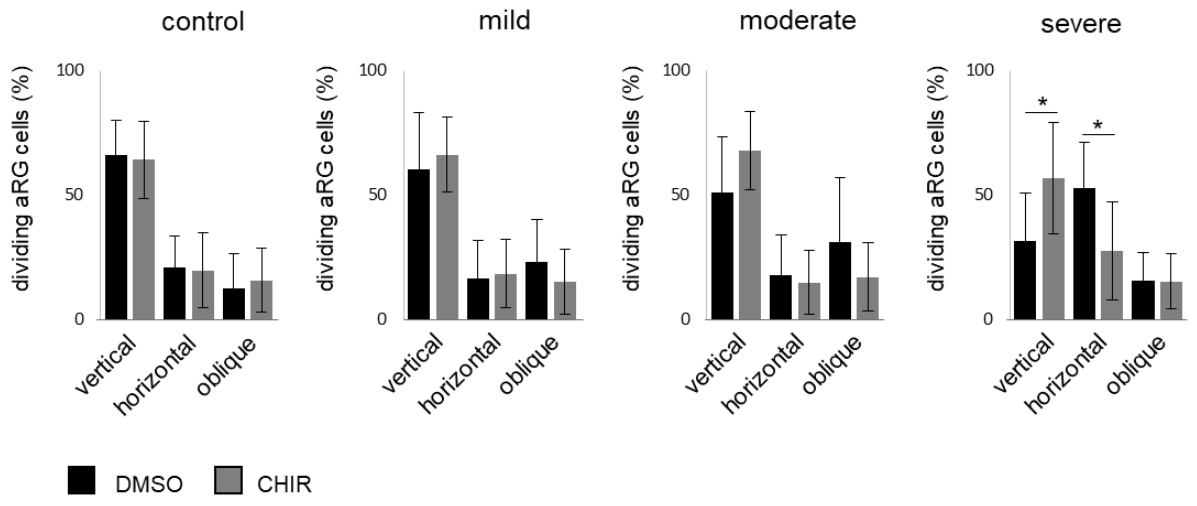

Figure 24: WNT activation changes aRG cell division pattern in iPS cell derived organoids from severe disease. Quantification of vertical, horizontal and oblique division planes of dividing aRG cells in control C3.1 (N=9), mild P1.1 (N=9), moderate P1.2 (N=9) and severe P1.1 (N=9) patient derived organoids in the absence (DMSO) and presence of GSK 3ß inhibitor CHIR at day 15.

The rescue of proliferative aRG cell division led to much more clear and homogeneous generation of VZ-structures compared to the DMSO control (Figure 25 A) with an increase of VZ structure dimensions in all LIS1-patient organoids (Figure 25 B), most likely due to the proliferation enhancing effect of CHIR on aRG cells (C. Li et al. 2013; Pachenari, Kiani, and Javan 2017). In addition, organoids from severe patients exposed to CHIR also exhibited a clearly reduced neuronal belt surrounding the VZ structures (Figure 25 A, indicated by errors).

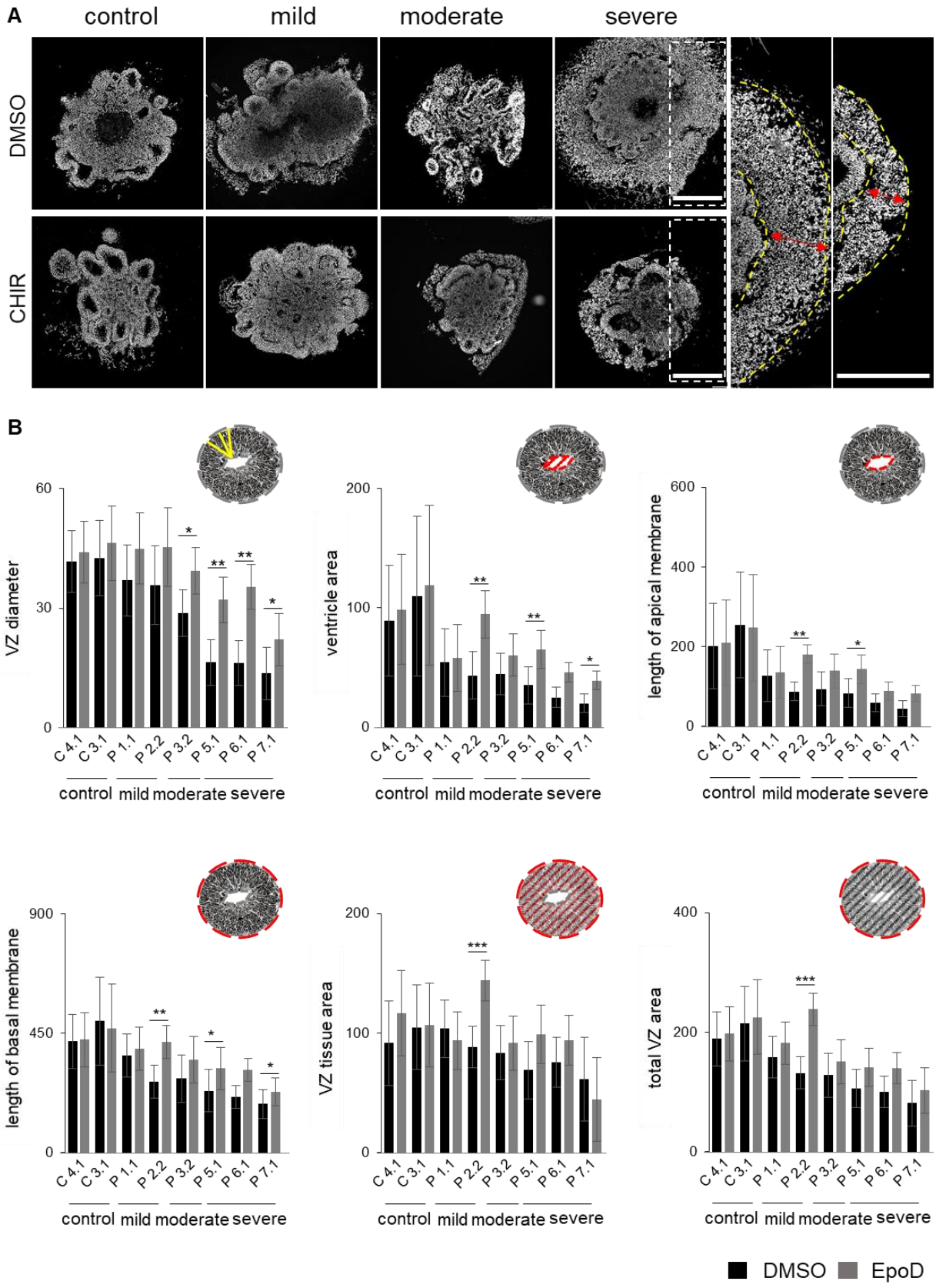
A
control
mild
moderate
severe
DMSO
CHIR
B
VZ diameter
ventricle area
length of apical membrane
length of basal membrane
VZ tissue area
total VZ area
C 4.1
C 3.1
P 1.1
P 2.2
P 3.2
P 5.1
P 6.1
P 7.1
control
mild
moderate
severe
DMSO
EpoD

Figure 25: CHIR treatment-related rescue of aRG cell division orientation improves organoid ventricular zone structure dimensions. (**A, B**) Representative DAPI recordings of control C3.1, mild P1.1, moderate P4.2 and severe P6.1 LIS1-patient derived organoids treated with DMSO or 1 µM CHIR. (**C-H**) Loop parameter quantification of CHIR and DMSO control treated organoids (control C3.1 DMSO N=16, control C3.1 CHIR N=21, control C4.1 DMSO N=10,control C4.1 CHIR N=18, mild P1.1 DMSO N=16, mild P1.1 CHIR N=24, mild 2.2 DMSO N=12, mild P2.2 CHIR N=11, moderate P3.2 DMSO N=14, moderate P3.2 CHIR N=12, severe P5.1 DMSO N=14, severe P5.1 CHIR N=11, severe P5.2 DMSO N=16,severe P5.2 CHIR N=11, severe 2.1 DMSO N=10, severe P6.1 CHIR N=10, severe P7.1 DMSO N=11, severe P7.1 CHIR N=11. Scale bars 200 µm. Error bars, ±SD. *p < 0.05, **p < 0.01, ***p < 0.001.

The aRG cell pool enlargement by CHIR did not lead to an improvement of AC-TUB strand spanning to basal VZ regions (Data not shown), distinctly separating phenotypic alterations directly caused by the disruption of LIS1 microtubule stabilizing function and those alterations, which are indirectly caused by the collapse of cellular organization. The hypothesis is that the different patient-specific mutations in the LIS1 gene have divergent direct impact on microtubule stability, which directly and/or indirectly (WNT-signaling impairments) lead to perturbed human corticogenesis providing the missing link between the patient-specific LIS1 mutation and the clinical severity grade.

5. Discussion

The application of the generated LIS1-lissencephaly iPS cell cohort to the established reproducible forebrain-type organoid protocol (Krefft et al. 2018; Iefremova et al. 2017) and the utilization of the founded quantitative organoid assessment protocols revealed the capability of our organoid system to sensitively reflect different disease severities, a so far not addressed major challenge of the system. In this context, organoids reproduced in correlation with the patient's severity, alterations in organoid cytoarchitecture and premature neurogenesis. Moreover, I showed that the patient-specific mutations have divergent direct impact on LIS1 microtubule stabilizing function, which in turn directly or indirectly leads to perturbed human corticogenesis providing the missing link between the patient-specific LIS1 mutation and the clinical severity grade. The breakdown of cytoarchitectural stability led directly to a progressive cellular disorganization with increasing patient severity, which could in part be rescued by microtubule array stabilization by EpothiloneD. In addition, also indirectly caused niche-depended WNT-signaling alterations played into pathology, most prominent in severe conditions leading to a non-random aRG cell division switch from proliferative to neurogenic cell division. This premature neurogenic division switch explains the observed large belt of neurons around the severe organoids, which was less abundant in milder conditions and mostly absent in controls. Organoid exposer to GSK3ß inhibitor CHIR99021 led to a significant rescue of non-random aRG cell division in severe organoids and to enlarged VZ diameters as well as reduced neurogenesis in all patient derived organoids.

In the following I will discuss how the iPS cell technology opened the doors for *in vitro* disease modeling. The invention of cell reprogramming was a giant milestone for *in vitro* research. The generation of a large LIS1-patient iPS cell cohort reflecting the lissencephalic severity spectrum formed the base for my study and enabled human 3D disease modeling. In the next section, I will discuss in how far my study complemented to the current understanding of LIS1-lissencephly from *in vivo* functional mouse models and human *in vitro* cell culture models. Furthermore, I will discuss potential underlying pathologies for the diverse lissencephalic disease severities and point out to what extend this study contributed to the understanding of disease heterogeneity. In the last sections, I want to reflect whether future application of sensitive patient-specific organoid models can help to identify personalized therapy approaches and also discuss future considerations to improve organoid technology in terms of maturity, complexity as well as functional microenvironments.

5.1. The iPS cell technology – a tremendous milestone for stem cell research

Stem cells have the unique hallmark property of pluripotency facilitating them to self-renewal and differentiate into any body cell (Weissman 2000). In 2007, a tremendous milestone within the field of stem cell research was reached by Takashi and Yamanaka by discovering the reprogramming potential of already differentiated somatic mouse cells by transferring 4 transcription factors (OCT3/4, SOX 2, c-MYC and KLF 4) (Takahashi K, Okita K, Nakagawa M 2007). The translation to human cells in 2008 opened completely new perspectives for regenerative medicine and personalized disease modeling (Takahashi et al. 2007; Yu et al. 2007). The high degree of similarity of iPS and ES cells, significantly diminished the need of ethic-controversial ES cells (Takahashi K, Okita K, Nakagawa M 2007). Moreover, with the advent of defined protocols for the guided differentiation of iPS cells into specific somatic cell types, it became more and more possible to study cell type specific disease progressions. Studies like the one from Rudolf Jaenisch`s labs (Hanna et al. 2007), where sickle cell anemia mice were rescued by treatment with hematopoietic progenitors obtained *in vitro* from autologous iPS cells demonstrate the potential of iPS technology for regenerative medicine approaches. Another example is the progress due to iPS cell approaches to treat Parkinson's disease (Kriks et al. 2012), platelet deficiency (Tsujia et al. 2010) as well as macular degeneration (Okamoto and Takahashi 2011). Due to the advent of iPS cells, we now can generate patient-specific cells and generated diverse target organ-like tissues giving us the potential to unravel human-specific disease mechanisms as well as to identify potential new drug candidates. In the context of my study, the opportunity to model patient-specific disease progression helped to understand individual pathology leading to different disease severities and by that provided the missing link between clinical severity and disease severity.

5.2. Unraveling LIS1-lissencephaly - *in vivo* functional mouse models and *in vitro* human stem cell models

Lissencephaly is most caused by mutation in the LIS1 gene, which was correspondingly the first gene identified to trigger the disorder. With 1,2 cases per 100.000 birth it can be categorized as rare disease. Nonetheless, it is the best studied MCD. Before the emergence of the iPS technology and 3D organoid cell cultures many studies analyzing LIS1-lissencephaly were utilizing murine systems. The basic sequence of events during corticogenesis are commonly shared across species making mouse models a well-suited system to unravel neurodevelopmental disorders. In general, mice can be easily genetically manipulated, making them a powerful tool for examining genetic mechanisms. Consequently, several mouse models

of lissencephaly were created based on LIS1 protein dosage variations leading to the identification of many molecular functions of the LIS1 protein. Even though the observed LIS1-deficiency associated phenotypes appeared milder in murine systems compared to humans most likely due to the low proportion of bRG cells and the related lissencephalic nature of the mouse brain, these murine studies suggest that LIS1 gene dosage is relevant for the phenotypic severities (Y. H. Youn et al. 2009; Gambello, Darling, Yingling, Tanaka, Gleeson, and Wynshaw-Boris 2003). Nonetheless, even so the basic sequence of events during corticogenesis is commonly shared across species, there are existing species differences including developmental timing distinctions of events as well as cell populational variances, which make the translation to human brains challenging. Moreover, why a specific mutation within the LIS1 gene as identified in LIS1-lissencephalic patients leads to different disease severities and whether human-specific processes during cortical development are differentially affected by the specific mutations could not be investigated. Consequently, animal models alone cannot be sufficient to fully understand disease mechanisms and patient-specific disease causing mutations explaining the hysteria when early human brain developmental aspects could be analyzed for the first time *in vitro* (M. Lancaster et al. 2013; Kadoshima et al. 2013). The advent of 3D human cell culture models revolutionized the study of human organ development and disease, it became possible to study human brain development *in vitro*. The development of defined protocols to differentiate iPS cells made it possible to study all human cell types outside the body without harming the living individuum. Within this project I, together with my colleagues, developed a reproductible 3D differentiation protocol leading to highly homogenous forebrain-type brain organoids (Krefft et al. 2018; Iefremova et al. 2017). To implant this protocol for the analysis of patient-specific LIS1-lissencephaly causing mutations I established a LIS1-lissencephalic iPS cell patient cohort by Sendai virus-based reprogramming of fibroblasts and lymphocytes comprising 2 mild, 2 moderate and 3 severe LIS1-patients reflecting the complete lissencephalic severity spectrum. By that I was able to study lissencephalic patient-specific genic backgrounds of living individuals in a dish and approach the question why a specific mutation within the LIS1 gene as identified in LIS1-lissencephalic patients leads to different disease severities and whether human-specific processes during cortical development are differentially affected by the specific mutations. When comparing the generated forebrain-type cerebral organoids from LIS1-patients and 6 age and gender match control iPS cell lines, it became clear that organoids from controls and patients with mild disease gradually develop smooth neuroepithelial loop-like structures which expand over time, whereas organoids from patients with moderate and

severe disease appeared to be generally smaller in size. This observation of size reduction was also made by other studies utilizing 3D brain organoids and modeling the most severe form of lissencephaly, MDS, which is caused by a heterozygous deletion of chromosome 17p13.3 involving LIS1 and YWHAE (coding for 14.3.3 epsilon, a LIS1 interaction partner). Bershteyn and colleagues (Bershteyn et al. 2016) and a former study of my colleagues and me (Iefremova et al. 2017) showed, that organoids derived from MDS patients are drastically smaller in size compared to controls. Interestingly, my organoids from severe LIS1-lissencephaly patients did show a drastic VZ size reduction, but not an overall organoid size decrease. Instead, these organoids were covered by a large belt of neurons, which was drastically less abundant in mild and moderate conditions and nearly absent in control derived organoids. Premature neurogenesis and defective neuronal migration have been described in many different studies analyzing lissencephaly in mouse and human model systems in the past. In mice did the reduction of LIS1 dosage lead to migration defects causing dosage-depended cellular disorganization of cortical layers, hippocampus, cerebellum and olfactory bulb (Hirotsune et al. 1998; Gambello, Darling, Yingling, Tanaka, Gleeson, and Wynshaw-boris 2003; Tanaka et al. 2004). Furthermore, was the necessity of LIS1 for correct neuronal migration also shown by direct examination of neuronal migration in mouse embryonic brain slice cultures, which were *in utero* transfected with green fluorescent protein to label migrating neurons (Shu et al. 2004). Using RNAi knockdown of LIS1 also undoubtfully demonstrated that LIS1 is required of neuronal migration and that LIS1 deficiency leads to neuronal migration defects associated with lissencephaly (Shu et al. 2004; Tsai J, Chen Y, Kriegstein A 2005; Y. H. Youn et al. 2009). With the development of the iPS cell technology the neuronal migration problem could also be shown in human cells. During 2D neural differentiation iPS cells undergo morphogenic changes characterized by the formation of so-called neural rosettes, which reflect every early neural tube-like formation by radially organized epithelial cells with apical-basal polarity (Elkabetz et al. 2008; S. Zhang et al. 2001). Bamba et al. (Bamba et al. 2016) utilized 2D neuronal cultures and demonstrated that lissencephaly patient derived neurons display abnormal neurite extensions, impaired migration and deficient neurite formation. Nonetheless, 2D systems have the disadvantage in contrast to 3D systems, that the capacity of cells to differentiate and self-organize into epithelia reminiscing of the embryo is not given. Nonetheless, due to this variety of studies revealing migration defects, LIS1-lissencephaly was long time considered to be an isolated neuronal migration disorder. However, extended mouse studies showed that the underlying disease triggers are characterized by a broader spectrum of disease-causing pathology also including progenitor abnormalities like mitotic spindle formation as well as

perturbed radial glial cell proliferation (Tsai J, Chen Y, Kriegstein A 2005; Tanaka et al. 2004; N. E. Faulkner et al. 2000; Yingling et al. 2008). To assess the direct consequences of the patient-specific LIS1 mutations on LIS1 microtubule stabilizing function I applied my 3D organoid models to my LIS1-patient cohort and investigated the stability of the cytoskeleton of aRG cells within the 3D VZ cortical loop-like structures by AC-TUB staining. To avoid cutting artifacts, I analyzed cleared and sliced organoids and found an overall reduction of AC-TUB positive labeled tubulin strands with increased disease severity. The more drastic the disease severity was, the more extreme was the cytoskeleton malformed. In addition, in correlation with the degree of astral tubulin disruption, I also observed a cellular disorganization. Especially the organoids derived from moderate and severe disease displayed random arranged cell bodies with gaps in between cells, whereas in control conditions aRG cells arranged well organized, stringed and densely packed within the VZ. Together with this cellular disorganization I identified a disturbed apical membrane alignment. Similar observations of cellular disorganization Bershteyn et al. (Bershteyn et al. 2016) and our laboratory (Iefremova et al. 2017) observed in organoids derived from MDS patients. Furthermore, my colleagues and me found that the apical membrane disruption leads to non-cell-autonomous WNT-signaling disruption leading to a premature, non-random switch from vertical to horizontal cleavage planes of aRG cells, which leads to premature neurogenesis (Iefremova et al. 2017). These findings support the proposed model by Yingling et al. (Yingling et al. 2008) of spindle disorientation due to LIS1 deficiency in RG cells. As underling mechanisms, they found a perturbed DYNEIN localization due to LIS1 deficiency. Comparable to our study, additionally supporting Yingling et al. (Yingling et al. 2008) proposal, Bershteyn et al. (Bershteyn et al. 2016) also described an increase in horizontal cell division associated with a premature shift to neurogenesis in MDS derived cerebral organoids. Interestingly, when investigating aRG cell division modes in my LIS1-patient derived organoids, I found a clear increase in horizontal division patterns only in cultures derived from severe patients compared to controls, explaining the large neuronal belt around organoids from severe disease. Whereas mild and moderate patient organoids exhibited predominantly random arranged mitotic spindles leading to an increase in oblique division planes most likely related to LIS1 and its important role in mitotic spindle orientation (Pawlisz et al. 2008; N. E. Faulkner et al. 2000; Tsai J, Chen Y, Kriegstein A 2005; Yingling et al. 2008). In this context, further investigations analyzing DYNEIN dynamics in the LIS1- patient derived organoids need to be done. To test to what extend perturbed niche-dependent WNT-signaling contributes to the observed phenotypic changes in LIS1-patient derived organoids I exposed control and patient derived organoids to the GSK3ß

inhibitor CHIR99021, which led to much more clear and homogeneous generation of VZ-structures compared to the DMSO control with a significant increase in VZ diameter in organoids derived from moderate and severe patients. In addition, organoids from severe patients exposed to CHIR also exhibit a clearly reduced neuronal belt surrounding the VZ structures and a significant rescue of the perturbed division mode. Concluded, it can be assumed that LIS1-disfunction leads directly to cytoskeleton breakdown, which in turn promotes cellular disorganization associated with apical membrane disruption leading to niche disintegration, which in turn might cause indirectly WNT-signaling alterations. This interplay of LIS1-function-associated direct and indirect pathologies might explain why CHIR only partially rescues observed phenotypes. In addition to add is, that the utilization of MDS-organoids also revealed a mitotic delay of the human-specific bRG cells at later stages (Bershteyn et al. 2016). This human-specific cell type disease phenotype could be shown for the first time, due to the application of human model systems adding to the already unraveled knowledge about LIS1-lissencephaly in murine systems. In my LIS1-patient derived organoids I observed a specific increase in the abundance of cells positive for human-specific bRG marker genes at day 58+/-2 of organoid differentiation, which was most prominent in organoids derived from patients with moderate and severe disease. In addition, I also identified a decrease of cells positive for deep cortical layer marker and an increase of upper cortical layer marker with increase patient severity. Together, these data suggest a premature development of bRG cells accompanied by an accelerated generation of upper cortical layer neurons with increased LIS1-patient severity leading to the hypothesis that LIS1 might be involved in the development of human-specific bRG cell development. One more study is to mention in terms of analyzing human-specific disease parameters of LIS1-lissendephaly facilitating human *in vitro* 3D organoids. Orly and her laboratory (Karzbrun et al. 2018) were able to evaluate human explicit gyrification-like processes unraveling that decreased brain folding observed in LIS1-patients might partially result from differences in the physical properties of progenitor cells. To do so, they generated LIS1 mutant iPS cell lines and defined physical forces that regulate cortical fording. LIS1 mutant organoids display reduced folding properties and a longer distance between folds when compared to wildtype organoid wrinkles. Moreover, they identified a reduction in the speed of nuclear migration from the outer to the inner fold surface, which could be endorsed to the cytoplasmic DYNEIN function. In addition, they found that the LIS1 mutant nuclei do not expand that drastically in the outer fold regions as wildtype nuclei do, resulting in a reduced differential expansion, coherent with the decreased wrinkles. Atomic force microscopy suggested that the LIS1 mutant cells display reduced elasticity. This study also shows the

capability of human *in vitro* systems to complement to the existing knowledge gained by animal models. Moreover, my work clearly demonstrate that organoids are applicable for the analyzes of different disease severities also including mild conditions, a so far not addressed challenge of the system. Former studies modeled most severe lissencephalic conditions (Iefremova et al. 2017; Bershteyn et al. 2016). Furthermore, this study could, for the first time show that lissencephalic conditions can be in part rescued by microtubule-array stabilization, thereby identifying a potential drug to counteract disease progression (see 5.4).

In summary, human brain organoid studies reproduced findings observed in murine systems and in addition strongly suggest, that the pathophysiology of lissencephaly is more complex than previously thought. It might be assumed that the smooth mouse brain without the high number of proliferative bRG cells misses human-specific features to reflect full disease severity. Nonetheless, transgenic mice serve as powerful tool to unravel disease mechanisms caused by the dysfunction of single genes. However, to analyze specific mutation within the LIS1 gene as identified in LIS1-lissencephalic patients human *in vitro* model systems are needed. Cerebral organoids opened up the possibility to study human organ developmental aspects outside the human body, which holds massive potential for the understanding of human-specific disease pathology. This project aimed to shed light on the question why specific mutations within the LIS1 gene as identified in LIS1-lissencephalic patients leads to different disease severities and whether human-specific processes during cortical development are differentially affected by the specific mutations.

5.3. Elucidating underlying pathology of the diverse LIS1-severities – LIS1 function, genetics, environmental factors and by-chance effects

In the previous sections I specified and discussed how this project could complement to the current understanding of LIS1-lissencephaly by putting the findings in the context of former studies utilizing mouse and human model systems. This chapter focuses on how far this project could complement to the understanding of the underlying pathology of the different LIS1-severities. Multiple publications describe that there is no correlation between mutation and severity. Neither the mutation type nor the location of the mutation were found to predict the severity grade of LIS1-lissencephaly (Saillour et al. 2009; Uyanik et al. 2007; Philbert et al. 2017; Pilz et al. 1998). There are known cases, were the same mutation leads to different disease severities (oral communication, Nadja Bahi-Buisson). That raises the question in how far the genetic plays into pathology. Are environmental factors or any by-chance effects involved or is it mainly the degree of LIS1-function disruption which determines severity? My data clearly

points out a direct relationship between LIS1-lissencephalic severity and LIS1-function-associated cellular disruption. The more severe the disease the more drastic the LIS1-associated phenotypes like cytoskeleton breakdown, cellular disorganization, and apical membrane disruption in LIS1-patient derived organoids. Also, the WNT signaling impairment seems to be indirectly correlated with LIS1-function-associated apical membrane disruption caused by cellular disorganization triggered by cytoskeleton breakdown. The fact, that the severity can be mirrored with brain organoids excludes environmental factors playing into disease diversity as those are not present in my organoid models. Here, I only had access to 2 patients harboring the same mutation and suffering from the same disease severity. It would be interesting to generate organoids from patient cells with the same mutation and different disease severities to shed even more light on disease heterogeneity. Initially, one publication suggested a putative correlation with the mild lissencephaly associated missense mutations and truncating mutations localized at the 3' end of the LIS1 gene (Cardoso et al. 2000). Although more recent studies did not confirm this relationship (Uyanik et al. 2007; Saillour et al. 2009). Saillour et al. (Saillour et al. 2009) analyzed a large LIS1-patient cohort including 40 patients carrying LIS1 mutations (75%) or small deletions (20%). They tried unsuccessfully to correlate the severity of the disease in terms of epileptic seizures, radiological findings, and body movement impairments with the LIS1 mutations. Moreover, Uyanik et al. (Uyanik et al. 2007) revealed 21 intragenic mutations distributed over the entire LIS1 gene. Except 2 mutations in the LIS1 homology domain and 2 in the region encoding the coiled-coil domain all were found in one of the seven WD40 repeat domains. Similar, also the mutations of the patients included in my study are localized within this WD40 repeat regions. But neither the type nor the position of the mutation correlated with a particular phenotype. Rather, they found that the clinical severity correlates only with the degree of agyria and cortical thickening, which supports the statement of Barkovich and colleagues already in 1991 (Barkovich, Koch, and Carrol 1991). In addition, also my study supports this observation. The more severe the brain folding's alterations of the LIS1-patients, the more severe the clinical severity was of the here included patients. In addition, my study shows a strong correlation between clinical severity with the LIS1-function associated phenotypic alterations found in my LIS1-lissencepahly organoid models. My data hints towards the hypothesis that the degree of impairment of LIS1 function directly or indirectly (WNT-signaling) determines disease severity. The next logical question in line would be what determines the degree of impairment of LIS1 function? In line with the studies discussed above (Uyanik et al. 2007; Saillour et al. 2009) I also did not see a correlation to the mutations. The patients characterized by mild disease, grade 4-5, carry the same recurrent

mutation affecting a splice site (c.569-10T>C; LIS1-mild P1 und P2) leading to exon 7 skipping with an induced frameshift. The patients with moderate disease display either a small deletion (c.11delC, LIS1-moderate P3) leading to frameshift or a deletion of exon 11. The mutations leading to severe phenotypes, grade 1-2, have either a mutation leading to skipping of exon 9 which is in-frame (c.1002+1G>T, LIS1-severe P5), or missense mutations (c.531G>C, LIS1-severe P6; c.445C>T, LIS1-severe P7 ;). Concluded, the less severe mutation lead to severe disease, whereas the milder mutation lead to mild disease progressions. Our collaboration partners analyzed the impact of 4 specific mutations on LIS1 protein synthesis (Philbert et al. 2017). They examined LIS1 mRNA levels of fibroblasts from mild LIS1-patient P1 and P2 (c.569-10T>C) as well as from severe LIS1-patient P5 (c.1002+1G>T) and P7 (c.445C>T). Quantitative real-time qPCR showed that WT transcript levels from those 4 patients (mild and severe) are reduced by approximately half compared to controls due to the heterozygous mutation. But only the mutant transcripts levels from patients with mild disease (P1 and P2) carrying a frameshift are degraded by NMD, as shown by inhibition of NMD by Emetine. In contrast, mutant transcripts of patients with severe disease (P5 and P7), with in-frame missense mutation, are not degraded. Inhibition of the proteasome led to LIS1 clusters only in cells from patients P5 and P7 with severe disease severe. Cells from patients P1 and P2 did not show this phenomenon supporting the assumption that only cells from severe patients contain misfolded protein variants. Due to co-labeling of LIS1 and G3BP1, an SG marker, and fibroblast treatment with sodium arsenate, a cellular stressor, they found that LIS1 clusters are observed only after MG132 treatment, suggesting LIS1 mutant proteins are misfolded and then degraded by proteasome. These findings suggest that the wildtype transcript reduction by 50 % together with the 50 % of misfolded proteins are more harmful to the cell physiology than only the 50 % wildtype transcripts as found in cells from patients with mild disease, which might be associated with SG formation. The degradation by the proteasome seems to lead to more severe clinical symptoms, although by-chance effects are not ruled out. It would be interesting to further analyze SG formation in human 3D cortical organoids. One hypothesis could be, that the misfolded LIS1 proteins, which according to Philbert et al. (Philbert et al. 2017, Camille Maillard unpublished data) only appear in cells from patients with severe disease might negatively influence the complex interaction network of LIS1, explaining the direct correlation of disease severity and LIS1-disfunction-associated cellular disruption as observed in my LIS1-organoid models.

My data could show that different patient-specific mutations in the LIS1 gene have divergent direct impact on microtubule stability, which directly and/or indirectly lead to perturb human

corticogenesis providing the missing link between the patient-specific LIS1 mutation and the clinical severity grade. The application of this sensitive model allows the analyzes of disease severity specific pathomechanisms. In the next section it is discussed in how far the application of those sensitive *in vitro* models can elevate personalized medicine and may lead to a better understanding of individual disease progression for effective therapy.

5.4. Patient derived organoids – unraveling individual disease progressions for the identification of personalized drug treatments

This chapter discusses whether patient-specific organoid approaches can lead to an understanding of patient-specific disease progression as well as to the identification of personalized drug interventions. Even though 3D organoid cultures are young scientific tools, they already have been used to identify possible drug targets (Nowakowski, et al. 2017) and therapeutic application against ZIKA virus infection (Li et al., 2017). Nonetheless, there are no published studies, which test the sensitivity of 3D systems to recapitulate different disease severities and understand individual's disease progressions. My pioneer work raises hope that organoids can really unravel patient-specific disease progression and support personalized medicine approaches. The observed phenotypic differences correlated with patient disease severity. Moreover, the patient-specific disease severity modeling led to the identification of dissimilar degree of impact of specific pathways involved. In the mild and moderate LIS1-patient derived organoids aRG cells displayed dominantly a non-planar random disorientation of mitotic spindle, which might be explained by LIS1-deficiency associated with DYNEIN delocalization (Yingling et al. 2008). Whereas, in the severe LIS1-patient organoids a planar switch from vertical to horizontal aRG cell division was most prominent, which might be associated with N-CAD disruption and disturbance of ß-CAT/WNT-signaling (Iefremova et al. 2017). Adherents junctions have been associated with self-renewal control of aRG cells (Marthiens et al. 2010; Stocker and Chenn 2009). Moreover, data from mouse studies indicate that WNT/ß-CAT signaling is crucial for aRG cell proliferation (Chenn and Walsh 2008; Zechner et al. 2003) and that N-CAD is involved in WNT activity by controlling AKT phosphorylation, which in turn leads to phosphorylation and stabilization of ß-CAT (J. Zhang et al. 2010, 2013). Consequently, the protein level of important signaling proteins within the WNT-signaling cascade as well as their phosphorylated forms were analyzed in the different LIS1-patient lines (Data not shown). Despite a potential reduction of LRP 5/6 receptor in the severe LIS1-patient derived cells were no specific abnormalities detected. Nonetheless, based on the observed N-CAD/ WNT-signaling disruption the GSK 3b inhibitor CHIR was tested to

counteract observed phenotypes and indeed, the treatment rescued aRG vertical cell division planes in LIS1-patient derived organoids and consequently significantly decreased premature neurogenesis and increased cortical-like ventricular structure size. These findings go in line with former studies (Iefremova et al. 2017; Zechner et al. 2003; J. Zhang et al. 2013). The rescue effect specific for severe conditions confirmed the greater impact of LIS1-assocaited spindle disorientation rather than WNT-signaling disruption in the milder conditions. To counteract those LIS1-associated microtubule-destabilization triggered phenotypes, a second drug screen was performed testing the microtubule-stabilizing drug EpothiloneD, which is a macrolide compound binding to a common binding site on ß-tubulin (Giannakakou et al. 2000). Based on the applied concentration EpothiloneD can stabilize microtubes (low dosages) or block cell division by completely preventing microtubule depolymerization (high dosage) (Bollag et al. 1995). Applying higher dosages, EpothiloneD has been successful tested for hindering malign cell division and is currently subjected to clinical trials. For detailed information of EpothiloneD in cancer treatment see Fumoleau et al. (Fumoleau et al. 2007). In very low concentrations EpothiloneD has been applied to studies focusing on tauopathy-associated disorders utilizing mouse models (B. Zhang et al. 2012; Cartelli et al. 2013; Penazzi et al. 2016). EpothiloneD treatment in aged tau transgenic mice with Alzheimer-like tau pathology and related behavioral deficits reduced axonal dystrophy and increased axonal microtubule density, which led to improved fast axonal transport and cognitive performance (B. Zhang et al. 2012). Also, Cartelli et al. (Cartelli et al. 2013) described the neuroprotective effect of EpothiloneD on mice mimicking experimental parkinsonism induced by 1-methyl-4-phenyl-1,2,3,6-tetrahydropyridine (MPTP). Consequently, low-dosage EpothiloneD treatment was also tested on the LIS1-patient derived organoids. The experiments confirmed the microtubule-stabilizing properties of EpothiloneD displaying significant improvement in cytoarchitectural stability by astral tubulin strands spanning in VZ basal regions. This rescue of VZ architectural stability led to improved cellular organization. In summary, the discovery of severity-specific pathologies as well as the identification of specific drugs differential rescuing phenotypic alterations in mild, moderate and severe LIS1-patient derived organoids underlines the capacity of iPS cell derived 3D model systems to understand individual disease progressions. Consequently, brain organoids are a very promising tool for personalized disease understanding as well as patient-specific therapeutically intervention approaches. Nonetheless, the field remains young and there is capacity for further enhancement before it reliably can serve as robust model for therapy and regenerative medicine. The following chapter discusses possible improvements, which could enhance *in vivo* similarity and reduce system limitations.

5.5. Brain organoids – future advances of complexity, maturity and functionality

The here presented work displays that the organoid system serves as promising model to analyze human and severity-specific aspects of LIS1-associated MCD as well as related disorders and contributes to the identification of new therapeutic drugs. There are multiple studies verifying the capability of organoids to develop specific and discrete brain regions closely mimicking *in vivo* cell type compositions with gene expression profiles and epigenetic signatures reminiscing of human fetal corticogenesis (Kanton et al. 2019; Velasco et al. 2019; Quadrato et al. 2017; Camp et al. 2015). Nonetheless, they remain immature in nature only reflecting developmental processes of the first and second gestation semester. To make the organoid system mature, there are significant challenges and limitations to overcome especially in terms of complexity and maturity. It is undeniable that brain organoid systems have progressed substantially due to the development of diverse generation protocols closely mimicking *in vivo* development (M. a Lancaster et al. 2013; M. A. Lancaster et al. 2017; Kadoshima et al. 2013; Birey et al. 2017; X. Qian et al. 2016; Krefft et al. 2018). Depending on the differentiation protocol organoids differentiate spontaneously (without external morphogen supplementation) in an unpredictable fashion into brain regions of different identity (M. Lancaster et al. 2013) or with growth factor manipulation into regional specified homogenous brain tissue (Birey et al. 2017; Xuyu Qian et al. 2016; Kadoshima et al. 2013)(for review see Marsoner, Koch, and Ladewig 2018). Both differentiation approaches generate organoids, which face the limitation of missing tissue polarity without topographic organization illustrating that organoids are still a very reductionist model without body axes and morphogen signaling centers leading to the absence of morphogen gradients within the tissue. This limitation has been tackled by multiple studies with different approaches. One approach is based on the guided differentiation of organoids into specific brain identities with subsequent fusion of those different regions (Bagley et al. 2017; Xiang et al. 2017). This approach does, however, not recapitulate the continuum of regional diversity found in the human brain (Krefft, Koch, Ladewig, in press by SDCB). Cederquist and colleagues (Cederquist et al. 2019) attempted to overcome the weakness of missing topographic organization by the implementation of morphogen-secreting cells, mimicking organizing centers, into the organoid tissue. Similar, also Orly Reiners laboratory (Karzbrun et al. 2018) tried to establish morphogen gradients by external selective morphogen exposure by microfluidic systems. All studies helped to direct organoid technologies into an advanced future, but still did not manage to develop topographic organized *in vitro* tissue. Another big limitation of organoids is the missing non-neuroectodermal structures including blood vessel, meninges as well as cerebrospinal fluid.

Meninges have not only a brain protective role, but also establish unique microsystem for cellular waste disposal of the brain. In addition, they provide entry for blood vessel into the brain tissue. The in organoid present lumen do not contain physiological equivalent to blood (Wimmer et al. 2019) or cerebrospinal fluid (Kadoshima et al. 2013) limiting the nutritive supply of cells deep insight the tissue as well as the presence of signaling molecules for tissue polarity. Finally, to mention is the limitation of immune and glia cells. Studies coculturing organoids with microglia have started to approach this limitation (Ormel et al. 2018; Song et al. 2019) but further studies are needed to investigate the contribution of microglia in organoid tissue with respect to their role in developmental processes like synaptic pruning. Also, astrocytes and oligodendrocytes, which are important for synaptogenesis as well as myelination, are underrepresented in organoid cultures (Quadrato et al. 2017), probably due to the limited culture time of 3D organoids. Despite cell populational deficits, cytoarchitectural aspects of organoids also need to be critically reflected. The in human significantly enlarged and in inner and outer separated SVZ can be found in organoids, although in a limited extend (Watanabe et al. 2016). The same does account for the 6 cortical layers. Layer-related cell types can be detected in organoids, but only fragmentary without the distinct layer-specific orientation (Bhaduri et al. 2020). The folding of the outer cortical layers leads to the primate-specific gyrification of the neocortex. Although organoids display wrinkles, it cannot be equated with gyri and sulci in human brains. The reported folding due to physical forces (Karzbrun et al. 2018) or genetic manipulation (Y. Li et al. 2019) mainly involves the inner germinal zone and not the outer layers of the cortex as it is true for gyrification (Lewitus, Kelava, and Huttner 2013).

It remains elusive to what extent mature aspects of brain development can be achieved in organoid cultures. It is likely that there is a natural limitation of *in vitro* cultures to reproduce the incredible complexity of the human brain in a dish. Consequently, organoid data needs to be carefully evaluated with respect to the impact of the systems limitations.

6. Conclusion

The here presented work demonstrates the great potential of recent technology advances including iPS cell- as well as organoid tools to revolutionize stem cell research and medicine. Impressively, human organ development can be analyzed outside the human body with healthy and patient-specific disease backgrounds. These advents open completely new perceptive for personalized medicine. The here demonstrated research underlines the capability of cerebral organoids to sensitively model individual disease severities, a so far not addressed major challenge of the system. My data show that different patient-specific mutations in the LIS1 gene have divergent direct impact on microtubule stability, which directly and/or indirectly lead to perturbed human corticogenesis providing the missing link between the patient-specific LIS1 mutation and the clinical severity grade. Future applications analyzing individual diseases have the potential to advance personalized medicine and improve the understanding of individual pathology for personalized therapy. Nonetheless, intensive research still needs to overcome hurdles focusing on organoid complexity, maturity as well as functional microenvironments to faithfully model *in vivo* development. By accomplishing following aims this thesis demonstrated for the first time that 3D organoids already serve as promising tool to reflect different disease severities and to elucidate individual disease pathology:

1. A large LIS1-patient iPS cell cohort reflecting the complete severity spectrum of LIS1-lissencephaly was generated and fully characterized.
2. An *in vitro* system to reconstruct cortical stem cell niche and analyze corticogenesis in healthy and patient-specific disease backgrounds was established.
3. The sensitivity of organoid systems to model patient-specific disease progressions was shown.
4. LIS1-associated phenotypes reflecting the individual LIS1-patient’s severity were unraveled.
5. Potential severity-specific disease mechanisms were found, which are directly or indirectly caused by the impairment of LIS1 microtubule stabilizing functions.
6. 2 potential drugs were identified, which counteracted specific mechanisms involved in LIS1-lissencephaly pathology.

References

Aberle, Hermann, Andreas Bauer, Andreas Kispert, and Rolf Kemler. 1997. "β-Catenin Is a Target for the Ubiquitin–Proteasome Pathway." *The EMBO Journal* 16 (13): 3797–3804.

Aronica, Eleonora, Albert J., Becker, and Roberto, Spreafico. 2012. "Malformations of Cortical Development." *Brain Pathology* 22: 380–401. https://doi.org/10.1111/j.1750-3639.2012.00581.x.

Bagley, Joshua A., Daniel Reumann, Shan Bian, Julie Lévi-Strauss, and Juergen A. Knoblich. 2017. "Fused Dorsal-Ventral Cerebral Organoids Model Complex Interactions between Diverse Brain Regions." *Nature Methods* 14 (7): 743–51. https://doi.org/10.1038/nmeth.4304.

Bamba, Yohei, Tomoko Shofuda, Mitsuhiro Kato, Ritsuko K. Pooh, Yoko Tateishi, Jun-ichi Takanashi, Hidetsuna Utsunomiya, et al. 2016. "In Vitro Characterization of Neurite Extension Using Induced Pluripotent Stem Cells Derived from Lissencephaly Patients with TUBA1A Missense Mutations." *Molecular Brain*, 1–14. https://doi.org/10.1186/s13041-016-0246-y.

Barkovich, A. James, Renzo Guerrini, Ruben I. Kuzniecky, Graeme D. Jackson, and William B. Dobyns. 2005. "A Developmental and Genetic Classification for Malformations of Cortical Development." *Neurology*. https://doi.org/10.1212/01.wnl.0000183747.05269.2d.

Barkovich, A. James, Thomas K. Koch, and Clark L. Carrol. 1991. "The Spectrum of Lissencephaly: Report of Ten Patients Analyzed by Magnetic Resonance Imaging." *Annals of Neurology* 30 (2): 139–46. https://doi.org/10.1002/ana.410300204.

Barkovich James A., Ruben I. Kuzniecky, William B. Dobyns, Graeme D. Jackson, Becker L.E. and Evrard P. 1996. "A Classification Scheme for Malformations of Cortical Development." *Neuropediatrics*, no. 27: 59–63. https://doi.org/10.1093/brain/aws019.

Barkovich, A James, Renzo Guerrini, Ruben I Kuzniecky, Graeme D Jackson, and William B Dobyns. 2012b. "A Developmental and Genetic Classification for Malformations of Cortical Development : Update 2012." *Brain*. https://doi.org/10.1093/brain/aws019.

Bershteyn, Martina, Thomasz J. Nowakowski, Alex Pollen, Elizabeth Di Lullo, Aishwarya Nene, Anthony Wynshaw-Boris, and Arnold R. Kriegstein. 2016. "Human IPSC-Derived Cerebral Organoids Model Cellular Features of Lissencephaly and Reveal Prolonged Mitosis of Outer Radial Glia." *Cell Stem Cell* 420 (4): 199–209. https://doi.org/10.1016/j.ydbio.2016.06.037.

Bhaduri, Aparna, Madeline G. Andrews, Walter Mancia Leon, Diane Jung, David Shin, Denise

Allen, Dana Jung, et al. 2020. “Cell Stress in Cortical Organoids Impairs Molecular Subtype Specification.” *Nature* 578 (7793): 142–48. https://doi.org/10.1038/s41586-020-1962-0.

Birey, Fikri, Jimena Andersen, Christopher D. Makinson, Saiful Islam, Wu Wei, Nina Huber, H. Christina Fan, et al. 2017. “Assembly of Functionally Integrated Human Forebrain Spheroids.” *Nature* 545 (7652): 54–59. https://doi.org/10.1038/nature22330.

Bizzotto, Sara, and Fiona Francis. 2015. “Morphological and Functional Aspects of Progenitors Perturbed in Cortical Malformations.” *Frontiers in Cellular Neuroscience* 9 (February): 1–25. https://doi.org/10.3389/fncel.2015.00030.

Bollag, Daniel M, Patricia A Mcqueney, Jian Zhu, Otto Hensens, Lawrence Koupal, Jerrold Liesch, Michael Goetz, Elias Lazarides, and Catherine M Woods. 1995. “Epothilones , a New Class of Microtubule-Stabilizing Agents with a Taxol-like Mechanism of Action.” *Cancer Research*.

Borrell, Victor. 2019. “Recent Advances in Understanding Neocortical Development.” *F1000Research* 8: 1–9. https://doi.org/10.12688/f1000research.20332.1.

Bystron, Irina, Colin Blakemore, and Pasko Rakic. 2008. “Development of the Human Cerebral Cortex: Boulder Committee Revisited.” *Nature Reviews Neuroscience* 9 (2): 110–22. https://doi.org/10.1038/nrn2252.

Camp, J. Gray, Farhath Badsha, Marta Florio, Sabina Kanton, Tobias Gerber, Michaela Wilsch-Bräuninger, Eric Lewitus, et al. 2015. “Human Cerebral Organoids Recapitulate Gene Expression Programs of Fetal Neocortex Development.” *Proceedings of the National Academy of Sciences* 112 (51): 201520760. https://doi.org/10.1073/pnas.1520760112.

Cardoso, Carlos, Richard J. Leventer, NaomichiMatsumoto, Julie A. Kuc, Melissa B. Ramocki, Stephanie K. Mewborn, Laura L. Dudlicek, et al. 2000. “The Location and Type of Mutation Predict Malformation Severity in Isolated Lissencephaly Caused by Abnormalities within the LIS1 Gene.” *Human Molecular Genetics* 9 (20): 3019–28. https://doi.org/10.1093/hmg/9.20.3019.

Cartelli, Daniele, Francesca Casagrande, Carla Letizia Busceti, Domenico Bucci, Gemma Molinaro, Anna Traficante, Daniele Passarella, et al. 2013. “Microtubule Alterations Occur Early in Experimental Parkinsonism and The.” *Scienctific Reports*, 1–10. https://doi.org/10.1038/srep01837.

Caspi, Michal, Frédéric M. Coquelle, Cynthia Koifman, Talia Levy, Hiroyuki Arai, Junken Aoki, Jan R. De Mey, and Orly Reiner. 2003. “LIS1 Missense Mutations. Variable Phenotypes Result from Unpredictable Alterations in Biochemical and Cellular

Properties." *Journal of Biological Chemistry* 278 (40): 38740–48. https://doi.org/10.1074/jbc.M301147200.

Cederquist, Gustav Y, James J Asciolla, Jason Tchieu, Ryan M Walsh, Daniela Cornacchia, Marilyn D Resh, and Lorenz Studer. 2019. "Specification of Positional Identity in Forebrain Organoids." *Nature Biotechnology* 37 (4): 436–44. https://doi.org/10.1038/s41587-019-0085-3.

Chambers Stuart M, Fasano Christopher A, Papapetrou Eirini P, Tomishima Mark, Sadelain Michel, Studer Lorenz. 2009. "Highly Efficient Neural Conversion of Human ES and IPS Cells by Dual Inhibition of SMAD Signaling." *Nat Biotechnol.* 27 (3): 275–80. https://doi.org/10.1038/nbt.1529.Highly.

Chenn, Anjen, and Christopher A. Walsh. 2008. "Regulation of Cerebral Cortical Size by Control of Cell Cycle Exit in Neural Precursors." *Science* 365 (2002): 365–70. https://doi.org/10.1126/science.1074192.

Chevassus-Au-Louis, N., S. C. Baraban, J. L. Gaïarsa, and Y. Ben-Ari. 1999. "Cortical Malformations and Epilepsy: New Insights from Animal Models." *Epilepsia* 40 (7): 811–21. https://doi.org/10.1111/j.1528-1157.1999.tb00786.x.

Chia, Gloryn, Judith Agudo, Nathan Treff, Mark V Sauer, David Billing, Brian D Brown, Richard Baer, and Dieter Egli. 2017. "Genomic Instability during Reprogramming by Nuclear Transfer Is DNA Replication Dependent." *Nature Cell Biology* 19 (4). https://doi.org/10.1038/ncb3485.

Collins, Stephan C., Ana Uzquiano, Mohammed Selloum, Olivia Wendling, Marion Gaborit, Maria Osipenko, Marie Christine Birling, Binnaz Yalcin, and Fiona Francis. 2019. "The Neuroanatomy of Eml1 Knockout Mice, a Model of Subcortical Heterotopia." *Journal of Anatomy* 235 (3): 637–50. https://doi.org/10.1111/joa.13013.

Cugola, Fernanda R., Isabella R. Fernandes, Fabiele B. Russo, Beatriz C. Freitas, Joaõ L.M. Dias, Katia P. Guimarães, Cecília Benazzato, et al. 2016. "The Brazilian Zika Virus Strain Causes Birth Defects in Experimental Models." *Nature* 534 (7606): 267–71. https://doi.org/10.1038/nature18296.

Dang, Jason, Sashi K. Tiwari, Gianluigi Lichinchi, Yue Qin, Veena S. Patil, Alexey M. Eroshkin, and Tariq M. Rana. 2016. "Zika Virus Depletes Neural Progenitors in Human Cerebral Organoids through Activation of the Innate Immune Receptor TLR3." *Cell Stem Cell* 19 (2): 258–65. https://doi.org/10.1016/j.stem.2016.04.014.Zika.

DeSantis, Morgan E., Michael A. Cianfrocco, Zaw Min Htet, Phuoc Tien Tran, Samara L. Reck-Peterson, and Andres E. Leschziner. 2017. "Lis1 Has Two Opposing Modes of

Regulating Cytoplasmic Dynein." *Cell* 170 (6): 1197-1208.e12. https://doi.org/10.1016/j.cell.2017.08.037.

Desikan, Rahul S, and A James Barkovich. 2016. "Malformations of Cortical Development." *Ann Neurol.* 80 (6): 797–810. https://doi.org/10.1002/ana.24793.Malformations.

Dobyns, William B., and C. L. Truwit. 1995. "Lissencephaly and Other Malformations of Cortical Development: 1995 Update." *Neuropediatrics* 26 (3): 132–47. https://doi.org/10.1055/s-2007-979744.

Dobyns, William B., and S Das. 2014. "PAFAH1B1 -Associated Lissencephaly / Subcortical Band Heterotopia," *Gene Reviews* 1–22.

Dobyns, W B, Orly Reiner, Romeo Carrozzo, and H Ledbetter. 1993. "A Human Brain Malformation Associated With Deletion of the LIS1 Gene Located at Chromosome 17p13." *JAMA*. https://doi.org/10.1001/jama.1993.03510230076039.

Efimov, Vladimir P, and N Ronald Morris. 2000. "The LIS1-Related NUDF Protein of Aspergillus Nidulans Interacts with the Coiled-Coil Domain of the NUDE/RO11 Protein." *JCB Reports* 150 (3): 681–88. https://doi.org/10.1083/jcb.150.3.681.

Eiraku, M., K. Watanabe, M. Matsuo-takasaki, M. Kawada, S. Yonemura, M. Matsumura, T. Wataya, A. Nishiyama, K. Muguruma, and Y. Sasai. 2008. "Self-Organized Formation of Polarized Cortical Tissues from ESCs and Its Active Manipulation by Extrinsic Signals." *Cell Stem Cell* 1: 519–32. https://doi.org/10.1016/j.stem.2008.09.002.

Elkabetz, Yechiel, Georgia Panagiotakos, George Al Shamy, Nicholas D. Socci, Viviane Tabar, and Lorenz Studer. 2008. "Human ES Cell-Derived Neural Rosettes Reveal a Functionally Distinct Early Neural Stem Cell Stage." *Genes and Development*, 152–65. https://doi.org/10.1101/gad.1616208.1995.

Faulkner, Nicole E, Denis L Dujardin, Chin-yin Tai, Kevin T Vaughan, Christopher B O Connell, Yu-li Wang, and Richard B Vallee. 2000. "A Role for the Lissencephaly Gene LIS1 in Mitosis and Cytoplasmic Dynein Function." *Nature Cell Biology*. https://doi.org/10.1038/35041020.

Fietz, Simone A, Iva Kelava, Johannes Vogt, Michaela Wilsch-bräuninger, Denise Stenzel, Jennifer L Fish, Denis Corbeil, et al. 2010. "OSVZ Progenitors of Human and Ferret Neocortex Are Epithelial-like and Expand by Integrin Signaling." *Nature Neuroscience* 13 (6). https://doi.org/10.1038/nn.2553.

Fogli, Antonella, Renzo Guerrini, Francesca Moro, Emilio Fernandez-Alvarez, Marie Odile Livet, Alessandra Renieri, Maddalena Cioni, et al. 1999. "Intracellular Levels of the LIS1 Protein Correlate with Clinical and Neuroradiological Findings in Patients with Classical

Lissencephaly." *Annals of Neurology*. https://doi.org/10.1002/1531-8249(199902)45:2.

Francis, Fiona, Gundela Meyer, Catherine Fallet-Bianco, Sarah Moreno, Caroline Kappeler, Alfredo Cabrera Socorro, Françoise Phan Dinh Tuy, Cherif Beldjord, and Jamel Chelly. 2006. "Human Disorders of Cortical Development: From Past to Present." *European Journal of Neuroscience* 23 (4): 877–93. https://doi.org/10.1111/j.1460-9568.2006.04649.x.

Fumoleau, P, B Coudert, N Isambert, and E Ferrant. 2007. "Novel Tubulin-Targeting Agents : Anticancer Activity and Pharmacologic Profile of Epothilones and Related Analogues." *Annals of Oncology* 18 (Supplement 5): 9–15. https://doi.org/10.1093/annonc/mdm173.

Gambello, Michael J., Dawn L. Darling, Jessica Yingling, Teruyuki Tanaka, Joseph G. Gleeson, and Anthony Wynshaw-Boris. 2003. "Multiple Dose-Dependent Effects of Lis1 on Cerebral Cortical Development." *Journal of Neuroscience* 23 (5): 1719–29. https://doi.org/10.1523/jneurosci.23-05-01719.2003.

Gambello, Michael J, Dawn L Darling, Jessica Yingling, Teruyuki Tanaka, Joseph G Gleeson, and Anthony Wynshaw-boris. 2003. "Multiple Dose-Dependent Effects of Lis1 on Cerebral Cortical Development." *The Journal of Neuroscience* 23 (5): 1719–29. https://doi.org/10.1523/JNEUROSCI.23-05-01719.2003.

Garcez, Patricia P, Erick Correia Loiola, Rodrigo Madeiro da Costa, Luiza M. Higa, Pablo Trindade, Rodrigo Delvecchio, Juliana Minardi Nascimento, Rodrigo Brindeiro, Amilcar Tanuri, and Stevens K. Rehen. 2016. "Zika Virus Impairs Growth in Human Neurospheres and Brain Organoids." *Science (New York, N.Y.)* 352 (April): aaf6116. https://doi.org/10.1126/science.aaf6116.

Giannakakou, Paraskevi, Rick Gussio, Eva Nogales, Kenneth H Downing, Daniel Zaharevitz, Birgit Bollbuck, George Poy, Dan Sackett, K C Nicolaou, and Tito Fojo. 2000. "A Common Pharmacophore for Epothilone and Taxanes : Molecular Basis for Drug Resistance Conferred by Tubulin Mutations in Human Cancer Cells." *PNAS*. https://doi.org/10.1073/pnas.040546297.

Gordon, Michael D, and Roel Nusse. 2006. "Wnt Signaling : Multiple Pathways , Multiple Receptors ,." *The Journal of Biological Chemistry* 281 (32): 22429–33. https://doi.org/10.1074/jbc.R600015200.

Guerrini, Renzo, and William B Dobyns. 2017. "Malformations of Cortical Development: Clinical Features and Genetic Causes." *Lancet Neurol.* 13 (7): 710–26. https://doi.org/10.1016/S1474-4422(14)70040-7.

H., Xu, Jiao Y., Qin S., Zhao W., Chu Q., and Wu K. 2018. "Organoid Technology in Disease

Modelling, Drug Development, Personalized Treatment and Regeneration Medicine." *Experimental Hematology and Oncology* 7 (1): 1–12. https://doi.org/10.1186/s40164-018-0122-9 LK.

Jacob, H., Wernig, M., Markoulaki, S., Wang Sun, C., Meissner, A., Cassady, J.P., Beard, C., et al. 2007. "Treatment of Sickle Cell Anemia Mouse Model with IPS Cells Generated from Autologous Skin." *Science* 318 (5858): 1920–23. https://doi.org/10.1126/science.1152092.

Hansen, David V, Jan H Lui, Philip R L Parker, and Arnold R Kriegstein. 2010. "Neurogenic Radial Glia in the Outer Subventricular Zone of Human Neocortex." *Nature* 464 (March): 2–11. https://doi.org/10.1038/nature08845.

Harrison-Uy, Susan J., and Samuel J. Pleasure. 2012. "Wnt Signaling and Forebrain Development." *Cold Spring Harbor Perspectives in Biology* 4 (7): 1–11. https://doi.org/10.1101/cshperspect.a008094.

Hay, Eric, Emmanuel Laplantine, Monique Frain, Thomas Kohler, Ralph Mu, and Pierre J Marie. 2009. "N-Cadherin Interacts with Axin and LRP5 To Negatively Regulate Wnt/ᴺʟ-Catenin Signaling, Osteoblast Function, and Bone Formation." *MOLECULAR AND CELLULAR BIOLOGY* 29 (4): 953–64. https://doi.org/10.1128/MCB.00349-08.

He, Xi, Mikhail Semenov, Keiko Tamai, and Xin Zeng. 2004. "LDL Receptor-Related Proteins 5 and 6 in Wnt / β -Catenin Signaling : Arrows Point the Way." *Development* 1: 1663–77. https://doi.org/10.1242/dev.01117.

Hirotsune, Shinji, Mark W Fleck, Michael J Gambello, Gregory J Bix, Amy Chen, Gary D Clark, David H Ledbetter, Chris J Mcbain, and Anthony Wynshaw-boris. 1998. "Graded Reduction of Pafah1b1 (Lis1) Activity Results in Neuronal Migration Defects and Early Embryonic Lethality." *Nature America* 19 (august): 333–39. https://doi.org/10.1038/1221.

Howard, Sara, Tom Deroo, Yasuyuki Fujita, and Nobue Itasaki. 2011. "A Positive Role of Cadherin in Wnt/β-Catenin Signalling during Epithelial-Mesenchymal Transition." *PLoS ONE* 6 (8). https://doi.org/10.1371/journal.pone.0023899.

Huang, Julie, Anthony J. Roberts, Andres E. Leschziner, and Samara L. Reck-Peterson. 2012. "Lis1 Acts as a 'Clutch' between the ATPase and Microtubule-Binding Domains of the Dynein Motor." *Cell* 150 (5): 975–86. https://doi.org/10.1016/j.cell.2012.07.022.

Iefremova, V., G. Manikakis, O. Krefft, A. Jabali, K. Weynans, R. Wilkens, F. Marsoner, et al. 2017. "An Organoid-Based Model of Cortical Development Identifies Non-Cell-Autonomous Defects in Wnt Signaling Contributing to Miller-Dieker Syndrome." *Cell Reports* 19 (1): 50–59. https://doi.org/10.1016/j.celrep.2017.03.047.

Janssens, Sylvie, Michael Schotsaert, Rahul Karnik, Vinod Balasubramaniam, Marion Dejosez, and Alexander Meissner. 2018. “Zika Virus Alters DNA Methylation of Neural Genes in an Organoid Model of the Developing Human Brain.” *American Society for Microbiology* 3 (1): 1–12. https://doi.org/10.1128/mSystems.00219-17.

Johnson, Matthew B, Peter P Wang, Kutay D Atabay, Elisabeth A Murphy, N Ryan, Jonathan Hecht, and Christopher A Walsh. 2017. “Single Cell Analysis Reveals Transcriptional Heterogeneity of Neural Progenitors in the Human Cortex.” *Nature Neuroscience* 18 (5): 637–46. https://doi.org/10.1038/nn.3980.Single.

Juan Romero, Camino De, and Víctor Borrell. 2015. “Coevolution of Radial Glial Cells and the Cerebral Cortex.” *Glia* 63 (8): 1303–19. https://doi.org/10.1002/glia.22827.

Kadoshima, T., H. Sakaguchi, T. Nakano, M. Soen, S. Ando, M. Eiraku, and Y. Sasai. 2013. “Self-Organization of Axial Polarity, inside-out Layer Pattern, and Species-Specific Progenitor Dynamics in Human ES Cell-Derived Neocortex.” *Proceedings of the National Academy of Sciences* 110 (50): 20284–89. https://doi.org/10.1073/pnas.1315710110.

Kanton, Sabina, Michael James Boyle, Zhisong He, Malgorzata Santel, Anne Weigert, Fátima Sanchís-calleja, Patricia Guijarro, et al. 2019. “Organoid Single-Cell Genomic Atlas Uncovers Human-Specific Features of Brain Development.” *Nature* 574. https://doi.org/10.1038/s41586-019-1654-9.

Karzbrun, Eyal, Aditya Kshirsagar, Sidney R. Cohen, Jacob H. Hanna, and Orly Reiner. 2018. “Human Brain Organoids on a Chip Reveal the Physics of Folding.” *Nature Physics* 14 (5): 515–22. https://doi.org/10.1038/s41567-018-0046-7.

Kato M., Dobyns B. 2003. “Lissencephaly and the Molecular Basis of Neuronal Migration.” *Human Molecular Genetics* 12 (90001): 89R – 96. https://doi.org/10.1093/hmg/ddg086.

Kishida, Shosei, Hideki Yamamoto, Shin-ichiro Hino, Satoshi Ikeda, Michiko Kishida, and Akira Kikuchi. 1999. “DIX Domains of Dvl and Axin Are Necessary for Protein Interactions and Their Ability To Regulate ␣ -Catenin Stability.” *MOLECULAR AND CELLULAR BIOLOGY* 19 (6): 4414–22. https://doi.org/10.1128/mcb.19.6.4414.

Kitagawa, Mayumi, Makiko Umezu, Junken Aoki, Hiroyuki Koizumi, Hiroyuki Arai, and Keizo Inoue. 2000. “Direct Association of LIS1, the Lissencephaly Gene Product, with a Mammalian Homologue of a Fungal Nuclear Distribution Protein, RNUDE.” *FEBS Letters* 479 (1–2): 57–62. https://doi.org/10.1016/S0014-5793(00)01856-1.

Koizumi, Hiroyuki, Noritaka Yamaguchi, Mitsuharu Hattori, Tomo O. Ishikawa, Junken Aoki, Makoto M. Taketo, Keizo Inoue, and Hiroyuki Arai. 2003. “Targeted Disruption of Intracellular Type I Platelet Activating Factor-Acetylhydrolase Catalytic Subunits Causes

Severe Impairment in Spermatogenesis." *Journal of Biological Chemistry* 278 (14): 12489–94. https://doi.org/10.1074/jbc.M211836200.

Komiya, Yuko, and Raymond Habas. 2008. "Wnt Signal Transduction Pathways." *Organogenesis* 4 (2): 68–75. https://doi.org/10.4161/org.4.2.5851.

Krefft, Olivia, Ammar Jabali, Vira Iefremova, Philipp Koch, and Julia Ladewig. 2018. "Generation of Standardized and Reproducible Forebrain-Type Cerebral Organoids from Human Induced Pluripotent Stem Cells." *Journal of Visualized Experiments*, no. 131: 1–8. https://doi.org/10.3791/56768.

Krefft, Olivia, Julia Ladewig, and Philipp Koch. 2020. "Cerebral Organoids to Unravel the Mechanisms Underlying Malformations of Human Cortical Development." *Seminars in Cell and Developmental Biology*. (in press)

Kriks, S., J. Shim, J. Piao, YM. Ganat, DR. Wakeman, Z. Xie, L. Carrillo-Reid, et al. 2012. "Floor Plate-Derived Dopamine Neurons from HESCs Efficiently Engraft in Animal Models of PD." *Nature* 480 (7378): 547–51. https://doi.org/10.1038/nature10648.Floor.

Lancaster, Madeline A., Nina S. Corsini, Simone Wolfinger, E. Hilary Gustafson, Alex W. Phillips, Thomas R. Burkard, Tomoki Otani, Frederick J. Livesey, and Juergen A. Knoblich. 2017. "Guided Self-Organization and Cortical Plate Formation in Human Brain Organoids." *Nature Biotechnology* 35 (7): 659–66. https://doi.org/10.1038/nbt.3906.

Lancaster, Madeline a, Magdalena Renner, Carol-anne Martin, Daniel Wenzel, S Bicknell, Matthew E Hurles, Tessa Homfray, Josef M Penninger, and P Andrew. 2013. "Europe PMC Funders Group Cerebral Organoids Model Human Brain Development and Microcephaly." *Nature* 501 (7467): 373–79. https://doi.org/10.1038/nature12517.Cerebral.

Lancaster, Madeline, Magdalena Renner, Carol-anne Martin, Daniel Wenzel, S Bicknell, Matthew E Hurles, Tessa Homfray, Josef M Penninger, A. P. Jackson, and J. A. Knoblich. 2013. "Cerebral Organoids Model Human Brain Development and Microcephaly." *Nature* 501 (7467): 373–79. https://doi.org/10.1038/nature12517.

Lewitus, Eric, Iva Kelava, and Wieland B. Huttner. 2013. "Conical Expansion of the Outer Subventricular Zone and the Role of Neocortical Folding in Evolution and Development." *Frontiers in Human Neuroscience* 7 (August): 1–12. https://doi.org/10.3389/fnhum.2013.00424.

Li, Chunyan, Siyang Zhang, Yao Lu, Ying Zhang, Enhua Wang, and Zeshi Cui. 2013. "The Roles of Notch3 on the Cell Proliferation and Apoptosis Induced by CHIR99021 in NSCLC Cell Lines: A Functional Link between Wnt and Notch Signaling Pathways."

PLoS ONE 8 (12): 1–9. https://doi.org/10.1371/journal.pone.0084659.

Li, Y., J. Muffat, A. Omer, I Bosch, Lancaster M.A., M. Sur, L. Gehrke, J.A. Knoblich, and R. Jaenisch. 2019. "Induction of Expansion and Folding in Human Cerebral Organoids." *Cell Stem Cell* 20 (3): 385–96. https://doi.org/10.1016/j.stem.2016.11.017.

Marie, Pierre J, and Eric Hay. 2013. "Cadherins and Wnt Signalling : A Functional Link Controlling Bone Formation." *BoneKEy Reports* 330 (April): 1–5. https://doi.org/10.1038/bonekey.2013.64.

Marsoner, Fabio, Philipp Koch, and Julia Ladewig. 2018. "Cortical Organoids: Why All This Hype?" *Current Opinion in Genetics and Development* 52: 22–28. https://doi.org/10.1016/j.gde.2018.04.008.

Marthiens, Véronique, Ilias Kazanis, Lara Moss, Katherine Long, and Charles Ffrench-Constant. 2010. "Adhesion Molecules in the Stem Cell Niche – More than Just Staying in Shape?" *Journal of Cell Science*. https://doi.org/10.1242/jcs.054312.

Mesngon, Mariano T., Cataldo Tarricone, Sachin Hebbar, Aimee M. Guillotte, E. William Schmitt, Lorene Lanier, Andrea Musacchio, Stephen J. King, and Deanna S. Smith. 2006. "Regulation of Cytoplasmic Dynein ATPase by Lis1." *Journal of Neuroscience* 26 (7): 2132–39. https://doi.org/10.1523/JNEUROSCI.5095-05.2006.

Mi Moon, H., and A. Wynshaw-boris. 2013. "Cytoskeleton in Action: Lissencephaly, a Neuronal Migration Disorder." *Wiley Interdiscip Rev Dev Biol.*, no. Type 1: 1–23. https://doi.org/10.1002/wdev.67.Cytoskeleton.

Moon, Hyang Mi, Yong Ha Youn, Hayley Pemble, Jessica Yingling, Torsten Wittmann, and Anthony Wynshaw-Boris. 2014. "LIS1 Controls Mitosis and Mitotic Spindle Organization via the LIS1-NDEL1-Dynein Complex." *Human Molecular Genetics* 23 (2): 449–66. https://doi.org/10.1093/hmg/ddt436.

Morris, S. M., U. Albrecht, O. Reiner, G. Eichele, and L. Y. Yu-Lee. 1998. "The Lissencephaly Gene Product Lis1, a Protein Involved in Neuronal Migration, Interacts with a Nuclear Movement Protein, NudC." *Current Biology* 8 (10): 603–6. https://doi.org/10.1016/S0960-9822(98)70232-5.

Niethammer, Martin, Deanna S. Smith, Ramses Ayala, Junmin Peng, Jane Ko, Ming Sum Lee, Maria Morabito, and Li Huei Tsai. 2000. "NUDEL Is a Novel Cdk5 Substrate That Associates with LIS1 and Cytoplasmic Dynein." *Neuron* 28 (3): 697–711. https://doi.org/10.1016/S0896-6273(00)00147-1.

Okamoto, Satoshi, and Masayo Takahashi. 2011. "Induction of Retinal Pigment Epithelial Cells from Monkey IPS Cells." *Retinal Cell Biology*, 8785–90. https://doi.org/10.1167/iovs.11-

8129.

Ormel, Paul R, Renata Vieira De Sá, Emma J Van Bodegraven, Henk Karst, Oliver Harschnitz, Marjolein A M Sneeboer, Lill Eva Johansen, et al. 2018. “Microglia Innately Develop within Cerebral Organoids.” *Nature Communications*. https://doi.org/10.1038/s41467-018-06684-2.

Pachenari, Narges, Sahar Kiani, and Mohammad Javan. 2017. “Inhibition of Glycogen Synthase Kinase 3 Increased Subventricular Zone Stem Cells Proliferation.” *Biomedicine and Pharmacotherapy* 93: 1074–82. https://doi.org/10.1016/j.biopha.2017.07.043.

Paşca, Anca M, Steven A Sloan, Laura E Clarke, Yuan Tian, Christopher D Makinson, Nina Huber, Kim C H, et al. 2015. “Functional Cortical Neurons and Astrocytes from Human Pluripotent Stem Cells in 3D Culture.” *Nat Methods*. 12 (7): 671–78. https://doi.org/10.1038/nmeth.3415.Functional.

Pawlisz, Ashley S., Christopher Mutch, Anthony Wynshaw-Boris, Anjen Chenn, Christopher A. Walsh, and Yuanyi Feng. 2008. “Lis1-Nde1-Dependent Neuronal Fate Control Determines Cerebral Cortical Size and Lamination.” *Human Molecular Genetics* 17 (16): 2441–55. https://doi.org/10.1093/hmg/ddn144.

Penazzi, Lorène, Christian Tackenberg, Adnan Ghori, Nataliya Golovyashkina, and Roland Brandt. 2016. “Aβ-Mediated Spine Changes in the Hippocampus Are Microtubule-Dependent and Can Be Reversed by a Subnanomolar Concentration of the Microtubule-Stabilizing Agent Epothilone D.” *Neuropharmacology*, no. 541: 84–95. https://doi.org/10.1016/j.neuropharm.2016.01.002.A.

Philbert, Marion, Camille Maillard, Mara Cavallin, Alice Goldenberg, Cecile Masson, Nathalie Boddaert, Adrienne El Morjani, et al. 2017. “A Novel Recurrent LIS1 Splice Site Mutation in Classic Lissencephaly.” *American Journal of Medical Genetics, Part A* 173 (2): 561–64. https://doi.org/10.1002/ajmg.a.38041.

Pilz, Daniela T., Michelle E. Macha, Kathrin S. Precht, Ann C.M. Smith, William B. Dobyns, and David H. Ledbetter. 1998. “Fluorescence in Situ Hybridization Analysis with LIS1 Specific Probes Reveals a High Deletion Mutation Rate in Isolated Lissencephaly Sequence.” *Genetics in Medicine* 1 (1): 29–33. https://doi.org/10.1097/00125817-199811000-00007.

Qian, X., H. N. Nguyen, M. M. Song, C. Hadiono, Sarah C. Ogden, Christy Hammack, Bing Yao, et al. 2016. “Brain Region-Specific Organoids Using Mini-Bioreactors for Modeling ZIKV Exposure.” *Cell* 131 (3): 393–409. https://doi.org/10.1007/s00401-015-1526-9.

Qian, Xuyu, Ha Nam Nguyen, Mingxi M. Song, Christopher Hadiono, Sarah C. Ogden, Christy

Hammack, Bing Yao, et al. 2016. “Brain-Region-Specific Organoids Using Mini-Bioreactors for Modeling ZIKV Exposure.” *Cell* 165 (5): 1238–54. https://doi.org/10.1016/j.cell.2016.04.032.

Quadrato, Giorgia, Tuan Nguyen, Evan Z Macosko, John L Sherwood, Sung Min Yang, Daniel R Berger, Edward S Boyden, et al. 2017. “Cell Diversity and Network Dynamics in Photosensitive Human Brain Organoids.” *Nature* 545 (7652): 48–53. https://doi.org/10.1038/nature22047.

Reiner, Orly, Romeo Carrozzo, Ying Shen, Manfred Wehnert, Fabrizia Faustinella, William B. Dobyns, C. Thomas Caskey, and David H. Ledbetter. 1993. “Isolation of a Miller-Dicker Lissencephaly Gene Containing G Protein β-Subunit-like Repeats.” *Nature* 364 (6439): 717–21. https://doi.org/10.1038/364717a0.

Renner, Magdalena, Madeline A Lancaster, Shan Bian, Heejin Choi, Taeyun Ku, Angela Peer, C. Kwanghun, and Juergen A Knoblich. 2017. “Self-Organized Developmental Patterning and Differentiation in Cerebral Organoids.” *The EMBO Journal* 36 (10): 1316–29. https://doi.org/10.15252/embj.201694700.

Saillour, Yoann, Nathalie Carion, Chloé Quelin, Pierre Louis Leger, Nathalie Boddaert, Caroline Elie, Annick Toutain, et al. 2009. “LIS1-Related Isolated Lissencephaly: Spectrum of Mutations and Relationships with Malformation Severity.” *Archives of Neurology* 66 (8): 1007–15. https://doi.org/10.1001/archneurol.2009.149.

Sasaki, Shinji, Aki Shionoya, Michiyo Ishida, Michael J. Gambello, Jessica Yingling, Anthony Wynshaw-Boris, and Shinji Hirotsune. 2000. “A LIS1/NUDEL/Cytoplasmic Dynein Heavy Chain Complex in the Developing and Adult Nervous System.” *Neuron* 28 (3): 681–96. https://doi.org/10.1016/S0896-6273(00)00146-X.

Shu, Tianzhi, Ramses Ayala, Minh-dang Nguyen, Zhigang Xie, Joseph G Gleeson, and Li-huei Tsai. 2004. “Ndel1 Operates in a Common Pathway with LIS1 and Cytoplasmic Dynein to Regulate Cortical Neuronal Positioning.” *Neuron* 44: 263–77. https://doi.org/10.1016/j.neuron.2004.09.030.

Smith, Deanna S, Martin Niethammer, Ramses Ayala, Ying Zhou, Michael J Gambello, and Li-huei Tsai. 2000. “Regulation of Cytoplasmic Dynein Behaviour and Microtubule Organization by Mammalian Lis1.” *Nature Cell Biology* 2 (NOVEMBER): 767–75. https://doi.org/10.1038/35041000.

Song, L., X. Yuan, Z. Jones, C. Vied, Y. Miao, M. Marzano, T. Hua, et al. 2019. “Functionalization of Brain Region- Specific Spheroids with Isogenic Microglia-like Cells.” *Nature Scientific Reports*, no. July: 1–18. https://doi.org/10.1038/s41598-019-

47444-6.

Stocker, Adam M, and Anjen Chenn. 2009. “Focal Reduction of α E-Catenin Causes Premature Differentiation and Reduction of β -Catenin Signaling during Cortical Development.” *Developmental Biology* 328: 66–77. https://doi.org/10.1016/j.ydbio.2009.01.010.

Susaki, Etsuo A., Kazuki Tainaka, Dimitri Perrin, Fumiaki Kishino, Takehiro Tawara, Tomonobu M. Watanabe, Chihiro Yokoyama, et al. 2014. “Whole-Brain Imaging with Single-Cell Resolution Using Chemical Cocktails and Computational Analysis.” *Cell* 157 (3): 726–39. https://doi.org/10.1016/j.cell.2014.03.042.

Taapken, Seth M, Benjamin S Nisler, Michael A Newton, Tori L Sampsell-Barron, Kimberly A Leonhard, Erik M McIntire, and Karen D Montgomery. 2011. “Karyotypic Abnormalities in Human Induced Pluripotent Stem Cells and Embryonic Stem Cells.” *Nat. Biotechnol.* 29 (4): 2009–11. https://doi.org/10.1038/nbt.1835.

Tai, Chin Yin, Denis L. Dujardin, Nicole E. Faulkner, and Richard B. Vallee. 2002. “Role of Dynein, Dynactin, and CLIP-170 Interactions in LIS1 Kinetochore Function.” *Journal of Cell Biology* 156 (6): 959–68. https://doi.org/10.1083/jcb.200109046.

Takahashi K, Okita K, Nakagawa M, Yamanaka S. 2007. “Induction of Pluripotent Stem Cells from Fibroblast Cultures.” *Nature Protocols* 2 (12): 3081–89. https://doi.org/10.1038/nprot.2007.418.

Takahashi, Kazutoshi, Koji Tanabe, Mari Ohnuki, Megumi Narita, Tomoko Ichisaka, Kiichiro Tomoda, and Shinya Yamanaka. 2007. “Induction of Pluripotent Stem Cells from Adult Human Fibroblasts by Defined Factors.” *Cell*, 861–72. https://doi.org/10.1016/j.cell.2007.11.019.

Tanaka, Teruyuki, Finley F. Serneo, Christine Higgins, Michael J. Gambello, Anthony Wynshaw-Boris, and Joseph G. Gleeson. 2004. “Lis1 and Doublecortin Function with Dynein to Mediate Coupling of the Nucleus to the Centrosome in Neuronal Migration.” *Journal of Cell Biology* 165 (5): 709–21. https://doi.org/10.1083/jcb.200309025.

Toropova, Katerina, Sirui Zou, Anthony J. Roberts, William B. Redwine, Brian S. Goodman, Samara L. Reck-Peterson, and Andres E. Leschziner. 2014. “Lis1 Regulates Dynein by Sterically Blocking Its Mechanochemical Cycle.” *ELife* 3: 1–25. https://doi.org/10.7554/eLife.03372.

Tran, Nhan L, Deanna G Adams, Richard R Vaillancourt, and Ronald L Heimark. 2002. “Signal Transduction from N-Cadherin Increases Bcl-2.” *The Journal of Biological Chemistry* 277 (36): 32905–14. https://doi.org/10.1074/jbc.M200300200.

Tsai J, Chen Y, Kriegstein A, Vallee R. 2005. “LIS1 RNA Interference Blocks Neural Stem

Cell Division, Morphogenesis, and Motility at Multiple Stages." *Jouranl of Cell Biology*, 935–45. https://doi.org/10.1083/jcb.200505166.

Tsujia, Osahiko, Kyoko Miuraa, Yohei Okadaa, Kanehiro Fujiyoshia, Masahiko Mukaino, Narihito Nagoshia, Kazuya Kitamuraa, et al. 2010. "Therapeutic Potential of Appropriately Evaluated Safe-Induced Pluripotent Stem Cells for Spinal Cord Injury." *PNAS* 107 (28). https://doi.org/10.1073/pnas.0910106107.

Uyanik, G., D. J. Morris-Rosendahl, J. Stiegler, J. Klapecki, C. Gross, Y. Berman, P. Martin, et al. 2007. "Location and Type of Mutation in the LIS1 Gene Do Not Predict Phenotypic Severity." *Neurology* 69 (5): 442–47. https://doi.org/10.1212/01.wnl.0000266629.98503.d0.

Uzquiano, Ana, Carmen Cifuentes-Diaz, A. Jabali, Delfina M. Romero, Anne Houllier, Florent Dingli, Camille Maillard, et al. 2019. "Mutations in the Heterotopia Gene Eml1/EML1 Severely Disrupt the Formation of Primary Cilia." *Cell Reports* 28 (6): 1596-1611.e10. https://doi.org/10.1016/j.celrep.2019.06.096.

Velasco, S., A.J. Kedaigle, S.K. Simmons, A. Nash, M. Rocha, G. Quadrato, B. Paulsen, et al. 2019. "Individual Brain Organoids Reproducibly Form Cell Diversity of the Human Cerebral Cortex." *Nature*. https://doi.org/10.1038/s41586-019-1289-x.

Watanabe, M., J. E. Buth, N. Vishlaghi, L. de la Torre-Ubieta, J. Taxidis, B. Khakh, G. Coppola, et al. 2016. "Self-Organized Cerebral Organoids with Human-Specific Features Predict Effective Drugs to Combat Zika Virus Infection." *Cell Reports* 21 (2): 517–32. https://doi.org/10.1016/j.celrep.2017.09.047.

Weissman, Irving L. 2000. "Stem Cells: Units of Development, Units of Regeneration, and Units in Evolution." *Cell* 100 (1): 157–68. https://doi.org/10.1016/S0092-8674(00)81692-X.

Wells, Michael F., Max R. Salick, Ole Wiskow, Daniel J. Ho, Kathleen A. Worringer, Robert J. Ihry, Sravya Kommineni, et al. 2016. "Genetic Ablation of AXL Does Not Protect Human Neural Progenitor Cells and Cerebral Organoids from Zika Virus Infection." *Cell Stem Cell* 19 (6): 703–8. https://doi.org/10.1016/j.stem.2016.11.011.

Wimmer, Reiner A, Alexandra Leopoldi, Martin Aichinger, Dontscho Kerjaschki, and Josef M Penninger. 2019. "Generation of Blood Vessel Organoids from Human Pluripotent Stem Cells." *Nature Protocols*. https://doi.org/10.1038/s41596-019-0213-z.

Woodhead G., Mutch C. A., Olson E. C, Chenn A. 2006. "Cell-Autonomous β-Catenin Signaling Regulates Cortical Precursor Proliferation." *J Neurosci.* 23 (1): 1–7. https://doi.org/10.1038/jid.2014.371.

Xiang, Yangfei, Yoshiaki Tanaka, Benjamin Patterson, Young Jin Kang, Gubbi Govindaiah, Naomi Roselaar, Bilal Cakir, et al. 2017. “Fusion of Regionally Specified HPSC-Derived Organoids Models Human Brain Development and Interneuron Migration.” *Cell Stem Cell* 21 (3): 383-398.e7. https://doi.org/10.1016/j.stem.2017.07.007.

Yamada, M., Yuko Yoshida, Daisuke Mori, Takako Takitoh, Mineko Kengaku, Hiroki Umeshima, Keizo Takao, et al. 2009. “Inhibition of Calpain Increases LIS1 Expression and Partially Rescues in Vivo Phenotypes in a Mouse Model of Lissencephaly.” *Nature Medicine* 15 (10). https://doi.org/10.1038/nm.2023.

Yamada, Masami, Yuko Yoshida, Daisuke Mori, Takako Takitoh, Mineko Kengaku, Hiroki Umeshima, Keizo Takao, et al. 2013. “Rab6a Releases LIS1 from a Dynein Idling Complex and Activates Dynein for Retrograde Movement.” *Nature Communications* 4 (May): 1–10. https://doi.org/10.1038/ncomms3033.

Yan, Wei, Amir H. Assadi, Anthony Wynshaw-Boris, Gregor Eichele, Martin M. Matzuk, and Gary D. Clark. 2003. “Previously Uncharacterized Roles of Platelet-Activating Factor Acetylhydrolase 1b Complex in Mouse Spermatogenesis.” *Proceedings of the National Academy of Sciences of the United States of America* 100 (12): 7189–94. https://doi.org/10.1073/pnas.1236145100.

Yingling, J., Y.H. Youn, D. Darling, K. Toyo-oka, T. Pramparo, S. Hirotsune, and A. Wynshaw-Boris. 2008. “Neuroepithelial Stem Cell Proliferation Requires LIS1 for Precise Spindle Orientation and Symmetric Division.” *Cell* 132 (3): 474–86. https://doi.org/10.1016/j.cell.2008.01 .026.

Youn, Ji-Young, Boris J A Dyakov, Jianping Zhang, James D R Knight, Robert M Vernon, Julie D Forman-Kay, and Anne-Claude Gingras. 2019. “Properties of Stress Granule and P-Body Proteomes.” *Molecular Cell*. https://doi.org/10.1016/j.molcel.2019.09.014.

Youn, Yong Ha, Tiziano Pramparo, Shinji Hirotsune, and Anthony Wynshaw-Boris. 2009. “Distinct Dose-Dependent Cortical Neuronal Migration and Neurite Extension Defects in Lis1 and Ndel1 Mutant Mice.” *Journal of Neuroscience* 29 (49): 15520–30. https://doi.org/10.1523/JNEUROSCI.4630-09.2009.

Yu, Junying, Maxim A Vodyanik, Kim Smuga-otto, Jessica Antosiewicz-bourget, Jennifer L Frane, Shulan Tian, Jeff Nie, et al. 2007. “Induced Pluripotent Stem Cell Lines Derived from Human Somatic Cells.” *Science* 318 (December). https://doi.org/10.1126/science.1151526.

Zechner, Dietmar, Yasuyuki Fujita, Thomas Mu, Ingrid Walther, Makoto M Taketo, E Bryan Crenshaw, Walter Birchmeier, and Carmen Birchmeier. 2003. “Beta-Catenin Signals

Regulate Cell Growth and the Balance between Progenitor Cell Expansion and Differentiation in the Nervous System." *Dev Biol* 258: 406–18. https://doi.org/10.1016/S0012-1606(03)00123-4.

Zhang, Bin, Jenna Carroll, John Q Trojanowski, Yuemang Yao, Michiyo Iba, Justin S Potuzak, Anne-marie L Hogan, et al. 2012. "The Microtubule-Stabilizing Agent , Epothilone D , Reduces Axonal Dysfunction , Neurotoxicity , Cognitive Deficits , and Alzheimer-Like Pathology in an Interventional Study with Aged Tau Transgenic Mice." *The Journal of Neuroscience* 32 (11): 3601–11. https://doi.org/10.1523/JNEUROSCI.4922-11.2012.

Zhang, Jianing, Julie R. Shemezis, Erin R. McQuinn, Jing Wang, Maria Sverdlov, and Anjen Chenn. 2013. "AKT Activation by N-Cadherin Regulates Beta-Catenin Signaling and Neuronal Differentiation during Cortical Development." *Neural Development* 8 (1): 1. https://doi.org/10.1186/1749-8104-8-7.

Zhang, Jianing, Gregory J Woodhead, Sruthi K Swaminathan, Stephanie R Noles, Erin R Mcquinn, Anna J Pisarek, Adam M Stocker, Christopher A Mutch, Nobuo Funatsu, and Anjen Chenn. 2010. "Cortical Neural Precursors Inhibit Their Own Differentiation via N-Cadherin Maintenance of b -Catenin Signaling." *Developmental Cell*, 472–79. https://doi.org/10.1016/j.devcel.2009.12.025.

Zhang, Su-chun, Marius Wernig, Ian D Duncan, and James A Thomson. 2001. "In Vitro Differentiation of Transplantable Neural Precursors from Human Embryonic Stem Cells." *Nature Biotechnology* 19 (December): 1129–33. https://doi.org/10.1038/nbt1201-1129.

Appendix 1, Overview of iPS cell lines included in this study and validation steps

Table 18: Overview and validation steps of iPS cell lines included in this study.

	Pluripotency maker expression	Karyotyping	Tripotente differentiation	Validation of LIS1 mutation
Control 1.1	yes	yes	yes	no
Control 1.2	yes	yes	yes	no
Control 2.1	yes	yes	yes	no
Control 2.2	yes	yes	yes	no
Control 3.1	yes	yes	yes	no
Control 4.1	yes	yes	yes	no
Control 4.2	yes	yes	yes	no
Control 5.1	yes	yes	yes	no
Control 6.1	yes	yes	yes	no
mild 1.1	yes	yes	yes	yes
mild 1.2	yes	yes	yes	yes
mild 2.1	yes	yes	yes	yes
mild 2.2	yes	yes	yes	yes
moderate 1.1	yes	yes	yes	yes
moderate 1.2	yes	yes	yes	yes
moderate 2.1	yes	yes	yes	yes
moderate 2.2	yes	yes	yes	yes
severe 1.1	yes	yes	yes	yes
severe 1.2	yes	yes	yes	yes
severe 2.1	yes	yes	yes	yes
severe 2.2	yes	yes	yes	yes
severe 3.1	yes	yes	yes	yes
severe 3.2	yes	yes	yes	yes

Appendix 2, Statistics

Table 19: Post-Hoc group comparison of Kruskal-Wallis-Test of VZ diameter analyzes for control- and LIS1-patient derived organoids at day 20.

Sample 1-Sample 2	sig.	adj. sig.[a]
control mild	,000	,000
control moderate	,000	,000
control severe	,000	,000

a. Significance values have been adjusted by the Bonferroni correction for multiple tests

Table 20: Post-Hoc group comparison of Kruskal-Wallis-Test of apical membrane length for analyzes for control- and LIS1-patient derived organoids at day 20.

Sample 1-Sample 2	sig.	adj. sig.[a]
control mild	,066	,393
control moderate	,000	,002
control severe	,000	,000

a. Significance values have been adjusted by the Bonferroni correction for multiple tests

Table 21: Post-Hoc group comparison of Kruskal-Wallis-Test of total VZ area analyzes for control- and LIS1-patient derived organoids at day 20.

Sample 1-Sample 2	sig.	adj. sig.[a]
control mild	,441	1,000
control moderate	,000	,001
control severe	,000	,000

a. Significance values have been adjusted by the Bonferroni correction for multiple tests

Table 22: Post-Hoc group comparison of Kruskal-Wallis-Test of ventricle-like area analyzes for control- and LIS1-patient derived organoids at day 20.

Sample 1-Sample 2	sig.	adj. sig.[a]
control mild	,066	,393
control moderate	,000	,002
control severe	,000	,000

a. Significance values have been adjusted by the Bonferroni correction for multiple tests

Table 23: Post-Hoc group comparison of Kruskal-Wallis-Test of basal membrane length analyzes for control- and LIS1-patient derived organoids at day 20.

Sample 1-Sample 2	sig.	adj. sig.[a]
control mild	,003	,019
control moderate	,000	,000
control severe	,000	,000

a. Significance values have been adjusted by the Bonferroni correction for multiple tests

Table 24: Post-Hoc group comparison of Kruskal-Wallis-Test of VZ tissue area analyzes for control- and LIS1-patient derived organoids at day 20.

Sample 1-Sample 2	sig.	adj. sig.[a]
control mild	,671	1,000
control moderate	,000	,001
control severe	,000	,000

a. Significance values have been adjusted by the Bonferroni correction for multiple tests

Table 25: Post-Hoc group comparison of Kruskal-Wallis-Test for AC-TUB strand density in basal regions quantification in control- and LIS1-patient derived organoids at day 20.

Sample 1-Sample 2	sig.	adj. sig.[a]
control C 1.2-mild P1.1	,413	1,000
control C 1.2-mild P1.2	,055	1,000
control C 1.2-mild P2.1	,057	1,000
control C 1.2-mild P2.2	,251	1,000
control C 1.2-moderate P3.1	,057	1,000
control C 1.2-moderate P3.2	,000	,000
control C 1.2-moderate P4.1	,000	,002
control C 1.2-moderate P4.2	,003	,335
control C 1.2-severe P5.1	,000	,001
control C 1.2-severe P5.2	,000	,000
control C 1.2-severe P6.2	,000	,000
control C 1.2-severe P6.2	,000	,000
control C 1.2-severe P7.1	,000	,000
control C 1.2-severe P7.2	,000	,000
control C 4.2-control C 1.2	,407	1,000
control C 4.2-mild P1.1	,870	1,000
control C 4.2-mild P1.2	,340	1,000
control C 4.2-mild P2.1	,348	1,000
control C 4.2-mild P2.2	,822	1,000
control C 4.2-moderate P3.1	,362	1,000
control C 4.2-moderate P3.2	,000	,030
control C 4.2-moderate P4.1	,001	,144
control C 4.2-moderate P4.2	,047	1,000
control C 4.2-severe P5.1	,001	,086
control C 4.2-severe P5.2	,000	,000
control C 4.2-severe P6.1	,000	,002
control C 4.2-severe P6.2	,000	,011
control C 4.2-severe P7.1	,000	,009
control C 4.2-severe P7.2	,000	,010

Table 26: Post-Hoc group comparison of Kruskal-Wallis-Test for N-CAD disruption diameter quantification for control- and LIS1-patient derived organoids at day 20.

Sample 1-Sample 2	sig.	adj. sig.[a]
control C 2.1-mild P1.1	,522	1,000
control C 2.1-mild P2.1	,087	1,000
control C 2.1-mild P2.2	,022	1,000
control C 2.1-mild P1.2	,002	,296
control C 2.1-moderate P3.1	,035	1,000
control C 2.1-moderate P4.1	,000	,005

control C 2.1-moderate P4.2	,000	,011
control C 2.1-severe P5.1	,000	,004
control C 2.1-severe P5.2	,000	,000
control C 2.1-severe P6.1	,000	,000
control C 2.1-severe P6.2	,000	,000
control C 2.1-severe P7.1	,000	,000
control C 4.2-mild P1.1	,691	1,000
control C 4.2-mild P1.2	,011	1,000
control C 4.2-mild P2.1	,170	1,000
control C 4.2-mild P2.2	,057	1,000
control C 4.2-moderate P3.1	,084	1,000
control C 4.2-moderate P3.2	,000	,029
control C 4.2-moderate P4.1	,000	,053
control C 4.2-moderate P4.2	,001	,106
control C 4.2-severe P5.1	,000	,056
control C 4.2-severe P5.2	,000	,000
control C 4.2-severe P6.1	,000	,000
control C 4.2-severe P6.2	,000	,001
control C 4.2-severe P7.1	,000	,000

a. Significance values have been adjusted by the Bonferroni correction for multiple tests.

Table 27: Kruskal-Wallis-Test for independent samples without Gaussian distribution for AC-TUB strand density quantification in basal VZ regions for EpothiloneD vs. DMSO control treated control- and LIS1-patient derived organoids at day 15.

	control C 4.1	control C 3.1	mild P1.1	mild 2.2	moderate P3.2	severe P5.1	severe P6.1	severe P7.1
asymptotic sig. (2-sided test)	,892	0,743	0,003	0,003	,771	0,008	0,004	,012

a. the test statistic is adjusted for ties.

Table 28: Kruskal-Wallis-Tests for independent samples without Gaussian distribution for N-CAD disruption diameter quantification of EpothiloneD and DMSO control treated control- and LIS1-patient-organoids at day 20.

	control C 4.1	control C 3.1	mild P1.1	mild P2.1	moderate P3.2	severe P5.1	severe P7.1
asymptotic sig. (2-sided test)	0,518	0,287	,037	0,623	0,336	0,109	0,055

a. the test statistic is adjusted for ties.

Table 29: Kruskal-Wallis-Test for independent samples without Gaussian distribution for VZ diameter quantification of CHIR and EpothiloneD treated control- and LIS1-patient derived organoids at day 15.

Asymptotic sig. (2-sided test)	sig. DMSO vs EpoD
control C4.1	,398
control C3.1	,735
mild P1.1	,149
mild P2.2	,061
moderate P3.2	,010

severe P5.1	,005
severe P6.1	,001
severe P7.1	,013

a. The test statistic is adjusted for ties.

Table 30: Kruskal-Wallis-Test for independent samples without Gaussian distribution for WNT-GFP quantification of control- and LIS1-patient derived organoids at day 20.

Asymptotic sig. (2-sided test)	sig. to C3.1
control C4.1	0,182
mild P1.1	0,449
mild P2.2	0,4889
moderate P3.2	0,009
severe P5.1	0,000

a. The test statistic is adjusted for ties.

Table 31: Post-Hoc group comparison of Kruskal-Wallis-Test of horizontal aRG cell division percentage of control- and LIS1-patient derived organoids at day 20.

Sample 1-Sample 2	sig.	adj. sig.[a]
vertical		
control C 4.2-mild P1.1	,136	1,000
control C 4.2-mild P1.2	,788	1,000
control C 4.2-mild P2.1	,283	1,000
control C 4.2-mild P2.2	,587	1,000
control C 4.2-moderate P3.1	,106	1,000
control C 4.2-moderate P3.2	,067	1,000
control C 4.2-moderate P4.1	,039	1,000
control C 4.2-moderate P4.2	,137	1,000
control C 4.2-severe P5.1	,000	,006
control C 4.2-severe P5.2	,039	,054
control C 4.2-severe P6.1	,002	,150
control C 4.2-severe P6.2	,000	,020
control C 4.2-severe P7.1	,000	,007
horizontal		
control C 4.2-mild P1.1	,030	1,000
control C 4.2-mild P1.2	,573	1,000
control C 4.2-mild P2.1	,196	1,000
control C 4.2-mild P2.2	,141	1,000
control C 4.2-moderate P3.1	,001	,067
control C 4.2-moderate P3.2	,002	,197
control C 4.2-moderate P4.1	,001	,088
control C 4.2-moderate P4.2	,001	,023
control C 4.2-severe P5.1	,000	,003
control C 4.2-severe P5.2	,001	,047
control C 4.2-severe P6.1	,000	,020

control C 4.2-severe P6.2	,002	,015
control C 4.2-severe P7.1	,000	,007
oblique		
control C 4.2-mild P1.1	,042	1,000
control C 4.2-mild P1.2	,295	1,000
control C 4.2-mild P2.1	,687	1,000
control C 4.2-mild P2.2	,148	1,000
control C 4.2-moderate P3.1	,037	1,000
control C 4.2-moderate P3.2	,036	1,000
control C 4.2-moderate P4.1	,033	1,000
control C 4.2-moderate P4.2	,043	1,000
control C 4.2-severe P5.1	,259	1,000
control C 4.2-severe P5.2	,013	1,000
control C 4.2-severe P6.1	,072	1,000
control C 4.2-severe P6.2	,358	1,000
control C 4.2-severe P7.1	,031	1,000

a. Significance values have been adjusted by the Bonferroni correction for multiple tests

Table 32: Post-Hoc group comparison of Kruskal-Wallis-Test for plane of cell division quantification in CHIR and DMSO control treated control- and LIS1-patient derived organoids at day 15.

DMSO-EpoD	sig.	adj. sig.[a]
horizontal		
control C 3.1	,687	1,000
mild P1.1	,639	1,000
moderate P3.2	,791	1,000
severe P5.1	,011	,031
vertical		
control C 3.1	,958	1,000
mild P1.1	,892	1,000
moderate P3.2	,098	1,000
severe P5.1	,012	,032

a. Significance values have been adjusted by the Bonferroni correction for multiple tests

Table 33: Post-Hoc group comparison of Kruskal-Wallis-Test for VZ diameter quantification of CHIR and EpothiloneD treated control- and LIS1-patient derived organoids at day 15.

condition	sig. DMSO vs. CHIR
control C4.1	,722
control C3.1	1,000
mild P1.1	,185
mild P2.2	,061
moderate 3.2	,011
severe P5.1	,000
severe P6.1	,001
severe P7.1	,054

Acknowledgements

First, I want to thank my supervisor Dr. Julia Ladewig for her support and for giving me a high degree of freedom, which allowed me to develop my own ideas and improve my research skills. I also want to thank Prof. Dr. Philipp Koch for his advice and input during our group meetings. I am also grateful to the European Rare Disease Network Neuron for financial support and to our international collaboration partners Dr. Fiona Francis, Dr. Nadja Bahi-Buisson, Prof. Dr. Orly Reiner and Dr. Laurent Nguyen for the precious contribution during our annual meetings somewhere at beautiful cities in Europe.

Furthermore, I also wish to thank Dr. Otto Bräunling and the Interdisciplinary Center of Neuroscience for giving me the possibility to be part of an amazing graduate school with many networking opportunities.

Moreover, I would like to thank Helene Schamber and Gina Tillmann for technical assistance.

I also owe a great debt of gratitude to all my friends and colleagues from the Hector Institute of Translational Brain Research for a good working atmosphere and general support.

Finally, and most importantly, I am tremendously grateful to my parents Viola and Volker, my stepfather Rainer, my grandparents Christel and Erhard, my sister Anja and my partner in crime Marvin for unconditional love, constant support, patience and believing in me.

Publications, presentations and awards

Publications:

- Iefremova V., Manikakis G., Jabali A., Weynans K., Krefft O., Brändl B., Müller FJ., Koch P. and Ladewig J., An organoid-based model of cortical development identifies non-cell autonomous defects in ß-CATsignaling contributing to Miller-Dieker-Syndrome. Cell Reports 19(1):50-59 (2017) doi: 10.1016/j.celrep.2017.03.047
- Krefft O., Jabali A., Iefremova V., Koch P. and Ladewig J., Generation of standardized and reproducible forebrain-type cerebral organoids from human induced pluripotent stem cells. J Vis Exp. 2018 Jan 23;(131) doi: 10.3791/56768
- Krefft O., Koch P. and Ladewig J., Cerebral organoids to unravel the mechanisms underlying malformations of human cortical development. Seminars in Cell & Developmental Biology (review, in press).
- Krefft O., Hoffrichter A., Maillard C., Jabali A., Marsoner F., Koch P. and Ladewig J., Unraveling the pathology of different disease severities in human cerebral organoid models of LIS1-lissencephaly. (in final preparation).

Presentations:

- Internal Meeting of the Stem Cell Network Nordrhein-Westfalen, Herne, Germany, 2016
- International Meeting of the Stem cell network Nordrhein-Westfalen, Münster, Germany, 2017
- Rare Disease Network Neuron Mid-term Symposium, RIGA, Latvia, 2017
- Cajal school “Developmental Neurobiology and Pathologies”, Bordeaux, France, 2018
- 6th Annual German Stem Cell Network Meeting, Heidelberg, Germany, 2018
- Central Institute of Mental Health Retreat, Bad Dürkheim, Germany, 2018
- International Society for Stem Cell Research Annual Meeting, Los Angeles, USA, 2019
- Central Institute of Mental Health Retreat, Mannheim, Germany, 2019
- Interdisciplinary Center of Neuroscience Seminar, Heidelberg, Germany 2020

Awards/ research funding:

- Travel Award, International Society for Stem Cell Research, Los Angeles, USA, 2019
- Add-on Funding SFB1324, German Cancer Research Center, Heidelberg, Germany, 2019
- Poster Award, Central Institute of Mental Health Retreat, Mannheim, Germany, 2019